

IBM-LBM Modelling of Two-Phase Flow in Porous Media

Wenxin Zuo

A thesis submitted to the University of Birmingham
for the degree of
DOCTOR OF PHILOSOPHY

School of Civil Engineering

University of Birmingham

Oct. 2015

UNIVERSITY OF
BIRMINGHAM

University of Birmingham Research Archive

e-theses repository

This unpublished thesis/dissertation is copyright of the author and/or third parties. The intellectual property rights of the author or third parties in respect of this work are as defined by The Copyright Designs and Patents Act 1988 or as modified by any successor legislation.

Any use made of information contained in this thesis/dissertation must be in accordance with that legislation and must be properly acknowledged. Further distribution or reproduction in any format is prohibited without the permission of the copyright holder.

Abstract

The phenomena of Two-Phase Flow with large density ratio (about 1000:1) in porous media occurs in many environmental and industrial processes, including the unsaturated water flow, the enhanced oil recovery and the slope stability analysis. Due to the time requirement and the relative high cost with the experimental approaches, numerical techniques become a popular alternative approach to simulate and understand the behaviour of a multi-fluid flow system.

This thesis aims to develop a numerical tool to simulate the Two-Phase Flow along curved solid boundaries for the multiphase Lattice Boltzmann (LB) method. Based on the existing single-fluid numerical tool FPS-BHAM, the multiphase Lattice Boltzmann method is incorporated into the computer code to simulate the interaction between two different fluids with large density ratio. In addition, a modified Ghost Fluid Immersed Boundary (GFIB) model is proposed in this thesis to capture the local interaction behaviour among fluids and solid curved boundaries. Furthermore, a new forcing calculation method is presented to predict the mechanical behaviour of the meniscus along the curved boundaries.

The new code is first checked with the droplet test and the capillary rise test, in which the LB model is verified to be stable for two fluids with large density jump across its interface. Then the capillary bridge test and the contact line dynamic test are used to validate the accuracy of the GFIB model applied to curved boundaries. With the newly proposed forcing calculation method in this thesis, the computed capillary forces in all six cases resulted in only less than 5.0% error in comparison with the analytical solutions. The new LB-GFIB model is further verified with capillary rise in the porous media. Though only 44 solid particles are used in the simulation, the numerical pressure still satisfies the theoretical one with about 12.7% error.

In addition, the parameter studies are conducted to gauge the influence of four main parameters in the model, including the interface thickness, the mobility, the domain size and the grid resolution. Except for the interface thickness, the other three have little impacts on the accuracy of the results; however, the equilibrium time in the computation is influenced by the mobility and the grid resolution. As a result, the new code with the LB-GFIB model can provide an alternative way to study the complex process of Two-Phase Flow in the porous media.

KEY WORDS: Lattice Boltzmann Method, Two –phase Fluid Flow, Curved Boundary, Ghost Fluid Immersed Boundary Method

ACKNOWLEDGEMENTS

Firstly, I would like to express my sincere gratitude to my supervisors: Professor John Bridgeman, Professor Andrew Chan and Dr. Soroosh Sharifi for their patient help and guidance throughout my study. I also would like to thank Dr. Jun Li and Dr. Xilin Cui for their help with the FPS-BHAM code and their encouragement during last four years. Besides, I wish to thank all the colleagues in Room F8 in Civil Engineering for their support.

A great thank goes to the University of Birmingham and School of Civil Engineering for providing a three and half years Elite Scholarship and I would also appreciate the BlueBEAR Committee for their technique support by HPC cluster for the numerical simulations in this thesis.

I wish to thank my parents and my wife, who provide me with strength to take challenge every day. Without their steadfast love and their support, I can hardly pass the difficult time in my study.

Finally, I must give my deepest gratitude to the Heavenly Father, the almighty creator of this world. His grace, love and unchanging promises provide me strength and wisdom to accomplish this thesis in time.

CONTENTS

Abstract.....	I
ACKNOWLEDGEMENTS.....	III
Chapter 1 Introduction.....	1
1.1 Background.....	1
1.2 Numerical techniques for modelling multi-fluid flow in porous media.....	2
1.3 Aim of this research.....	3
1.4 Thesis layout.....	4
Chapter 2 Literature Review.....	5
2.1 Introduction.....	5
2.2 Experiments and estimation for unsaturated soil.....	5
2.3 Computational Fluid Dynamics (CFD) simulation for multiphase flow.....	7
2.4 Lattice Boltzmann (LB) method.....	14
2.5 The solid–fluid boundary condition in LBM.....	18
2.6 Summary.....	25
Chapter 3 Methodology.....	26
3.1 Lattice Boltzmann (LB) method.....	26
3.2 Fluid–solid interaction models.....	32
Chapter 4 Validation and Verification.....	37
4.1 Droplet test at large density ratio.....	37
4.2 Capillary tube.....	41
4.3 Capillary bridge between two circular bodies.....	50
4.4 Contact line dynamics between two alongside cylinders.....	60
4.5 Capillary rise in porous media.....	71
4.6 Summary.....	82
Chapter 5 Parametric Study.....	84
5.1 Interface thickness dependence.....	84
5.2 Mobility dependence.....	88
5.3 Domain size dependence.....	94
5.4 Grid resolution dependence.....	101
5.5 Summary.....	108
Chapter 6 Conclusions and Future Work.....	110
6.1 Conclusions of this thesis.....	110
6.2 Future works.....	110

References.....	113
Appendix A The conservation between physical units and LB units	125
Appendix B Difference scheme used in LBM	126

Chapter 1 Introduction

1.1 Background

Soil which is partially saturated with water is often referred to as unsaturated soil and the unsaturated soil zone spreads widely on the earth. Due to the fluctuation in the degree of saturation induced by nature or human activity (such as rainfall infiltration, evaporation, transpiration, hydraulic engineering projects, etc.), severe deformation or failure, like shrinkage, swelling or even collapse, might result in the unsaturated zone (Gens, 2010). Since most housing and transport facilities are founded in this zone, the deformation or failure phenomena may cause huge economic loss and even fatalities. In the UK, the adverse effects of shrink–swell behaviour cost an estimated £3 billion from 2002 to 2012, ranking as the most damaging geo-hazard in Britain today (Jones and Jefferson, 2012). In the US, the damage cost incited by the expansive soil exceeded that of all other natural hazards combined, including earthquakes, floods, fires and tornados (Lu and Likos, 2004). In Hong Kong, due to the intense seasonal rainfall, the man-made unsaturated slopes suffered significant variation in shear strength and several severe landslides have happened since the 1940s, including two fatal incidents on the same day in 1972, killing 138 people in total (Choi et al., 2013).

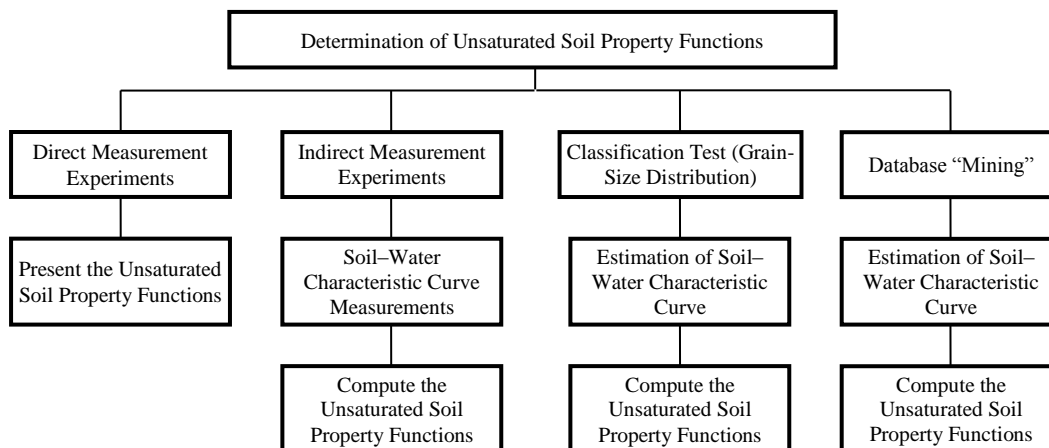


Figure 1-1 Methodologies for determination of unsaturated soil property functions (Fredlund et al., 2012)

With advances in experimental equipment for unsaturated soil, most unsaturated soil properties can be measured in laboratories; however, due to difficulties in controlling the matric suction (the suction originated from the capillary phenomenon and the

short-range interaction) (Lu and Likos, 2004), especially high suction value in experiments, it is still time-consuming and expensive to measure unsaturated soil properties for routine geotechnical engineering (Fredlund et al., 2012). Besides, since the late 1950s, Soil–Water Characteristic Curves (SWCCs) have been widely used in the unsaturated soil constitutive models and played a significant role in the estimation equations for unsaturated soil properties (illustrated in Figure 1-1) (Fredlund et al., 2012). Although the suction in unsaturated soils is mainly controlled by the Laplace Law, due to the complex pores' topologies, it is still difficult to predict the SWCC through experiments and analytical equations.

Alternatively, numerical simulations may provide a promising approach to studying the behaviour of the unsaturated soil and the Two-Phase Flow in the porous media with a large density ratio (1000:1) in unsaturated soil.

1.2 Numerical techniques for modelling multi-fluid flow in porous media

In recent years, a number of Computational Fluid Dynamics (CFD) techniques have been reported in the simulation of multi-fluid systems, including the Volume of Fluid (VOF) (Apsley and Hu, 2003; Galea et al., 2010), Level Set (LS) method (Menard et al., 2007), and Smoothed-Particle Hydrodynamics (SPH) (Monaghan, 1994; Toon et al., 2008). Nevertheless, due to the limitation of the computer performance and the complicated topology change of the meniscus shape, it is not easy for the CFD methods, which are based on Navier–Stokes (N–S) equations, to model the multiphase fluid flow in soil skeletons.

On the other hand, the Lattice Boltzmann (LB) method has shown a good performance in the Two-Phase Flow modelling in recent years. Rather than being based on the continuous N–S equations, the LB method is a mesoscopic numerical method based on the discrete kinematic equations, making it easier to capture the complex geometrical characters of the boundaries without decreasing the computational efficiency (Ladd, 1994; Feng and Michaelides, 2004; Pan et al., 2004; Tiwari and Vanka, 2012).

Besides, since the pioneering work of Rothman and Keller (1988), four major advances have been made in the two-phase fluid modelling with LB models (Shan

and Chen, 1993; Swift et al., 1995; He et al., 1999; Lee, 2004), and stable simulations of two-phase fluid with a large density ratio (1000:1) with rigid moving particles can now be realised (Lee, 2004; Lee and Lin, 2005; Connington and Lee, 2015).

Although the LB model proposed by Lee (Connington and Lee, 2015) can simulate the movement of solid particles in two-phase fluid, the ‘half-way’ boundary condition (as explained in Section 2.5.2) used in this model requires high grid resolution in order to capture the interaction characters between the fluids and moving particles accurately, which seriously affects the computational efficiency. Thus, the LB model proposed by Lee is used to simulate the interaction between two fluids, while the ‘half-way’ boundary condition is replaced by the Ghost Fluid Immersed Boundary (GFIB) method in this thesis.

1.3 Aim of this research

This thesis is primarily aimed at the development of the LB-GFIB model and its incorporation into an existing LB-DEM code to simulate the Two-Phase Flow on the curved boundaries and to predict the mechanical behaviour of the meniscus on the stationary curved solid boundaries using a new forcing calculation approach.

The main objectives of the project include:

- Incorporating the multiphase LB model proposed by Lee and the GFIB model into the existing FPS-BHAM and validating the new feature with the droplet test.
- Modifying the GFIB model with the corrected bounce back calculation method so that mass is conserved and less computationally expensively and incorporate it into the computer code and validating the it with the capillary rise test.
- Applying the new forcing calculation approach in the mechanical calculation of FPS-BHAM and validating it with the capillary bridge test and contact line dynamic test and validating the new updated code with the capillary rise in porous media test with stationary particles and verifying its ability in the Two-Phase Flow simulation.
- Performing parametric studies and assessing the computational requirement of the result computer code.

1.4 Thesis layout

This thesis is divided into six chapters. Chapter 2 provides a literature review of the experimental and numerical studies in the multiphase fluids flow in unsaturated soils and in porous media. Chapter 3 gives an introduction of the method used in this thesis, including the LB equations and the fluid-solid boundary interaction models. In Chapter 4, several numerical results are validated against the corresponding theoretical analytical solutions to gauge the accuracy of the code and in Chapter 5, the influence of four different parameters on the performance of the code are under investigation. Finally, in Chapter 6, conclusion on the overall work is presented and some future works are suggested.

Chapter 2 Literature Review

2.1 Introduction

Due to the importance of suction in the analysis of unsaturated soil, many experimental techniques and empirical equations have been proposed in the past 50 years. Furthermore, owing to the limitation of experiments, the Two-Phase Flow in porous media has been widely studied with different kinds of numerical tools after the emergence of Computational Fluid Dynamics.

As a result, a review of published research work in experimental and empirical works is presented in this chapter and the experimental and numerical ways in which to describe the Two-Phase Flow system are discussed. The review consists of four sections, namely the experiments and estimation for unsaturated soil in Section 2.2, the Computational Fluid Dynamics simulation for multiphase flow in Section 2.3, the Lattice Boltzmann method simulation for multi-fluid flow in Section 2.4, and the interaction model between the fluids and solid boundaries in Section 2.5.

2.2 Experiments and estimation for unsaturated soil

For the unsaturated soil, the suction force incurred by the capillary phenomena is the critical parameter in its analysis. As mentioned in Section 1.1, the relationship between the water content and suction (or the SWCC) provides critical information in the unsaturated soil study, including the seepage analysis, shear strength volume change, shear flow problems, etc. (Fredlund, 1997; Fredlund, 2000; Lu and Likos, 2004). In 1907, Buckingham first measured the suction under different water content in a variety of soils. Then, with the development of technology, the complex and accurate advanced experimental techniques with wider suction range measurement were invented for laboratory and field tests (shown in Table 2.1).

Table 2.1 Summary of common laboratory and field techniques for measuring soil suction (Lu and Likos, 2004)

Technique/Sensor	Practical Suction Range (kPa)	Laboratory/Field	Measurement Principle
Tensiometers	0–100	Laboratory/Field	Measuring the negative pore pressure through the high-air-entry ceramic tips in tensiometers directly
Axis translation techniques	0–1,500	Laboratory	Controlling pore pressure by increasing the air pressure and measuring the water content
Electrical/thermal conductivity sensors	0–400	Laboratory/Field	Measuring the electrical or thermal conductivities of the soil and determining the suction with predetermined calibration curve
Thermocouple psychrometers	100–8,000	Laboratory/Field	Measuring/controlling the humidity of the pore water and determining the suction through Kelvin's law
Chilled-mirror hygrometers	1,000–450,000	Laboratory	
Resistance/capacitance sensors	Entire range	Laboratory	
Isopiestic humidity control	4,000–400,000	Laboratory	Controlling the suction in experiments through the calibration of humidity based on Kelvin's law and measuring the water content
Two-pressure humidity control	10,000–600,000	Laboratory	
Noncontact filter paper method	1,000–500,000	Laboratory/Field	Measuring the water content in the noncontact filter papers in experiments and determining the suction with the corresponding calibration curves

Although the most accurate way in which to determine the suction in unsaturated soil nowadays is still through experimental methods, due to the high cost and time-consuming nature of the experiments (Fredlund et al., 1997), in the preliminary design stage of the practical geotechnical engineering project, the empirical equations are still used to predict the suction (Fredlund et al., 2012). In 1931, Richards proposed the first estimation equation for suction through a water flow equation. Later, Gardner as well as Brooks and Corey proposed two widely used equations in the early-stage construction design (Fredlund et al., 2012). Since the 1980s, Van Genuchten (1980), Bumb and McKee (1984 & 1987) and Fredlund et al. (Fredlund and Xing, 1994; Pham et al., 2005) have all proposed different closed-form, empirical equations for some particular groups of soil based on experimental data. Although each equation was originally proposed based on the experimental data and could be applied to a particular group of soil, due to the complicated change of suction when water content is low, few estimation equations can accurately fit the experimental data over the entire suction range with fitting parameters which have clear physical meanings.

Therefore, neither the experimental nor the empirical methods could offer a simple, cheap and accurate way in which to capture the basic characters of unsaturated soils. On the other hand, with the development of computational techniques in the multiphase fluid system in recent years, the numerical analysis provides an alternative approach to solving this problem. In the following sections, the literature review is mainly focussed on the numerical tools for simulating multi-fluid flow in unsaturated soil.

2.3 Computational Fluid Dynamics (CFD) simulation for multiphase flow

The prototype of two fluids' (water and air) flow in a soil skeleton can be simplified to the Two-Phase Flow with solid particles or in porous media, attracting much research on its complex behaviours with various numerical tools, such as Computational Fluid Dynamics (CFD) techniques.

As a branch of fluid mechanics, CFD uses numerical tools to solve and analyse fluid mechanics problems and many of them are expensive or even impossible in real experiments (Gomez et al., 2010). Generally, the fundamental basis of almost all CFD

models concerns the Navier–Stokes (N–S) equations, which represent a continuum statement of Newton’s Laws as follows:

$$\frac{\partial(\rho\mathbf{u})}{\partial t} + \nabla \cdot (\rho\mathbf{u}\otimes\mathbf{u}) = -\nabla p + \mathbf{F} + \mu\nabla^2\mathbf{u}, \quad (2.1)$$

where ρ , \mathbf{u} and μ represent the density, velocity and viscosity of a fluid, respectively, \mathbf{F} is the body force acting on the fluid, and p is the pressure. Due to the discontinuous fluid properties across the interface in multi-fluid flow, in conventional CFD methods, the moving interface between two different fluids is always regarded as a stress boundary and the surface tension at this interface is added into the N–S equation through the boundary condition.

There are two different frames applied for describing the N–S equations in CFD: the Eulerian description and the Lagrangian description. In the Eulerian description, a control volume is always pre-defined, within which the fluid properties are expressed as fields, while in the Lagrangian description, the fluid flow is described by tracking each individual fluid particle or particle cluster in the entire flow (Lagrangian and Eulerian specification of the flow field, 2015). For the widely used CFD approaches, the mesh sizes in the Eulerian–Eulerian (E–E) method and the Eulerian–Lagrangian (E–L) method are always larger than the size of secondary phases (bubbles, particles, droplets, etc.) in the computation, while in Direct Numerical Simulation (Yang et al., 2007), the typically small grid size is always applied in the modelling.

2.3.1 Eulerian–Eulerian method and Eulerian–Lagrangian method

In the Eulerian–Eulerian (E–E) method, only the droplets or bubbles dispersed in the continuous fluid phase can be simulated. As interpenetrating continuous media, each phase in these two models would possess the same space but different velocities and volume fractions (Garcia et al., 2005; Yang et al., 2007). In the E–E method, the dispersed droplets and bubbles are called the secondary phase while the continuous fluid is called the primary phase. Besides, in the E–E method, the relationship of stress and velocity in the interface between two different fluids should be formulated as the closure condition and sometimes it is hard to be expressed due to the variation in pressure and shear stress on the surface (Sokolichin and Eigenberger, 1994).

In the Eulerian–Lagrangian (E–L) method, there are also the primary and secondary phases in the model; unlike the E–E method, the specific motion of continuous

primary fluid in the vicinity of the secondary phase (i.e. droplets, bubbles and solid particles) is neglected in the simulation. Primary fluid with a large meshed grid is calculated in the Eulerian mode, and the secondary phase, which is always much smaller than the fluid grid, is traced in the Lagrangian mode (as illustrated in Figure 2-1).

The secondary phase, including the bubbles, droplets and particles, is distributed uniformly in the fluid cell with the same physical quantities (such as velocity, mass, capillary force, etc.) and their effects on the primary phase are also averaged within the cell. In other words, instead of being calculated individually in the simulation, the secondary phase in the E–L method works as a ‘whole’ particle in the Navier–Stokes equation computation in each fluid cell (Anderson and Jackson, 1968; Tsuji et al., 1993; Tsuji, 2007).

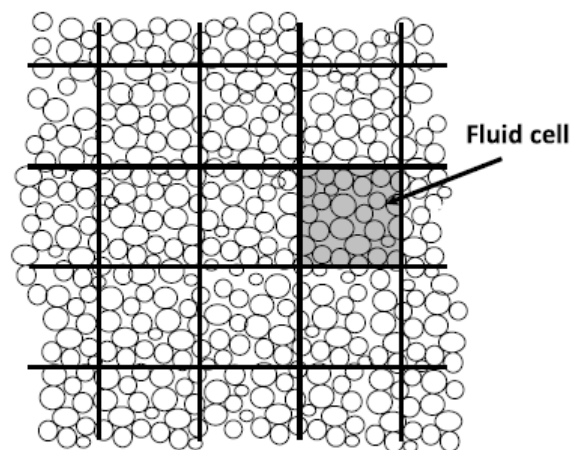


Figure 2-1 Schematic diagram of the coarse-grid approach used in the DEM-CFD model, where the size of the Eulerian cell is much larger than that of the Lagrangian solid particles (O’Sullivan, 2011)

For the two-phase fluid simulation in the pore scale, the topology shape of the meniscus might be complicated (as illustrated in Figure 2-2, showing a numerical simulation of the pressure-plate test with LBM) and neither the E–E method nor the E–L method can easily capture the geometrical characters of the fluid interface just with simple geometrical shapes. In addition, the capillary force, incurred by the surface tension, is controlled by the shape of the interface, which can hardly be accurately calculated with an averaging method in the E–L method. As a result, both the E–E and E–L techniques cannot be applied in this thesis for the simulation of multi-phase fluid flow in a porous media system.

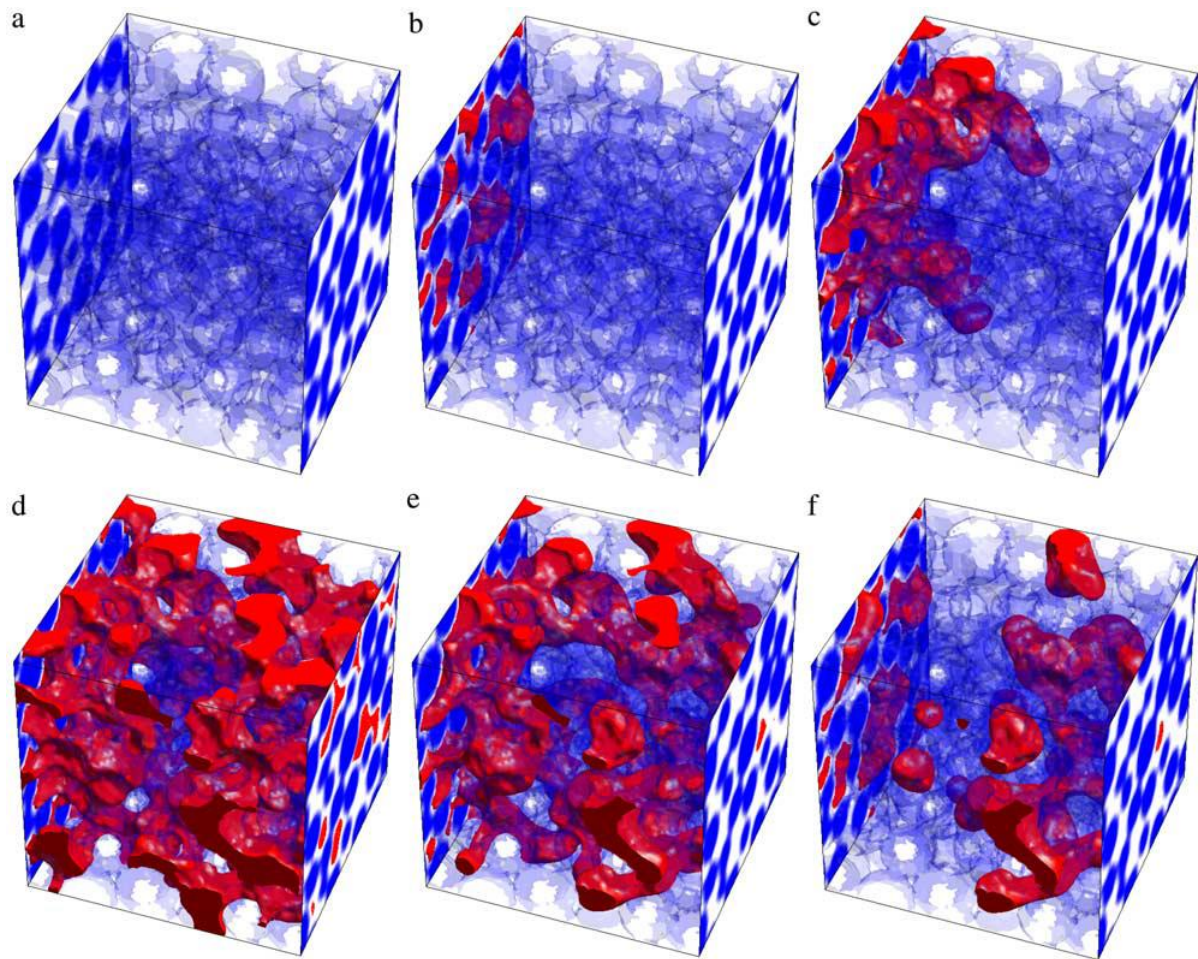


Figure 2-2 Distribution of the non-wetting phase during a primary drainage and imbibition simulation in a porous media system. The transparent blue surface indicates the interface between the pore space and the solid phase. Red parts represent the non-wetting fluid. The wetting fluid is not shown for the clarity of illustration (Pan et al., 2004)

2.3.2 Direct Numerical Simulation method

The origin of the term “Direct Numerical Simulation” (DNS) owes to the much smaller mesh size (compared with the E–L and E–E methods) used to simulate the turbulence in fluid. It is found that the typically small grid size also helps to track or capture the moving interface in the simulation of multiphase fluid flow (Coleman and Sandberg, 2010). For the DNS method, in terms of the gridding method, it can be categorised as a moving grid method, fixed grid method and free grid method.

Moving Grid Method

Like in the E–E method, the interface in the moving grid method is also regarded as a boundary between two different fluids with no physical convection and diffusion

across the interface. Besides, the two fluid subdomains are also meshed individually in the numerical computation (Zwart et al., 1999). Yet, in the modelling, since the interface can hardly be static, the re-meshing would be a time-consuming and complicated process, especially when an interface topology change occurs in the simulation, e.g. coalescence, break-up, nucleation, etc.

Fixed Grid Method

The fixed grid method, which is also known as the continuous interface method, treats two different fluids as a single flow with the density and viscosity varying smoothly across a finite thickness of the interface (Yang et al., 2007). According to the numerical technique applied on the interface, there are two categories: the front-tracking method and the front-capturing method.

For the front-tracking method, Glimm and his collaborators (Glimm et al., 2001) used to apply the marker particles to track the location of the interface explicitly and reconstruct the interface with a triangular (3D) or piecewise linear (2D) in the model. Although Tryggvason (Tryggvason et al., 2001) improved the interface reconstruction technique and can even simulate the complicated interface changes in the classical Rayleigh–Taylor instability test, due to the complex solid boundary problem in this thesis, the precise description of the interface location is still a computationally expensive task for the model.

For the front-capturing method, the concept of a diffuse interface (illustrated in Figure 2-3) is proposed (Anderson et al., 1998) to smooth the physical properties' discontinuity across the interface. In this method, the interface is implicitly represented by a scalar indicator function defined on a fixed regular mesh and the movement of the interface is captured by solving the advection equation of the scalar indicator equation (Yang et al., 2007). The two widely used CFD methods — Volume of Fluid (VOF) and Level Set (LS) — belong to this technique. In the VOF, a volume fraction, whose value lies between 0 and 1, is defined to denote whether a space is occupied by the dispersed phase or continuous phase. VOF can deal with the sharp topology change with mass conservation easily; however, due to the limitation of the volume fraction function, it is difficult to obtain the accurate curvature of the interface. In other words, the VOF is unable to predict the multiphase fluid flow in porous

media accurately when surface tension is a key factor in the movement of the interface, like the problem considered in this thesis (Lee et al., 2011).

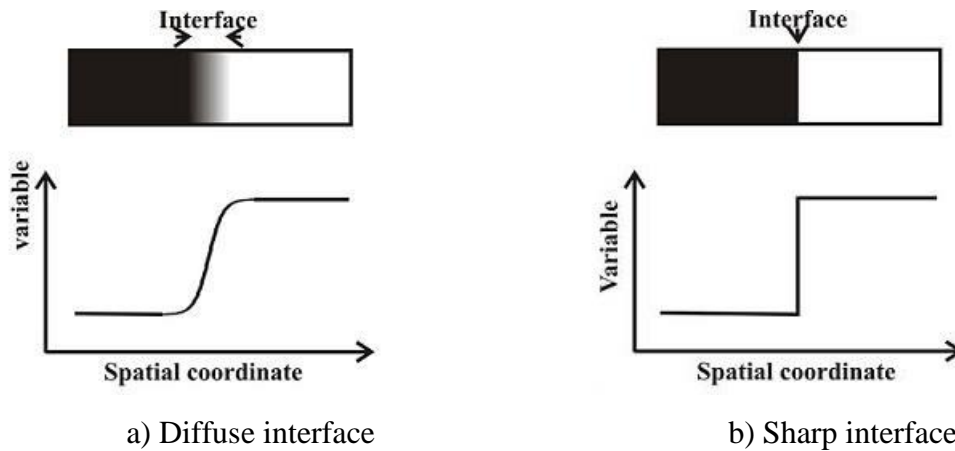


Figure 2-3 Schematic figures of two different interface models (Microstructure Modelling, 2015)

In the LS method, the level set function is introduced to represent the moving interface implicitly. In contrast to the VOF, the LS method can accurately compute the interface curvature and the smoothness of discontinuous physical properties near the interface is much better than that in VOF. However, for the LS method, the mass conservation can hardly be obtained in the computation, especially when the interface experiences severe topology changes (Sun and Tao, 2010).

For the front-tracking method, the re-meshing of the interface would be time-consuming and the significant topology change would also be a challenge for simulation. For the front-capturing method, the precise definition of interface curvature and the computational error limit the application of VOF and LS methods in this thesis respectively. Therefore, neither of these two methods can be applied in this thesis.

Free Grid Method

The fluid property discontinuity, especially the large density jump, across the interface presents a challenge for moving grid methods and fixed grid methods due to numerical instability near the interface. In order to eliminate the problem, free grid methods (or the “mesh-free” methods), such as Dissipative Particle Dynamics (DPD) and Smoothed-Particle Hydrodynamics (SPH), have been developed to simulate the multiphase flow by dividing the fluids into a set of off-lattice particles, which represent a physical object or a parcel of the domain (Scardovelli and Zaleski, 1999;

Liu and Liu, 2010). Unlike DPD, which mainly simulates polymeric fluids in volumes up to 100 nm (Dissipative particle dynamics, 2015), SPH is arguably the most popular mesh-free method for modelling mass flow and heat transfer on a macro-scale (Sawley et al., 1999; Gomez et al., 2010).

SPH is based on the integral interpolants and the fundamental principle is the combination of the Navier–Stokes equations in fluid dynamics and the kernel density estimation (KDE) in statistics. In SPH, any function $A(\mathbf{r})$ and its gradient at a particle a can be expressed by:

$$A(\mathbf{r}) \approx \sum_b m_b \frac{A_b}{\rho_b} W_{ab}, \quad (2.2)$$

$$\nabla A(\mathbf{r}) \approx \sum_b m_b \frac{A_b}{\rho_b} \nabla W_{ab}, \quad (2.3)$$

where \mathbf{r} is the vector position, m and ρ are mass and density respectively, and W is the weighting function or the kernel (Crespo, 2008). Since the expression of the kernel is predefined, the complex differentiable computation in Navier–Stokes equations can be simply constructed from the summation process in SPH, avoiding the numerical instability near the interface (Gomez et al., 2010).

On the other hand, with explicit surface tension expression (Morris, 2000; Tartakovsky and Meaking, 2005; Akinici et al., 2013) and the stationary particles representing the solid boundary, it is convenient to simulate the behaviour of multiphase fluid flow in porous media in the SPH model (Hu and Adams, 2006; Meaking and Tartakovsky, 2009) and successful SPH simulation has already been undertaken in the last few years (Tartakovsky et al., 2007; Ryan et al., 2011).

In order to describe the motion of a free surface, large numbers of particles are required in SPH simulation, leading to the low computational efficiency in the modelling in this thesis. Besides, since the fluid in SPH is composed of numerous discrete nodes, some physical properties of continuous fluid, such as viscosity, can hardly be defined by those discrete particles in SPH (Li, 2013). As a result, SPH still cannot be regarded as an idealised approach in the multiphase fluid flow in porous media considered in this thesis.

2.3.3 Summary of CFD methods

Although with the progress of the CFD methods, the multiphase fluid flow can be simulated with many numerical techniques, due to the complex boundary of the porous media and it being difficult to simulate the interface with complex topology changes, it is not appropriate to apply the E–E and E–L methods in this project. Besides, for the DNS method, the capture of the interface between two different fluids would be time-consuming and pose a challenge for the numerical simulation, though it is applicable theoretically.

As a result, the conventional CFD methods can hardly be used in this thesis to simulate the multiphase flow in porous media.

2.4 Lattice Boltzmann (LB) method

The Lattice Boltzmann (LB) method, originating from the Lattice Gas Automata (LGA), simulates the motion of fluids within discrete lattices and discrete time. Unlike the numerical methods in CFD, the LB method is based on the microscopic models and mesoscopic kinetic equations (Chen and Doolen, 1998). With the basic premise that the macroscopic physical properties are the collective behaviour of microscopic particles in the model, the LB method only focuses on the local calculation of kinetic distribution probability and data streaming with neighbouring particles (Benzi et al., 1992). The kinetic nature of the LB method helps it to keep both the advantages of continuous numerical methods (such as clear physical quantities in governing equations and acceptable computation cost) and those of discrete numerical methods (such as those suitable for parallelisation) (Chen and Doolen, 1998).

Besides, the Lattice Bhatnagar–Gross–Krook (LBGK) LB model (shown in equations (2.4)–(2.6)), proposed in the early 1990s and widely used nowadays, can be recovered to Navier–Stokes equations with second-order accuracy on a macro-scale (Chen et al., 1991; Shan and Chen, 1993):

$$\frac{\partial f}{\partial t} + \boldsymbol{\xi} \cdot \nabla f = -\frac{f-f^{eq}}{\lambda} + \frac{(\boldsymbol{\xi}-\mathbf{u}) \cdot (\mathbf{F}+\mathbf{G})}{\rho RT} f^{eq}, \quad (2.4)$$

$$\rho = \int f d\boldsymbol{\xi}, \quad (2.5)$$

$$\rho \mathbf{u} = \int \boldsymbol{\xi} f d\boldsymbol{\xi}, \quad (2.6)$$

where f is the single particle density distribution function in the phase space, f^{eq} is the equilibrium distribution function, ξ is the microscopic velocity, λ is the relaxation time, R is the gas constant, ρ is the density, T is the temperature, F is the effective molecular interaction force, and G is the gravity (He et al., 1999).

With these advantages, the LB method shows good ability in fluid modelling (Rothman and Keller, 1988; Succi et al., 1989; Shan and Doolen, 2008; Hao and Cheng, 2010) and even the simulation of multiphase fluid flow at pore level (Pan et al., 2004).

2.4.1 LB models and their applications in multiphase fluid flow

Up to now, mainly four different kinds of multiphase LB models have been proposed based on the LBGK LB model since 1988 (He et al., 1998): the Chromodynamic model (Rothman and Keller, 1988), the Pseudo-potential (Shan/Chen) model (Shan and Chen, 1993), the Free-Energy model (Swift et al., 1995), and the modified Pseudo-potential model (He/Lee model) (He et al., 1999; Lee, 2004).

The first Two-Phase Flow LB model, the so-called Chromodynamic model, was proposed by Rothman and Keller (Rothman and Keller, 1988) and modified by Gunstensen et al. (1991) for immiscible two-phase flow simulation. By introducing two-particle distributions for the two different fluids, each fluid obeys its own LBGK equations (similar to equation (2.4)) and a source term S (which can be regarded as the forcing term, the second term on the right-hand side of equation (2.4)) is applied in the model to represent the mesoscopic interaction between these two. Meanwhile, due to the highly heuristic expression of the term S in the model (in other words, the expression of S is directly defined by the authors based on the fluid characteristics and can even hardly ensure the mass conservation of each fluid in the simulation), it is difficult to incorporate microscopic physics into the model (Pan et al., 2004) and the parasite currents (a small-amplitude artificial velocity field) are always discovered near the interface in the simulation (Succi, 2001; He and Doolen, 2002). In 1991, Gunstensen (Gunstensen et al., 1991) succeeded in modelling the evolution of a two-phase flow in a microscopic model of a porous medium; however, because of the instability incurred by the parasite currents in the computation, the reasonable results could only be obtained at a low density ratio (<10) with the Chromodynamic model (He and Doolen, 2002).

Later, Shan and Chen (1993) proposed the Pseudo-potential LB model to get a more satisfactory result compared with the previous model. In the Pseudo-potential LB model, a pairwise interaction potential is incorporated into the forcing term and a more physically oriented expression has been obtained compared with Rothman's model. Although the local momentum still cannot be conserved in the Shan/Chen model, the system's global momentum conservation is exactly satisfied when the boundary effects are excluded (Pan et al., 2004). In 1995, Swift et al. (1995) made a further improvement and imposed an additional constrain on the equilibrium distribution functions (explained in Section 3.1.1) in the model to conserve the mass and momentums locally and globally (Succi, 2001; Pan et al., 2004). In these two models, however, the parasite currents still cannot be eliminated near the interface due to the truncation error in intermolecular force F computation. These parasite currents can be reduced with large viscous dissipation, but in most cases never disappear (Lee and Fischer, 2006) and incur severe numerical instability when the density ratio is larger than 10 (Connington and Lee, 2012). Therefore, as with the Chromodynamic model, the Pseudo-potential model and the Free-Energy model still have difficulties in simulating the large density ratio problem in this thesis due to the limitation of numerical errors in computation.

In 1999, He et al. modified the Pseudo-potential LB model by incorporating a pressure distribution function to describe the total pressure in the model (He et al., 1999). Meanwhile, they projected distribution functions to decrease the numerical error in previous models and reduced the parasite current efficiently. Later, Lee and Lin (2005) incorporated the Cahn–Hilliard theory into the model to describe the behaviour of multiphase fluid flow, and also updated the pressure distribution function form to obtain a more stable result, within which the density ratio between two fluids in LB simulation can first reach 1.0×10^3 (Lee and Lin, 2005). As a result, the modified Pseudo-potential model could be regarded as an effective technique to simulate the multiphase flow with a large density ratio in this thesis. A further review of the He/Lee LB model is presented in the next section.

2.4.2 Modified Pseudo-potential LB model and its application in multiphase fluid flow

In order to reduce the parasite current in the simulation, the intermolecular force in the modified Pseudo-potential LB model is expressed as:

$$\mathbf{F} = -\nabla\psi(\rho) + F_s, \quad (2.7)$$

where $F_s = \kappa\rho\nabla\nabla^2\rho$, κ is a parameter related to the surface tension, and $\psi(\rho) = p - \rho RT$ is a function of density ρ and pressure p (He et al., 1999).

Due to the density jump across the interface in multi-fluid flow in most cases, even small numerical errors in finite difference calculation of $\nabla\psi$ in equation (2.7) might generate the parasite currents in the vicinity of the interface, limiting the density ratio between two different fluids in the LB model. To minimise the influence of the error, He et al. (1999) introduced a new variable g into the model as:

$$g = fRT + \psi(\rho)\Gamma(0), \quad (2.8)$$

$$\Gamma(\mathbf{u}) = \frac{1}{(2\pi RT)^{D/2}} \exp\left[-\frac{(\xi-\mathbf{u})^2}{2RT}\right]. \quad (2.9)$$

Similar to equations (2.4)–(2.6), the evolution equation for g in the incompressible fluids model can be expressed as follows:

$$\frac{\partial g}{\partial t} + \xi \cdot \nabla g = -\frac{g-g^{eq}}{\lambda} + (\xi - \mathbf{u}) \cdot [\Gamma(\mathbf{u})(\mathbf{F}_s + \mathbf{G}) - (\Gamma(\mathbf{u}) - \Gamma(0))\nabla\psi(\rho)], \quad (2.10)$$

$$p = \int g d\xi, \quad (2.11)$$

$$\rho RT \mathbf{u} = \int \xi g d\xi. \quad (2.12)$$

In equation (2.10), the effect of the numerical errors for pressure and velocity in the calculation of intermolecular force is reduced by the second order of infinitesimal term $\Gamma(\mathbf{u}) - \Gamma(0)$ (He et al., 1999). However, the calculation of density with equation (2.5) in He's model is still influenced by the fluid property variation in the vicinity of the interface.

In 2004, Lee (Lee, 2004; Lee and Lin, 2005) recast the term of surface tension in equation (2.7) with a potential form for the calculation of density — a great

improvement in the reduction of the parasite current in the numerical calculation had been achieved. With the modified model, it is the first time that the numerical bubble test with a large density ratio (1000:1) is realised with the LB model (Lee, 2004).

In 2009, the Cahn–Hilliard diffusion model was introduced into Lee’s model to maintain the phase interface between two fluids and the intermolecular forcing term was replaced as follows:

$$\mathbf{F} = -\nabla\rho c_s^2 - (\nabla p_0 - C\nabla\mu), \quad (2.13)$$

where c_s^2 is a parameter related to RT and always equals $1/3$ in simulation, p_0 is the dynamic pressure to ensure the incompressibility of the LB model, C is the composition of the fluid (which can be expressed as $C = \frac{\rho - \rho_{gas}}{\rho_{liquid} - \rho_{gas}}$, where ρ is the particle density on the corresponding point and ρ_{gas} and ρ_{liquid} are the density of gas and liquid in the model respectively), $\mu = \mu_0 - \kappa\nabla^2 C$ is the chemical potential, and $\mu_0 = \frac{\partial E_0}{\partial C} = \frac{\partial \beta C^2 (C-1)^2}{\partial C}$ is a parameter related to the bulk energy E_0 , with β being a constant and κ the gradient parameter.

With the proper selection of parameters, the parasitic currents in an equilibrium state can be eliminated to the round-off level, which means that the parasitic currents in an equilibrium state almost have no influence on the numerical simulation of fluids motion (Lee, 2009).

Therefore, the modified Pseudo-potential model proposed by Lee is used in this thesis to simulate the multiphase phase flow due to its good performance in eliminating the parasitic currents in the simulation. However, for the porous media system, the complex solid boundary still poses a challenge to the numerical simulation. In the next section, the techniques dealing with the interaction between the fluids and solid boundaries in the LB model are reviewed and proper solid boundary methods are chosen to be applied in this thesis.

2.5 The solid–fluid boundary condition in LBM

The interaction problem between the multiphase fluids and the solid walls in the LB model can be divided into two parts: how to incorporate the wetting dynamic properties of the solid surface into the LB model and how to calculate the unknown values on the LB nodes occupied by the solid particles. Thus, in the following, the

boundary condition with dynamic wetting and the curved boundary condition applied in the LB model will be studied.

2.5.1 Boundary condition with dynamic wetting in LBM

When one fluid displaces another fluid on a solid surface, a triple contact line is formed at the intersection of these three phases (illustrated in Figure 2-4). If the three-phase contact line is in continuous motion, it is called dynamic wetting or spreading and the angle between the moving contact line (the dashed line in Figure 2-4) and the solid surface is defined as the dynamic contact angle (the angle θ as illustrated in Figure 2-4) (Lu and Likos, 2004; Liu and Lee, 2009).

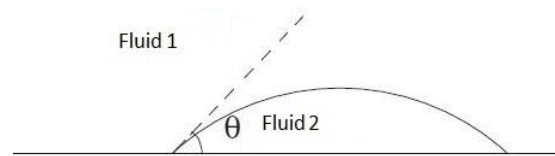


Figure 2-4 The schematic figure of the contact line

In LBM, since the early 1990s, the behaviour of various boundary conditions has been investigated widely (Sukop and Thorne, 2006) and mainly three of them could be applied in the description of the moving contact line on the solid wall surface: the external forcing approach, the coating approach, and the additional free energy approach (Lee and Lin, 2008).

In the external forcing approach, it assumes that when a drop contacts a solid surface, interaction forces F_w will take effect between the drop and the surface molecules. The value of the contact angle is determined by the interaction forces and the intermolecular forcing term in equation (2.4) should also be modified with the interaction forces (Huang et al., 2007; Mukherjee and Abraham, 2007). Although the external forcing method can be easily imposed in the model, due to the nonzero potential gradient along the normal direction to the boundary, it is difficult to conserve mass across the boundary nodes, which may provoke the parasitic currents near the boundary (Lee and Lin, 2008).

In the coating approach, in order to simulate the wetting conditions in the model, a layer of fluid particles is fixed on the boundary wall with a certain constant density. The contact force and angle can be achieved by a proper definition of dynamic wetting parameters among three different kinds of fluids in the model (Fan et al., 2001;

Kuksenok et al., 2002). However, in the LB model, the fluid particle density calculated by equation (2.5) is always inconsistent with the fixed wall density in the coating approach. Therefore, in the coating approach, mass conservation cannot be satisfied and the parasitic currents still exist in the computation (Lee and Lin, 2008).

In 2008, based on the modified Pseudo-potential model by Lee and the Van Der Waals theory, Lee and Lin (Lee and Lin, 2008; Liu and Lee, 2009) introduced an additional wall free energy into free energy and the new free energy can be expressed as:

$$E_f = \int_V \left(E_0(C) + \frac{\kappa}{2} |\nabla C|^2 \right) dV + \int_S (\phi_0 - \phi_1 C_s + \phi_2 C_s^2 - \phi_3 C_s^3 + \dots) dS, \quad (2.14)$$

where the first integrand on the right side of the equation represents the free energy of fluid particles and the second one represents the free energy increased due to the wall effect. $E_0 = \beta C^2 (C - 1)^2$ is the bulk energy, C is the composition of the fluid, C_s is the composition at a solid surface, and ϕ_i with $i=0,1,2,\dots$ are constant coefficients (Lee and Liu, 2010).

Since the numerical model is in the equilibrium state, the total free energy should be minimised all of the time in the simulation, in which an additional Neumann boundary condition (the governing equation of the boundary condition is in a partial differential form) for the calculation of chemical potential μ is imposed according to equation (2.14) as:

$$\mathbf{n} \cdot \nabla C = -\frac{\phi}{\kappa}, \quad (2.15)$$

where \mathbf{n} is the unit normal vector for the boundary wall in the model and ϕ is related to the wall free energy.

For the points near the flat wall boundary in the LB model, a simple mirror method is used to evaluate the first and second derivatives of the physical quantities ϕ (shown in Figure 2-5) required in equations (2.13) and (2.15).

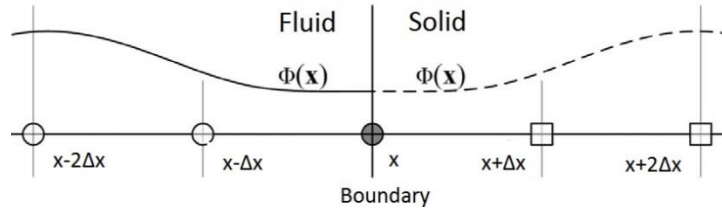


Figure 2-5 Profile of unknown variables in the solid taken as a mirror image in the fluid (Lee, 2009)

Based on the above model, Connington and Lee (2013) studied the water drop movement on a superhydrophobic surface (the surface which is extremely difficult to wet) with LB models in 2D and 3D and a good agreement had been achieved with the experimental contact angles of drops on the same property surface (Connington and Lee, 2013). Besides, the parasitic currents could also be eliminated to round-off with the additional free wall energy in the LB model.

2.5.2 Curved boundary condition in LBM

For the flat wall boundary, the mirror method could provide a simple approach to predicting the unknown variables inside the wall. However, it is difficult to determine the physical variables for the curved boundaries, like the circular particle boundary shown in Figure 2-6, since the mirror points would not be found easily on the lattice points.

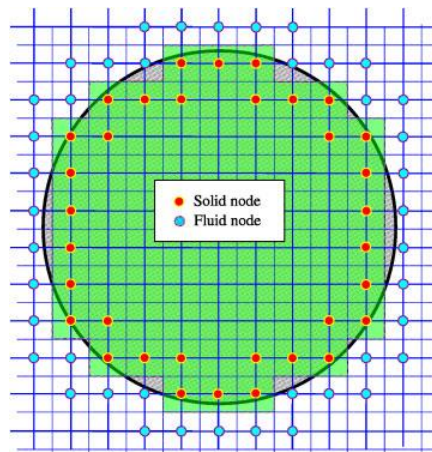


Figure 2-6 Lattice representation of a circular solid particle (Feng et al., 2007)

Based on the half-way method proposed by Ladd in the early 1990s (Ladd, 1994), Lee et al. implemented the boundary condition in equation (2.15) with the virtual stepwise boundary (the black points in Figure 2-7) instead of the real curved boundary (the dashed line in Figure 2-7) (Connington et al., 2015). Due to the simple geometrical

character for the stepwise boundary, the mirror scheme can be used directly. However, for the problems with geometric complexity, the half-way method would require extremely fine meshes to capture the details of the particle boundaries, which will be computationally expensive for this thesis.

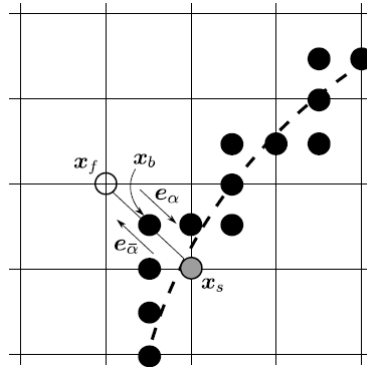


Figure 2-7 A representation of a curved boundary mapped onto the lattice (Connington and Lee, 2015)

In 1972, in order to simulate the flow of blood in the heart, Peskin (1972) proposed the Immersed Boundary Method (IBM) to deal with the complex geometrical boundary of the heart in the numerical model. In this method, the fluid domain is meshed with fixed Eulerian nodes while the solid boundaries are divided by the Lagrangian points (shown in Figure 2-8). The physical boundaries in IB models are treated as a deformable particle with high stiffness. Due to the difference between the interpolation velocity from Eulerian points and the one from Lagrangian points in every time step, small distortion happens on the boundary, yielding a force tending to restore the boundary in its original shape. Then the balance of the force will be distributed into fluid Eulerian nodes to work as a body force in the CFD or LB method.

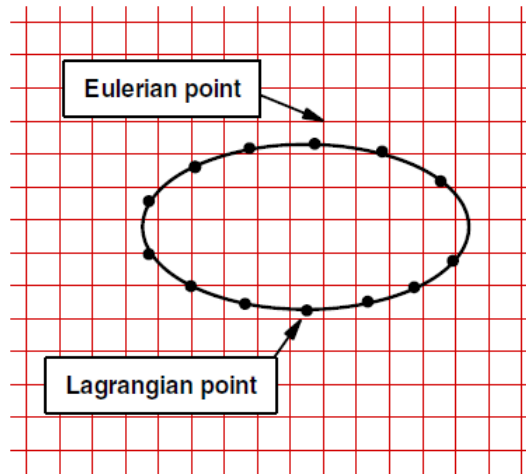


Figure 2-8 The schematic diagram about the IB method (Wu and Shu, 2009)

In 2004, Feng and Michaelides (2004) introduced the Immersed Boundary Method (IBM) with the LB method to simulate the sedimentation of circular particles in a viscous fluid and found a more accurate result with less fluctuation of particle forces and velocities than that with the previous half-way method under the same resolution. However, the value of the user-defined spring parameter in Feng's IB-LB model poses a significant effect on the accuracy result. In 2006 and 2007, based on the non-slip boundary condition and the implicit velocity assumption, Shu and his collaborators (Niu et al., 2006; Shu et al., 2007) updated the IB-LBM model to eliminate the user-defined parameter in Feng's model and improve the convergent rate in numerical computation.

Although the IB-LB model has already been proposed more than 10 years, to the best of the author's knowledge, only two IB-LB models could simulate the contact line dynamics while considering the Neumann boundary condition. In 2013, Shao et al. (2013) incorporated the Neumann boundary condition into the IB-LB model with the flux controlled assumption. However, since the new governing equations about the flux control are not in closed form, the mass conservation can hardly be realised in the simulation, i.e. the parasite currents in this model still cannot be ignored.

Based on the principle of the Ghost Cell Immersed Boundary Method (GC-IBM) (Tseng and Ferziger, 2003), Tiwari and Vanka (2012) proposed the Ghost Fluid Lattice Boltzmann (GF-LB) method (shown in Figure 2-9). Unlike previous IBM models, the Ghost Fluid IBM extrapolates values to nodes outside the fluid domain

boundary using the hydrodynamic boundary conditions (including the Neumann boundary condition).

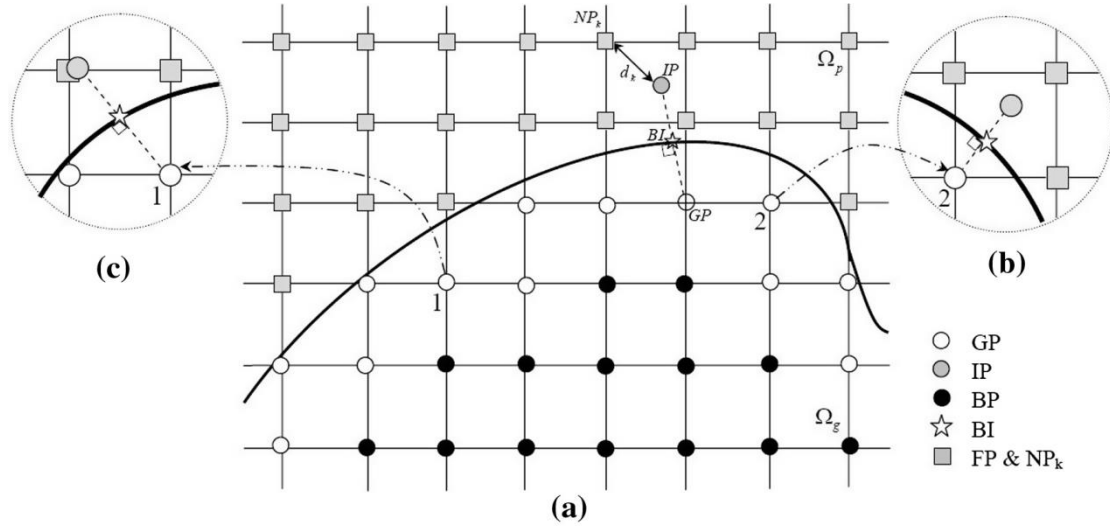


Figure 2-9 The schematic diagram about GF-LBM (Khazaeli et al., 2013)

After the identification of ghost cells, the density, velocity and chemical potential values of ghost nodes can be obtained from extrapolated mirror image points in the fluid domain. In most cases, the extrapolated point can hardly be located on the LB nodes exactly, so the bilinear interpolation with the four surrounding points will be used to find values at the image point. If some of the four surrounding points are interior, as shown in Figure 2-9(b), special treatment will be used to move reference points to the boundary and a boundary condition assumption will then be used directly.

2.5.3 Summary of boundary conditions in LBM

Due to the good performance in eliminating the parasite currents in the numerical simulation (Lee, 2009; Connington and Lee, 2015), the wall free energy boundary condition proposed by Lee will be used in this thesis to model the interaction phenomenon between the multiphase fluids and the solid boundary. For the LB nodes covered by the solid particles, the GF-LB model will be applied to extrapolate the unknown physical quantity values of ghost nodes from those of the fluid nodes in the simulation.

2.6 Summary

In this chapter, the literature review about the experimental and numerical techniques related to the suction inside the unsaturated soil or the porous media has been presented. Because of the time consumption and expensive cost of the laboratory tests and the low accuracy of the empirical equations, the numerical technique offers an effective way in which to study the complex flow in the porous media system.

Due to the limitation of the CFD methods and large density ratios (1000:1) between two fluids simulated in this thesis, the modified Pseudo-potential model proposed by Lee will be applied in the modelling due to its stable numerical computation performance for large density ratio problems. Besides, in order to simulate the contact line dynamic phenomenon between the multiphase fluids and the curved solid boundaries, the wall free energy boundary condition proposed by Lee and the GF-LB model are both incorporated into the numerical model in this thesis.

Chapter 3 Methodology

In this chapter, the Lattice Boltzmann model proposed by Lee (2009) will be first analysed in section 3.1 with detailed descriptions about the evolution equations proposed by Lee (2009) and the main LB equations used for the binary fluids in his model. Then, the interaction models between the multiphase fluids and the solid boundary are presented in section 3.2, including the free energy wall boundary condition in section 3.2.1 and the Ghost Fluid Immersed Boundary Method in section 3.2.2.

With the equations mentioned in this Chapter, a code based on the *FPS-BHAM* (Li, 2013) is developed to simulate the multiphase fluids flow in porous media and the validation and verification will be presented in Chapter 4.

3.1 Lattice Boltzmann (LB) method

In this section, the LB equations and the evolution equations for the component proposed by Lee (Lee and Lin, 2008; Lee, 2009) used in this thesis are presented in detail. Since the modified Pseudo Potential LB model is still based on the Lattice Bhatnagar-Gross-Krook (LBGK) model proposed in the early 1990s (Lee and Lin, 2005), the basic equations of the LBGK model are first presented in section 3.1.1. Then, the Cahn-Hilliard model, which represents the binary fluids movement in Lee's model, is presented in section 3.1.2. The LB equations used in Lee's model and a derivation process are illustrated in section 3.1.3.

3.1.1 Basic formulation used in LBM (two dimensions)

In LBM, the fluid domain is divided into a square lattice with unity spacing and the fluid is assumed to be a package of micro-particles residing on each lattice node. In this thesis, the D2Q9 model is used, in which the velocity field in two dimensions is discretised into nine prescribed vectors (see Figure 3-1), In every time step, the fluid particles can either remain at their current locations (referring to the zero velocity \mathbf{e}_0) or travel to their adjacent nodes with velocities \mathbf{e}_i ($i=1, \dots, 8$). (Li, 2013)

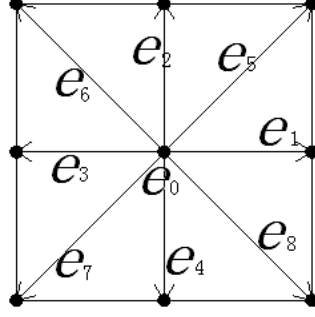


Figure 3-1 a typical lattice in D2Q9

As shown in Figure 3-1, the prescribed velocities in a D2Q9 model are defined as,

$$\mathbf{e}_0 = (0,0), \quad (3.1)$$

$$\mathbf{e}_i = C_L \left(\cos \left\{ \frac{\pi(i-1)}{2} \right\}, \sin \left\{ \frac{\pi(i-1)}{2} \right\} \right) (i = 1,2,3,4), \quad (3.2)$$

$$\mathbf{e}_i = \sqrt{2} \cdot C_L \left(\cos \left\{ \frac{\pi(2i-9)}{4} \right\}, \sin \left\{ \frac{\pi(2i-9)}{4} \right\} \right) (i = 5,6,7,8), \quad (3.3)$$

where $C_L = \Delta h / \Delta t$ refers to the lattice speed, Δh is the unity lattice spacing and Δt is the LBM time step. In LBM, the lattice speed is always chosen as 1 for simplicity of numerical computation. Therefore, a list is provided for the conversion of relevant physical variables with the lattice units in Appendix A .

As shown in equation (2.4), the governing equation of LBM BGK model can be discretized as (Lee and Lin, 2005),

$$f_i(\mathbf{x} + \mathbf{e}_i \Delta t, t + \Delta t) = f_i(\mathbf{x}, t) - \frac{f_i(\mathbf{x}, t) - f_i^{eq}(\mathbf{x}, t)}{\tau} + \frac{(\mathbf{e}_i - \mathbf{u}) \cdot (\mathbf{F} + \mathbf{G})}{\rho c_s^2} f_i^{eq}(\mathbf{x}, t), \quad (3.4)$$

where $f_i(\mathbf{x}, t)$ represents the probable quantity of micro-particles at \mathbf{x} along i -th direction with velocity \mathbf{e}_i at time t , τ is the relaxation time and f_i^{eq} represents the equilibrium state of distribution functions which can be expressed as: (Chen and Doolen, 1998)

$$f_i^{eq} = \omega_i \rho \left[1 + 3(\mathbf{e}_i \cdot \mathbf{u}) + \frac{9}{2}(\mathbf{e}_i \cdot \mathbf{u})^2 - \frac{3}{2} \mathbf{u} \cdot \mathbf{u} \right], \quad (3.5)$$

where ω_i is the weighting parameter and $\omega_0=4/9$, $\omega_i=1/9$ ($i=1, \dots, 4$) and $\omega_i=1/36$ ($i=5, \dots, 8$).

3.1.2 Cahn-Hilliard model

In the binary fluids flow in LB model, it is assumed that the density function of each fluid lattice point is consisted of two different fluids and a new variable, composition C , is introduced to describe the percentage of the heavier fluid at the corresponding point (Lee and Lin, 2010). Based on the definition of composition, the mixture density ρ can be recast as the linear function of composition C as:

$$\rho = \rho_1 \cdot C + \rho_2 \cdot (1 - C), \quad (3.6)$$

here ρ_1 and ρ_2 stands for the density of heavier fluids and lighter fluids, respectively.

On the other hand, C can also be defined as $C = \frac{\hat{\rho}_1}{\rho_1}$, where $\hat{\rho}_1$ stands for the mass of heavier fluid in a unit volume in that fluid lattice point and $\frac{\hat{\rho}_2}{\rho_2} = 1 - C$ in a similar way.

In fluid dynamics, the rate of mass entering a steady state system should be equal to the rate at which the mass leaves the system. Therefore, the continuity equation, for a transient system including the rate of change of mass within the cell, can be stated as,

$$\frac{\partial \hat{\rho}_i}{\partial t} + \nabla \cdot (\hat{\rho}_i \mathbf{u}_i) = 0 \quad (i = 1, 2), \quad (3.7)$$

where \mathbf{u}_i represent the i -th component of the local velocity . Besides, the volume diffusive flow rate \mathbf{j}_i of component i can be represented with the local velocity \mathbf{u} as,

$$\rho_i \mathbf{j}_i = \hat{\rho}_i (\mathbf{u}_i - \mathbf{u}). \quad (3.8)$$

Substituting $\hat{\rho}_i$ from equation (3.8) into equation (3.7) and incorporating the definition of composition $C = \frac{\hat{\rho}_1}{\rho_1} = 1 - \frac{\hat{\rho}_2}{\rho_2}$ gives:

$$\frac{\partial C}{\partial t} + \nabla \cdot (\mathbf{u}C) = -\nabla \cdot \mathbf{j}_1, \quad (3.9)$$

$$\frac{\partial (1-C)}{\partial t} + \nabla \cdot (\mathbf{u}(1 - C)) = -\nabla \cdot \mathbf{j}_2. \quad (3.10)$$

For LBM at low Mach number, the diffusive flow rate of two different fluids in the same point can be approximately assumed as $\mathbf{j}_1 = -\mathbf{j}_2 = \mathbf{j}$ (Ding et al, 2007; Lee, 2009), which yields:

$$\nabla \cdot \mathbf{u} = 0. \quad (3.11)$$

In Cahn-Hilliard equation, the diffusive rate is assumed to be proportional to the gradient of the chemical potential μ (Capuani et al, 2004) as:

$$\mathbf{j} = -M\nabla\mu, \quad (3.12)$$

where M is the mobility. Therefore, the equation (3.9) and equation (3.10) can be rewritten as,

$$\frac{\partial C}{\partial t} + \nabla \cdot (\mathbf{u}C) = \nabla \cdot (M\nabla\mu). \quad (3.13)$$

In present study, only the constant mobility M is considered in the LB model and the chemical potential μ is defined in section 2.4.2.

The equation (3.13) provides an evolution equation for the component C in LB model which indicates the binary fluids movement in Lee's LB model and contributes to dissipate the parasite currents in the numerical computation. (Lee, 2009)

3.1.3 Lattice Boltzmann Equations in Lee's model

As shown in equation (2.13), the intermolecular force and gravity $\mathbf{F}+\mathbf{G}$ in Lee's model comprises of (Connington and Lee, 2015):

$$\mathbf{F} + \mathbf{G} = \nabla\rho c_s^2 - \nabla p_0 - C\nabla\mu - \rho g\nabla h, \quad (3.14)$$

where ρc_s^2 is the ideal gas contribution to the pressure, p is the dynamic pressure enforcing the incompressibility and $\mu\nabla C$ represents the surface tension. In order to eliminate the parasitic currents incurred by the term $\nabla\rho$, based on the Pseudo-Potential LBM proposed by He et al (1999), a new particle distributor function is defined as: (Lee and Lin, 2010)

$$g_i = f_i c_s^2 + (p - \rho c_s^2)\Gamma_i(\mathbf{0}), \quad (3.15)$$

where $\Gamma_i(\mathbf{0}) = \frac{f_i^{eq}(\mathbf{u}=\mathbf{0})}{\rho}$, $\Gamma_i(\mathbf{u}) = \frac{f_i^{eq}(\mathbf{u})}{\rho}$ and $i=0\sim 9$ is the direction of the particle distribution functions (illustrated in Figure 3-1).

Taking the total derivative $D_t = \partial_t + \mathbf{e}_i \cdot \nabla$ of the new distribution g gives:

$$\partial_t g_i + \mathbf{e}_i \cdot \nabla g_i = D_t f_i \cdot c_s^2 + D_t(p - \rho c_s^2) \cdot \Gamma_i(\mathbf{0}) = -\frac{1}{\lambda}(g_i - g_i^{eq}) + (\mathbf{e}_i - \mathbf{u})[\nabla \rho c_s^2 - (\nabla p + C \nabla \mu) - \rho g \nabla h] \Gamma_i(\mathbf{u}) + D_t p \Gamma_i(\mathbf{0}) - D_t \rho c_s^2 \Gamma_i(\mathbf{0}). \quad (3.16)$$

The last two terms on the right hand side of equation (3.16) can be expanded through the continuity equation as follows,

$$D_t p = \frac{\partial p}{\partial t} + \mathbf{e}_i \cdot \nabla p \approx \mathbf{e}_i \cdot \nabla p, \quad (3.17)$$

where $\frac{\partial p}{\partial t}$ is dropped because it's on the order of truncation error under the low frequency limit in the model and detailed derivation of the dropped term can be found in Filippova and Hanel's paper (2000). Besides, the dimensional analysis shows that the $\mathbf{e}_i \cdot \nabla p \sim O(Ma^2)$ and in low Mach number approximation the following two terms are also on the order of truncation error: (Lee and Lin, 2003; 2005a)

$$\mathbf{u} \cdot \nabla p \sim O(Ma^3), \quad (3.18)$$

$$(\mathbf{e}_i - \mathbf{u}) \cdot \nabla p \cdot (\Gamma_i(\mathbf{u}) - \Gamma_i(\mathbf{0})) \sim O(Ma^3). \quad (3.19)$$

Due to the mass conservation and equation (3.11),

$$\frac{\partial \rho}{\partial t} + \rho \nabla \cdot \mathbf{u} + \mathbf{u} \nabla \rho = 0. \quad (3.20)$$

According to equations (3.17) - (3.20), equation (3.16) can be simplified as,

$$\partial_t g_i + \mathbf{e}_i \cdot \nabla g_i = -\frac{1}{\lambda}(g_i - g_i^{eq}) + (\mathbf{e}_i - \mathbf{u})[\nabla \rho c_s^2 \cdot (\Gamma_i(\mathbf{u}) - \Gamma_i(\mathbf{0})) - (\rho g \nabla h + C \nabla \mu) \cdot \Gamma_i(\mathbf{u})]. \quad (3.21)$$

The particle distribution function h_i for the composition C is related to f_i by $h_i = (C/\rho)f_i$. Taking the total derivative $D_t = \partial_t + \mathbf{e}_i \cdot \nabla$ of the new distribution h gives:

$$\partial_t h_i + \mathbf{e}_i \cdot \nabla h_i = -\frac{1}{\lambda}(h_i - h_i^{eq}) + (\mathbf{e}_i - \mathbf{u}) \cdot \frac{C}{\rho c_s^2} \cdot (\nabla \rho c_s^2 - \nabla p_0 - C \nabla \mu - \rho g \nabla h) \Gamma_i(\mathbf{u}) + (\partial_t C + \mathbf{e}_i \cdot \nabla C) \cdot \Gamma_i(\mathbf{u}) - (\partial_t \rho + \mathbf{e}_i \cdot \nabla \rho) \cdot C \cdot \frac{\Gamma_i(\mathbf{u})}{\rho}. \quad (3.22)$$

Substitute equation (3.11), (3.13) and (3.20) into the last two terms and the equation (3.22) can be simplified as,

$$\partial_t h_i + \mathbf{e}_i \cdot \nabla h_i = -\frac{1}{\lambda} (h_i - h_i^{eq}) + (\mathbf{e}_i - \mathbf{u}) \cdot \left[\nabla C - \frac{c}{\rho c_s^2} \cdot (\nabla p_0 + C \nabla \mu + \rho g \nabla h) \right] \Gamma_i(\mathbf{u}) + M \nabla^2 \mu \Gamma_i(\mathbf{u}). \quad (3.23)$$

In order to discretize the left side of equation (3.21) and (3.23), the trapezoidal rule is applied along characteristics over time step Δt for the terms on the right hand side as

$$g_i(x, t) - g_i(x - \mathbf{e}_i \delta t, t - \delta t) = -\frac{(g_i - g_i^{eq})}{2\tau} \Big|_{(x - \mathbf{e}_i \delta t, t - \delta t)} - \frac{(g_i - g_i^{eq})}{2\tau} \Big|_{(x, t)} + \frac{\delta t}{2} (\mathbf{e}_i - \mathbf{u}) \cdot \left[\nabla \rho c_s^2 \cdot (\Gamma_i(\mathbf{u}) - \Gamma_i(\mathbf{0})) - (\rho g \nabla h + C \nabla \mu) \cdot \Gamma_i(\mathbf{u}) \right]_{(x - \mathbf{e}_i \delta t, t - \delta t)} + \frac{\delta t}{2} (\mathbf{e}_i - \mathbf{u}) \cdot \left[\nabla \rho c_s^2 \cdot (\Gamma_i(\mathbf{u}) - \Gamma_i(\mathbf{0})) - (\rho g \nabla h + C \nabla \mu) \cdot \Gamma_i(\mathbf{u}) \right]_{(x, t)}, \quad (3.24)$$

$$h_i(x, t) - h_i(x - \mathbf{e}_i \delta t, t - \delta t) = -\frac{(h_i - h_i^{eq})}{2\tau} \Big|_{(x - \mathbf{e}_i \delta t, t - \delta t)} - \frac{(h_i - h_i^{eq})}{2\tau} \Big|_{(x, t)} + \frac{\delta t}{2} (\mathbf{e}_i - \mathbf{u}) \cdot \left[\nabla C - \frac{c}{\rho c_s^2} \cdot (\nabla p_0 + C \nabla \mu + \rho g \nabla h) \right]_{(x - \mathbf{e}_i \delta t, t - \delta t)} + \frac{\delta t}{2} (\mathbf{e}_i - \mathbf{u}) \cdot \left[\nabla C - \frac{c}{\rho c_s^2} \cdot (\nabla p_0 + C \nabla \mu + \rho g \nabla h) \right]_{(x, t)} + \frac{\delta t}{2} M \nabla^2 \mu \Gamma_i(\mathbf{u}) \Big|_{(x, t)} + \frac{\delta t}{2} M \nabla^2 \mu \Gamma_i(\mathbf{u}) \Big|_{(x - \mathbf{e}_i \delta t, t - \delta t)}, \quad (3.25)$$

where the non-dimensional relaxation time $\tau = \lambda / \delta t$ is related to the kinematic viscosity by $\nu = \tau c_s^2 \delta t$. The above two equations can be recast in simpler forms as,

$$\bar{g}_i(x, t) = \bar{g}_i(x - \mathbf{e}_i \delta t, t - \delta t) - \frac{(\bar{g}_i - \bar{g}_i^{eq})}{\tau + 1/2} \Big|_{(x - \mathbf{e}_i \delta t, t - \delta t)} + \delta t (\mathbf{e}_i - \mathbf{u}) \cdot \left[\nabla \rho c_s^2 \cdot (\Gamma_i(\mathbf{u}) - \Gamma_i(\mathbf{0})) + (-\rho g \nabla h - C \nabla \mu) \cdot \Gamma_i(\mathbf{u}) \right]_{(x - \mathbf{e}_i \delta t, t - \delta t)}, \quad (3.26)$$

$$\bar{h}_i(x, t) = \bar{h}_i(x - \mathbf{e}_i \delta t, t - \delta t) - \frac{(\bar{h}_i - \bar{h}_i^{eq})}{2\tau} \Big|_{(x - \mathbf{e}_i \delta t, t - \delta t)} + \delta t (\mathbf{e}_i - \mathbf{u}) \cdot \left[\nabla C - \frac{c}{\rho c_s^2} \cdot (\nabla p_0 + C \nabla \mu + \rho g \nabla h) \right]_{(x - \mathbf{e}_i \delta t, t - \delta t)} + \frac{\delta t}{2} M \nabla^2 \mu \Gamma_i(\mathbf{u}) \Big|_{(x, t - \delta t)} + \frac{\delta t}{2} M \nabla^2 \mu \Gamma_i(\mathbf{u}) \Big|_{(x - \mathbf{e}_i \delta t, t - \delta t)}, \quad (3.27)$$

where the modified particle and equilibrium distribution functions are defined as,

$$\bar{g}_i = g_i + \frac{1}{2\tau} (g_i - g_i^{eq}) - \frac{\delta t}{2} (\mathbf{e}_i - \mathbf{u}) \cdot \left[\nabla \rho c_s^2 \cdot (\Gamma_i(\mathbf{u}) - \Gamma_i(\mathbf{0})) + (-\rho g \nabla h - C \nabla \mu) \cdot \Gamma_i(\mathbf{u}) \right], \quad (3.28)$$

$$\bar{g}_i^{eq} = g_i^{eq} - \frac{\delta t}{2} (\mathbf{e}_i - \mathbf{u}) \cdot \left[\nabla \rho c_s^2 \cdot (\Gamma_i(\mathbf{u}) - \Gamma_i(\mathbf{0})) - (C \nabla \mu + \rho g \nabla h) \cdot \Gamma_i(\mathbf{u}) \right], \quad (3.29)$$

$$\bar{h}_i = h_i + \frac{1}{2\tau} (h_i - h_i^{eq}) - \frac{\delta t}{2} (\mathbf{e}_i - \mathbf{u}) \cdot \left[\nabla C - \frac{C}{\rho c_s^2} \cdot (\nabla p_0 + C \nabla \mu + \rho g \nabla h) \right] \Gamma_i(\mathbf{u}), \quad (3.30)$$

$$\bar{h}_i^{eq} = h_i^{eq} - \frac{\delta t}{2} (\mathbf{e}_i - \mathbf{u}) \cdot \left[\nabla C - \frac{C}{\rho c_s^2} \cdot (\nabla p_0 + C \nabla \mu + \rho g \nabla h) \right] \Gamma_i(\mathbf{u}). \quad (3.31)$$

It should be noticed that in order to avoid the implicit calculation in C , the term $M \nabla^2 \mu \Gamma_i(\mathbf{u})|_{(x,t)}$ is approximated by $M \nabla^2 \mu \Gamma_i(\mathbf{u})|_{(x,t-\delta t)}$ in equation (3.27). The composition, dynamic pressure and momentum can be computed by taking the zeroth and first moments of the modified particle distribution functions:

$$C = \sum_i \bar{h}_i, \quad (3.32)$$

$$\rho \mathbf{u} = \frac{1}{c_s^2} \sum_i \mathbf{e}_i \bar{g}_i - \frac{\delta t}{2} (C \nabla \mu + \rho g \nabla h), \quad (3.33)$$

$$p_0 = \sum_i \bar{g}_i + \frac{\delta t}{2} \mathbf{u} \cdot \nabla \rho c_s^2. \quad (3.34)$$

The dimensionless relaxation time is taken as an inverse function of the composition:

$$\frac{1}{\tau} = \frac{C}{\tau_1} + \frac{1-C}{\tau_2}. \quad (3.35)$$

In the computation, the gradients and Laplacians of macroscopic variable will be calculated with a combination of central and biased difference method and detailed description about it can be found in the Appendix B .

3.2 Fluid-Solid interaction models

As mentioned in section 2.5, the interaction model between the multiphase fluids and the solid boundary in LB model can be divided into two parts: the boundary model which can simulate the dynamic wetting phenomenon and the extrapolation model to obtain the values of LB nodes inside the curved boundary.

Therefore, in this section, the free energy wall boundary condition proposed by Lee is presented in section 3.2.1 to provide an effect way for the computational code in this thesis to simulate the wetting dynamic phenomenon. Then in section 3.2.2, the Ghost

Fluid Immersed Boundary Condition with a modification by us is illustrated to get the value with high accuracy in the code in this thesis.

3.2.1 Wall boundary condition

As mentioned in equation (2.14), the wall free energy is required in the simulation of the dynamic wetting phenomenon. In order to solve the equation (3.9) and (3.12) while considering the newly introduced energy, two boundary conditions should be applied in the fluid nodes on the wall. To ensure no mass flux normal to a boundary incurred by the chemical potential gradient, the condition $\mathbf{n} \cdot \nabla \mu|_{wall} = 0$ (\mathbf{n} is the unit normal vector) is required for the fluid nodes on the wall boundary. Besides, in order to minimize the free energy on the wall, neglecting the terms higher than the fourth-order in the second integrand in equation (2.14), a boundary condition in equilibrium state is applied as follows: (Connington and Lee, 2013)

$$\mathbf{n} \cdot \nabla C|_{wall} = -\frac{\phi_C}{\kappa} (C_{wall} - C_{wall}^2), \quad (3.36)$$

here the parameters in equation (2.14) is recommended by Liu and Lee (2009) as:

$\varphi_0 = \varphi_1 = 0$, $\varphi_2 = 1/2\phi_C$ and $\varphi_3 = 1/3\phi_C$ and $\phi_C = -\cos \theta^{eq}$ where θ^{eq} is the equilibrium contact angle.

For the unknown particle distribution functions, the bounce back scheme will be used to obtain their values, in which the out-going particle distribution g_i and h_i reflects back at the wall boundary and continues streaming as if they are continuations of g_i and h_i in the opposite direction as shown in Figure 3-2.

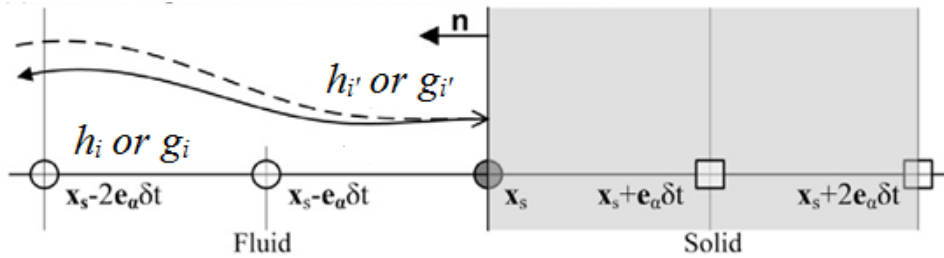


Figure 3-2 A schematic illustration of the bounce-back scheme (Lee and Liu, 2010)

For the first and second derivatives of macroscopic variables, as mentioned in section 2.5.1, the mirror scheme will be applied as illustrated in Figure 2-, any unknown

variable Φ outside the fluid domain is approximated with the corresponding mirroring points as:

$$\begin{cases} \phi(x_s + e_\alpha \delta t) = \phi(x_s - e_\alpha \delta t) \\ \phi(x_s + 2e_\alpha \delta t) = \phi(x_s - 2e_\alpha \delta t) \end{cases} \quad (3.37)$$

Besides, in Lee's model, a new boundary condition called equilibrium boundary condition is used to simulate the molecular movement near the wall boundary. The boundary condition is based on the assumption that impinging molecules reach equilibrium with the wall boundary or the surface. In fact, if the surface is rough on the characteristic length scale of molecules in reality, the reflection of molecules will be diffuse, which means molecules will "forget the past" and reemit after the wall collision with the equilibrium distribution function (Lee and Lin, 2005b).

3.2.2 Ghost Fluid Immersed Boundary Method

In the GF-IBM, the hydrodynamic boundary conditions are imposed into the model with the ghost points and the corresponding image points (shown in Figure 3-3).

(Tiwari and Vanka, 2012)

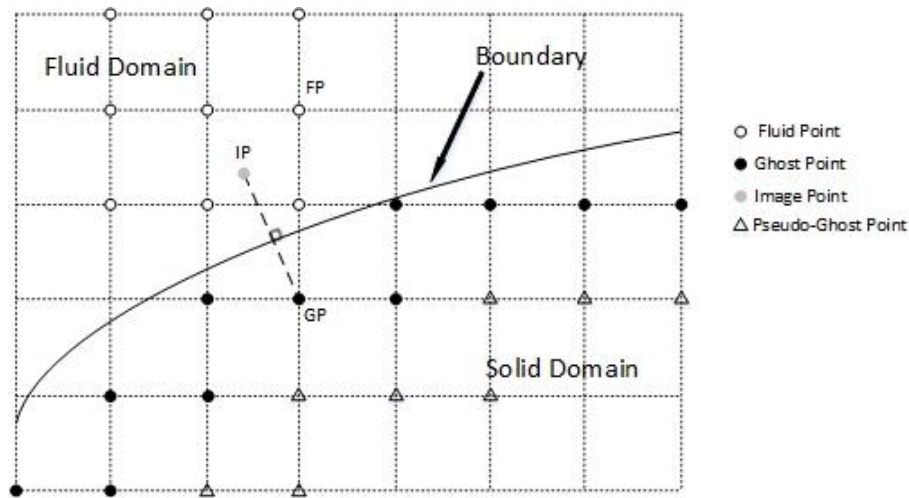
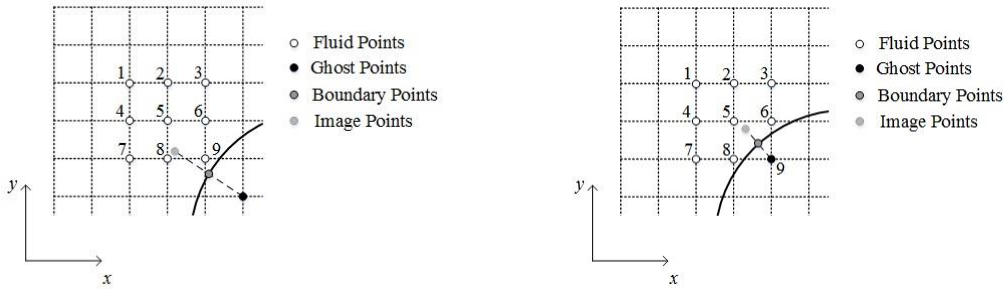


Figure 3-3 the schematic diagram about Ghost Points

In the Ghost Fluid Immersed Boundary Method (GFIBM), the variable values ϕ (such as density, velocity, composition, pressure and chemical potential) of the ghost points can be determined from the values of corresponding image points and the hydrodynamic boundary conditions. In this thesis, the biquadratic interpolation scheme is used to find the values ϕ at the image point and the detailed procedure of the GF-IBM used in this paper is as follows:

(1) The identification of the ghost points (GP) and their corresponding image points (IP) in the model.



(a) All nine nodes are fluid nodes (b) Eight nodes are fluid nodes and one is ghost node

Figure 3-4 Interpolation for image point value

(2) The bi-quadratic interpolation scheme (equation (3.38)) is used to find the values at the image points, since generally the image points do not coincide with the lattice fluid nodes in the model.

$$\varphi = ax^2y^2 + bxy^2 + cx^2y + dx^2 + ey^2 + fxy + gx + hy + k \quad (3.38)$$

Here a, b, c, d, e, f, g, h and k are constants determined by the value of nine surrounding fluid points, x and y are the coordinate values of nine fluid points around the image point (shown in Figure 3-4 (a)). However, in a more general case, not all the nine points of the square is inside the fluid domain. As an example, Figure 3-4 (b) shows a case in which eight nodes are fluid nodes and one is ghost node. In such a case, a more general approach for interpolation is employed:

(a) For velocity computation, whenever the point is inside the boundary, it is replaced with its corresponding boundary points and the values on the left hand side of equation (3.38) should be same as the boundary velocity.

(b) For computation of the other variables (i.e. density, composition, chemical potential, dynamic pressure), the zero normal gradient condition is imposed for its corresponding boundary points in the interpolation equations as

$$\frac{\partial \varphi_b}{\partial n} = a(2x_b y_b^2 n_x + 2x_b^2 y_b n_y) + b(y_b^2 n_x + 2x_b y_b n_y) + c(x_b^2 n_y + 2x_b y_b n_x) + d \cdot 2x_b n_x + e \cdot 2y_b n_y + f(x_b n_y + y_b n_x) + g n_x + h n_y = 0 \quad (3.39)$$

Here the subscript b denotes the boundary points and the n_x and n_y denote the gradient of the normal unit vector.

(3) The scalar variables at the ghost points are obtained via extrapolation along the normal direction with equation (3.40), so that the appropriate hydrodynamic boundary conditions at the Dirichlet and Neumann boundary conditions can be satisfied.

$$\frac{\partial \varphi_b}{\partial n} = \frac{\varphi_{IP} - \varphi_{GP}}{\Delta l} + O(\Delta l^2) \quad (3.40)$$

Here φ_{IP} and φ_{GP} represent the variables at image points and ghost points, respectively.

For the velocity extrapolation, unlike the centrosymmetric scheme with the BP as the centre used in other GF-IBMs, the axial symmetric scheme with the tangent line through the BP (Figure 3-5) is employed in this paper. Under the local coordinate system, the image point velocity is transformed along and normal to the tangent line through BP (shown in Figure 3-5). Then the ghost point velocity can be obtained as $(u_x', -u_y')$ under a local coordinate system since the solid boundaries are stagnant in the simulation in the next section.

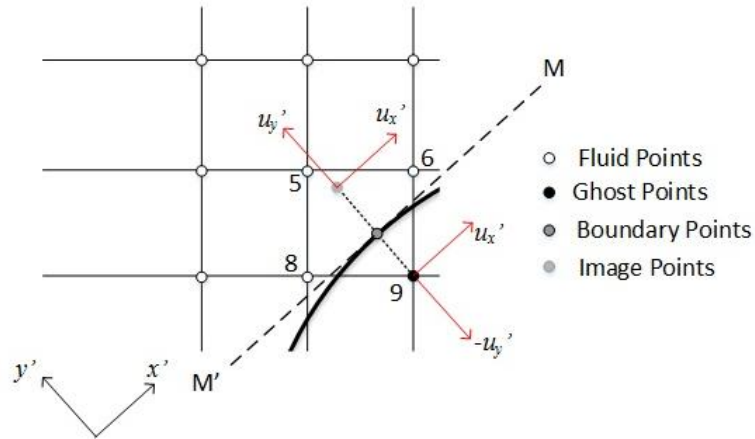


Figure 3-5 the axial symmetric scheme figure of the velocity extrapolation

(4) Finally, the equilibrium distribution functions for \bar{g}_i^{eq} and \bar{h}_i^{eq} can be calculated with the variables in the global coordinate system. In this thesis, the equilibrium distribution assumption is applied for the solid boundaries and the non-equilibrium part of the distribution functions is ignored at the ghost points. Once the distribution functions at the ghost points are known, the streaming step can be carried out in the simulation after the collision steps.

Chapter 4 Validation and Verification

In this chapter, in Section 4.1, the stationary droplets at a large density ratio (1000:1) are first examined for the accuracy of the LB model used in our code. Since the surface tension is given as a parameter for the code, the numerical result should satisfy the analytical solutions at an equilibrium. Then, in the next section, Section 4.2, the capillary rise rate in a long, narrow tube is studied only under the effect of gravity and surface tension for fluids with different viscosities. The capillary rise rate theories are also introduced to validate the LB model's ability to simulate simple dynamic behaviours of multiphase systems and the accuracy of the GF-IBM method on the simple, long linear boundary. In Section 4.3 and Section 4.4, the interaction of fluid interfaces with the stationary circular solid particles is studied. Since the particles can deform an interface locally and alter the capillary interaction behaviour dramatically, in these two sections, the capillary bridge and capillary rise between two horizontal circular bodies are simulated to verify the accuracy of capillary interaction force and liquid distribution of the numerical results. In Section 4.5, a capillary rise in porous media is simulated and the pressure distribution curve is studied to validate its ability to simulate the multiphase flow in complex porous media.

In order to simplify the numerical simulation, dimensionless quantities are used in the numerical simulation, which means that the lattice length, time step and the densities are regarded as unity in the simulation. Therefore, the velocity, pressure and force in the model are also dimensionless quantities. The conversion relationship between the LBM unit and the real physical unit can be found in Appendix A

4.1 Droplet test at large density ratio

As mentioned in Section 2.4.1, the near-interface parasitic currents are always reported in the previous LB multiphase model and incur large pressure oscillation near the interface, which would restrict the two-phase flow with a small density ratio (Lee and Lin, 2005). Because the code (the multiphase LB part in *FPS-BHAM*) used in this chapter was mainly developed by us with the papers published by Lee and his

co-workers, the accuracy of our code to simulate the two-phase fluid model without complicated a solid boundary condition should be first validated.

As a result, in this section, a stationary droplet is located at the centre of the computational domain and the pressure difference across the interface is calculated when the system reaches an equilibrium. The numerical results are compared with the analytical solutions to verify the accuracy of the code.

4.1.1 Young–Laplace equation and pressure expression in the LB model

The Young–Laplace (Y–L) equation is a non-linear partial equation describing the capillary pressure difference across the interface between two static fluids (i.e. liquid and vapour) caused by the surface tension (Oertel et al., 2010). For two-dimensional problems, the Y–L equation can be expressed as (Lee, 2004):

$$\Delta p = \frac{\sigma}{R}, \quad (4.1)$$

where Δp is the pressure difference across the interface, σ is the surface tension, and R is the radius of the droplet. With the surface tension and droplet radius, the analytical solution of pressure difference can be obtained before the simulation.

For the LB model used in this thesis, equation (3.14) used in the distribution computation only indicates the pressure difference between adjacent LB nodes, and the total pressure should be the summation of the pressure difference (Daniele, 2009). Therefore, by summing the hydrodynamic and hydrostatic pressure p_1 , the thermodynamic pressure p_0 and the pressure incurred by the surface tension, the total pressure P in the LB model can be expressed as (Daniele, 2009; Amaya-Bower and Lee, 2011):

$$P = p_0 + p_1 - \kappa C \nabla^2 C + \frac{1}{2} \kappa |\nabla C|^2, \quad (4.2)$$

where the thermodynamic pressure can be expressed as:

$$p_0 = C \frac{\partial E_0}{\partial C} - E_0, \quad (4.3)$$

$$E_0 = \beta C^2 (C - 1)^2, \quad (4.4)$$

where E_0 is the bulk energy to provide a free-energy barrier between the pure states $C=0$ and $C=1$ (Daniele et al., 2009). The main contribution to total pressure is given by the hydrodynamic and static pressure p_1 and the other two provide a settle effect on the computation (Amaya-Bower and Lee, 2011).

4.1.2 Numerical simulation results

To test the accuracy of the LB model, a stationary droplet with radius $R=30$ is located at the centre of a computational domain of 120×120 with no gravity effect. The initial density inside the droplet is 1.0 and outside is 0.001. In order to avoid the sharp density jump across the interface in the simulation on the early stage of the simulation, density distribution equation (4.5) is utilised to initialise the density distribution in the whole domain in the whole thesis (Lee and Lin, 2005a):

$$\rho = \frac{\rho_1 + \rho_2}{2} + \frac{\rho_1 - \rho_2}{2} \tanh \frac{2z}{S}, \quad (4.5)$$

where z is the distance to the interface, S is the interface thickness, and \tanh is the hyperbolic tangent function. To the best knowledge of the author, the initial condition of the model, especially the density distribution, is critical for the computational stability in the early stage. With a sharp density jump across the interface, the interface would be easily distorted at the first several hundred steps.

The surface tension $\sigma=7.275 \times 10^{-4}$, the interface thickness $S=5$, and the other parameters related to the two kinds of fluids can be referred to in Table 4-1.

Table 4-1 Parameters of two different phases in the droplet test (in LB units)

Variable	Phase 1	Phase 2
Density	1.0	0.001
Composition	1.0	0.0
Kinetic viscosity	0.01	0.157

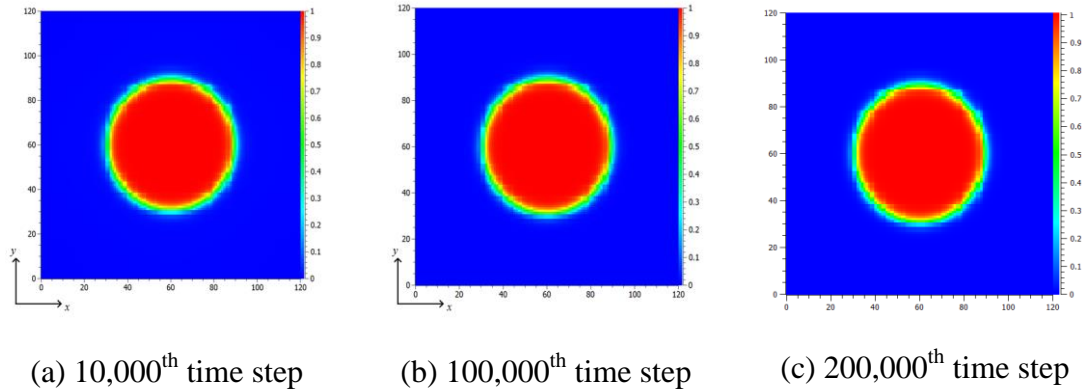


Figure 4-1 Component contour of the droplet in the first 200,000 time steps

After 50,000 time steps, the system reaches an equilibrium (the location of the interface between two different fluids is stable) and the component contour of the droplet in the 10,000th, 100,000th and 200,000th time steps is plotted in Figure 4-1. In Figure 4-2, the component distribution versus the distance from the centre of the droplet in the 200,000th time step (illustrated in Figure 4-1(c)) is displayed.

The droplet boundary indicated by the dashed line in Figure 4-2 shows little shrinkage, about 1.3%, compared with the initial value in the simulation and the radius decreases to about 29.6 in the 200,000th step.

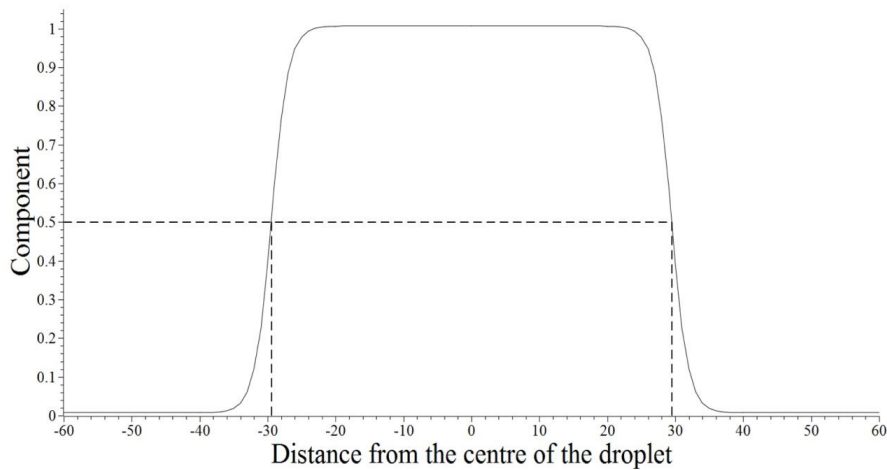


Figure 4-2 Component distribution versus the distance from the centre of the droplet in the 20,000th step

In addition, the pressure difference across the interface in the first 200,000 time steps is presented in Figure 4-3. It shows that the pressure difference oscillates in the first 40,000 time steps and becomes stable after that. The oscillation might be caused by

the hydrodynamic and hydrostatic pressure p_1 initialisation in the model, which is assumed to be zero at the beginning and completely different in reality.

According to equation (4.1), the analytical pressure difference across the interface should be 2.425×10^{-5} while the stable pressure difference value at 200,000 time steps obtained from Figure 4-3 is 2.455×10^{-5} , with a relative error $(|\Delta p_{analytical} - \Delta p_{numerical}| / |\Delta p_{analytical}|)$ equalling 1.2%. The results show that the LB model used in this thesis agrees with the Y-L equation and the model can be regarded as stable in the droplet test.

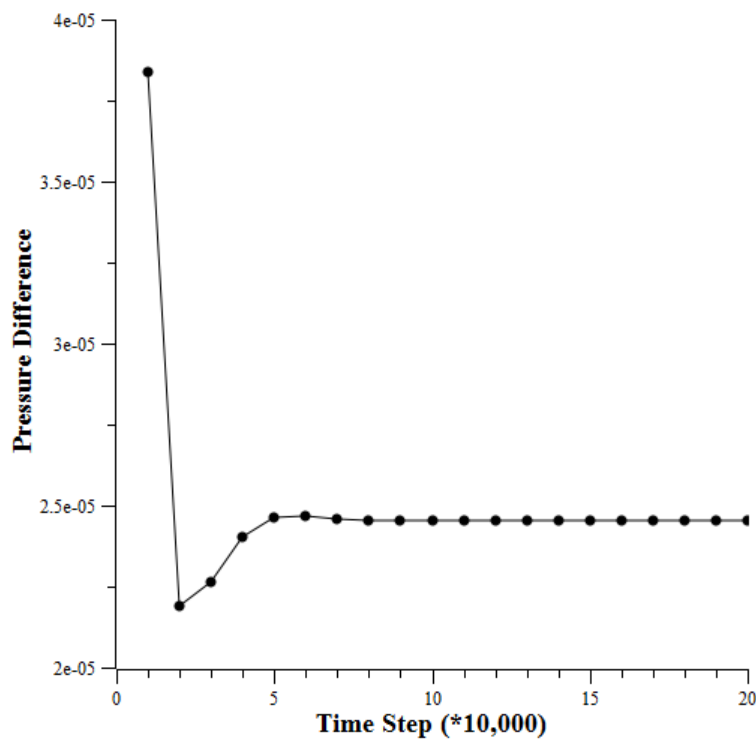


Figure 4-3 Pressure difference across the interface of droplets in the first 20,000 steps

4.2 Capillary tube

The capillary-driven flow is an important phenomenon in science, industry, agriculture as well as daily life and it is also a good case in which to test the LBM model because of the simply straight fixed boundaries in the simulation. In this section, the capillary rise rate between two paralleled plates is first analysed and then the numerical simulation results are compared with the analytical solutions for fluid with different viscosities.

4.2.1 Theory of capillary rise in a vertical tube

In a capillary tube, the surface tension draws liquid up/down until the liquid inside the tube is balanced by the pressure difference induced by the gravity. For a three-dimensional (3D) problem, the moment equation for a rising/dropping liquid can be presented as follows (Fries and Dreyer, 2008):

$$\frac{2\sigma\cos\theta}{R} = \rho gh + \frac{8\mu h}{R^2} \dot{h} + \rho \frac{d(h\dot{h})}{dt}, \quad (4.6)$$

where σ is the surface tension, θ is the contact angle, R is the inner tube radius, h is the height of the capillary rise, \dot{h} is the $\frac{dh}{dt}$, ρ is the fluid density, g is the gravity, and μ is the dynamic viscosity of the liquid.

On the right-hand side of equation (4.6), the individual terms can be referred to as (from left to right): the gravity pressure (hydrostatic pressure), the viscous pressure loss, following the Hagen–Poiseuille law (Oertel et al., 2010), and pressures caused by the inertia term.

Meanwhile, for the two-dimensional (2D) problem simulated in this thesis, according to the Hagen–Poiseuille law, the viscous pressure loss in equation (4.6) should be modified as $\frac{6\mu h}{R^2} \dot{h}$ and the expression of the capillary pressure on the right-hand side of equation (4.6) should be presented as $\frac{\sigma\cos\theta}{R}$.

Neglecting the inertia term in equation (4.6), Zhmud et al. (2000) proposed a long-term asymptotic relationship between h and t as follows:

$$h(t) = \frac{a}{b} \left(1 - e^{-\frac{b^2 t}{a}} \right), \quad (4.7)$$

where $a = \frac{\sigma R \cos\theta}{4\mu}$ and $b = \frac{\rho g R^2}{8\mu}$ for the 3D problem (Fries and Dreyer, 2008) and $a = \frac{\sigma R \cos\theta}{6\mu}$ and $b = \frac{\rho g R^2}{6\mu}$ for the 2D problem.

By involving the Lambert W function $W(x)$, Fries and Dreyer (2008) rearranged equation (4.6) without the inertia terms as follows:

$$h(t) = \frac{a}{b} \left(1 + W \left(-e^{-1 - \frac{b^2 t}{a}} \right) \right). \quad (4.8)$$

The final stable capillary rises ($t \rightarrow +\infty$) for both equation (4.7) and equation (4.8) are $\frac{a}{b} = \frac{2\sigma \cos \theta}{\rho g R}$ and the viscosity only has an influence on the capillary rise rate in these models.

4.2.2 Numerical simulation details

To validate the accuracy of the LB model in simulation of the capillary rise rate problem, three capillary rise models with the same contact angles ($\theta=120^\circ$) are simulated in this section. As illustrated in Figure 4-4, the computational domain is 120×120 with solid boundaries (contact angle equals 90°) located around the domain. The two parallel plates are symmetrical with respect to the axis $x=61$ in the domain, with 100 lattice units tall starting at $y=10$ and a separation distance $2R=23.6$ (shown in Figure 4-4). In this section, the GF-IBM method is applied on the inner sides of the plates and due to the simple linear shape of the boundary, the bi-quadratic extrapolation in the GF-IBM model mentioned in Section 3.2.2 can be degenerated to the quadratic extrapolation as follows:

$$\varphi_i = ax_i^2 + bx_i + c. \quad (4.9)$$

The original liquid level is at $y=60$ and the height difference $h(t)$ between the two interfaces (illustrated in Figure 4-4) is defined as the capillary rise driven by the surface tension. In order to increase the accuracy of the measurement, the contact angle for the outer sides of plates is also 90° to ensure a flat interface outside the plates. The surface tension is 7.275×10^{-4} and the gravity is 9.8×10^{-7} . Other parameters for these three capillary rise cases can be found in Table 4-2.

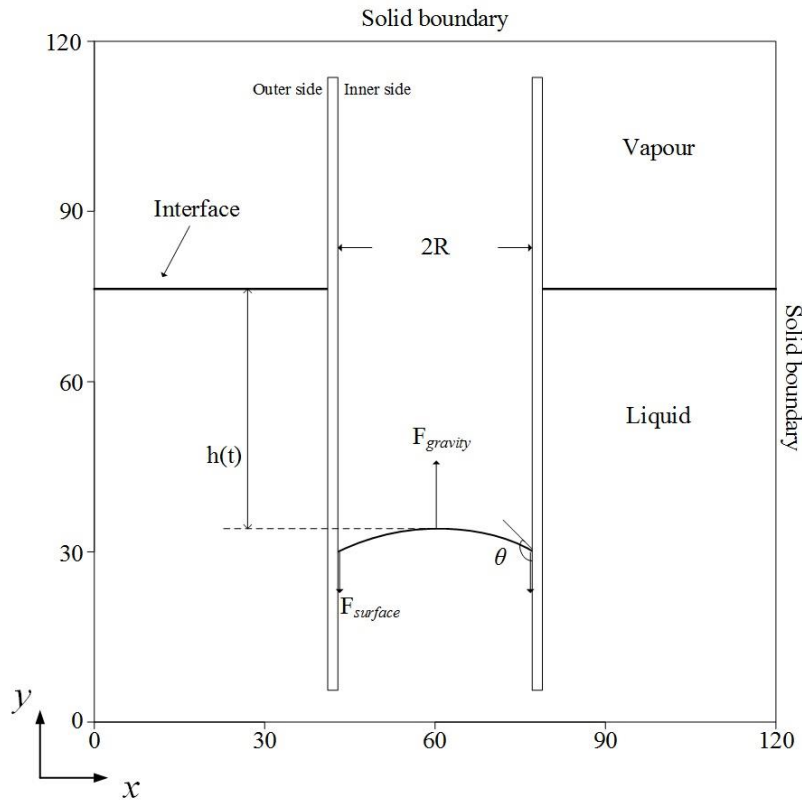


Figure 4-4 A schematic description of a two-dimensional capillary rise between two parallel plates (the contact angle is greater than 90°)

Table 4-2 Parameters used in six capillary models (in LBM units)

Variable	Case 1	Case 2	Case 3
Density (liquid)	1.0	1.0	1.0
Density (vapour)	0.001	0.001	0.001
Kinematic viscosity η_1 (Phase 1)	0.01	0.05	0.1
Kinematic viscosity η_2 (Phase 2)	0.157	0.157	0.157

According to equation (4.7) and equation (4.8), the analytical maximum capillary height for these three models should be -31.46 lattice units and with different kinetic viscosity of liquid, the capillary rise rates should be different (according to equation (4.7) and equation (4.8)) from each other.

4.2.3 Numerical simulation results

As the contact angle is greater than 90° , the liquid between two parallel plates falls down while the outside water level rises up as a result of mass conservation in the

system. After 1,000,000 time steps (about 110 hours of CPU time), all three cases are in the equilibrium state and the capillary rises are all nearly the same as each other.

Figure 4-5 shows the component contour of Case 1 before 1,000,000 time steps and Figure 4-6 shows the corresponding component distribution at axes $x=20$ and $x=60$ in Figure 4-5(d). From Figure 4-6, it can be found that at 1,000,000 time steps, the capillary rise (the distance between two curves at $C=0.5$ in Figure 4-6) is 31.0, which has an error of 1.46% ($|h_{analytical} - h_{numerical}|/|h_{analytical}|$) relative to the analytical solution.

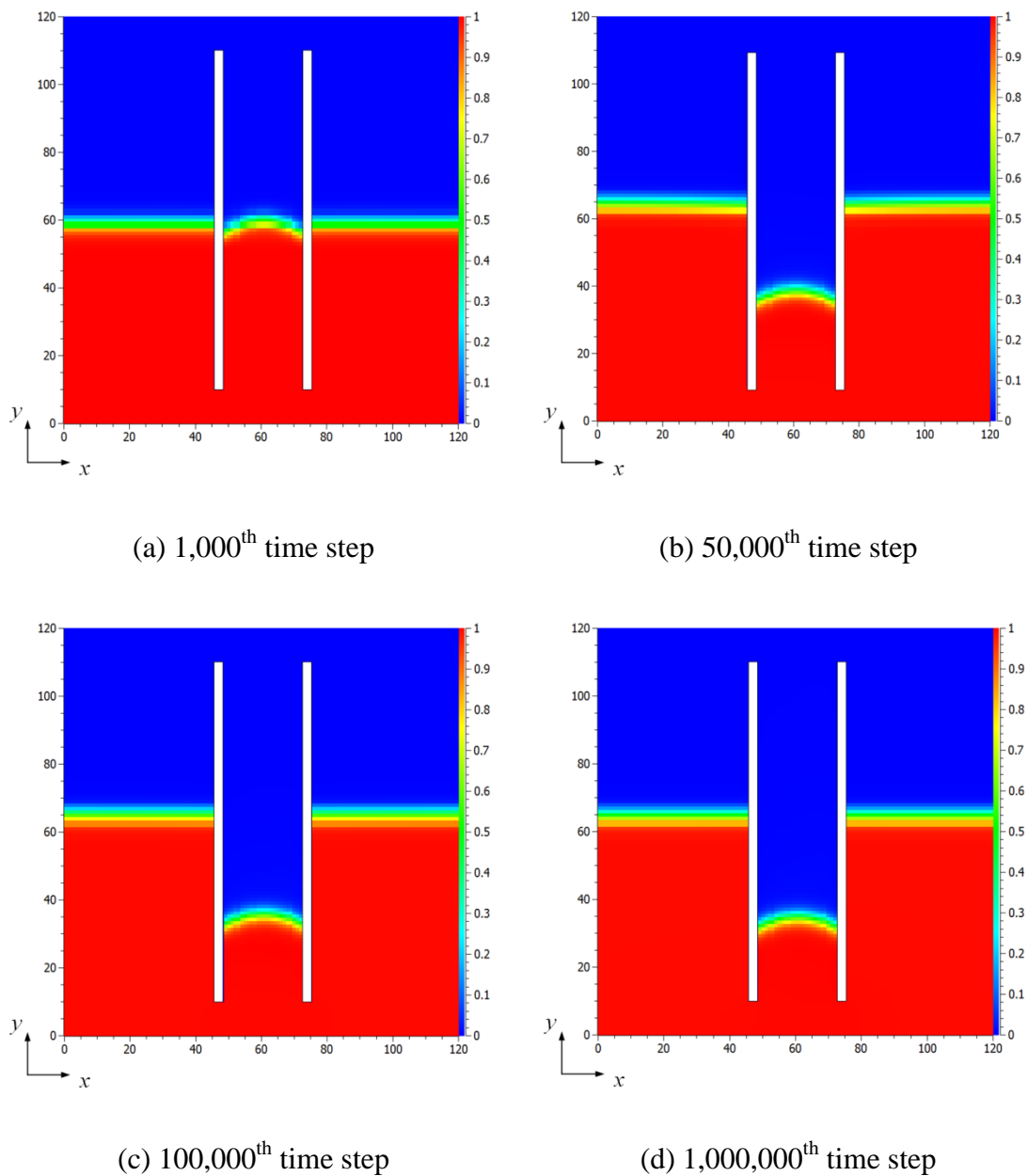


Figure 4-5 Component contour of Case 1 in the first 1,000,000 time steps

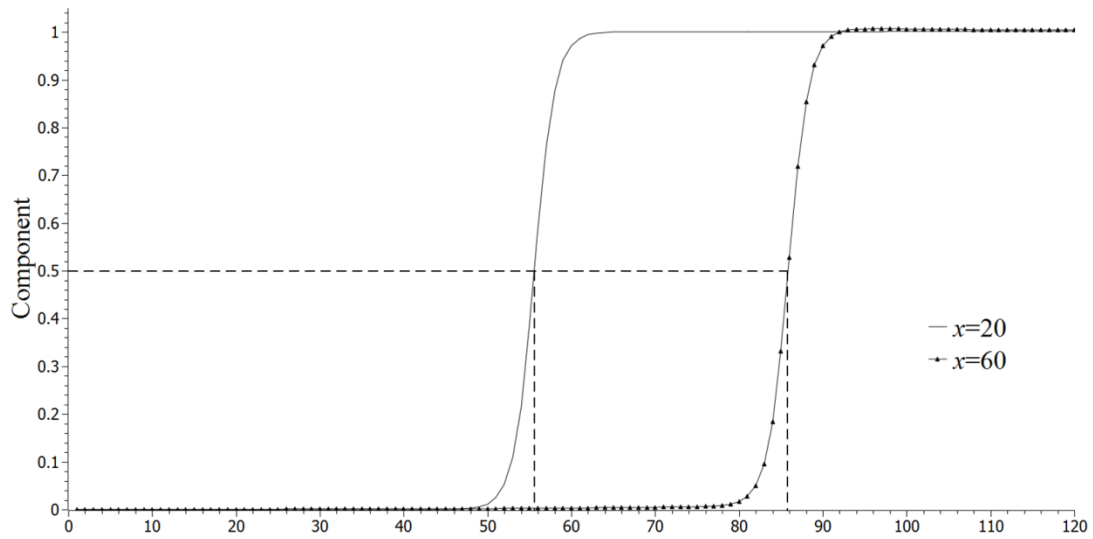


Figure 4-6 Component distribution of Case 1 in 1,000,000th time step

In Figure 4-7, the time evolutions of the capillary rise of these three cases are plotted. With larger kinematic viscosity η_1 , a longer time is needed for the system to reach the steady state (or the theoretical capillary descent). At about the 100,000th time step, the capillary rise $h(t)$ in Case 1 achieves the maximum value, while until about the 750,000th time step, the $h(t)$ in Case 3 reaches the theoretical capillary descent.

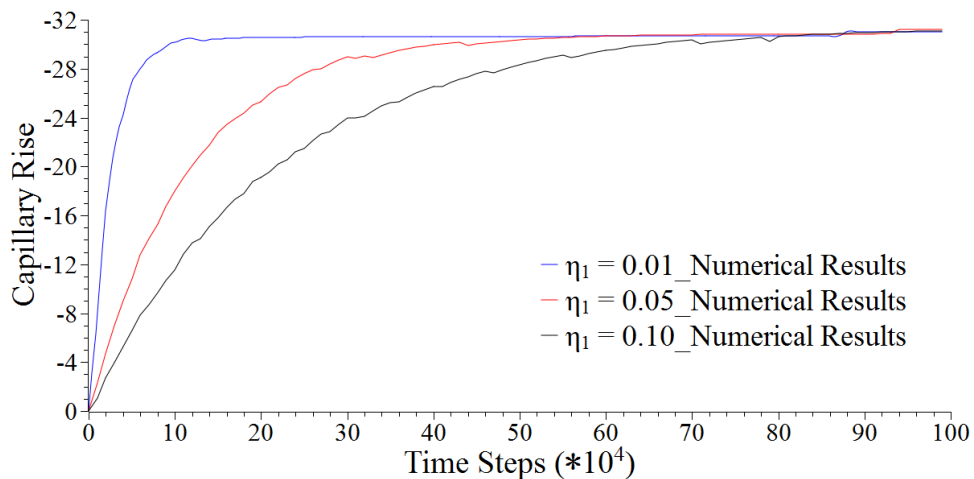


Figure 4-7 Time evolution of capillary rise $h(t)$

From Figure 4-8 to Figure 4-10, the time evolution of the capillary rise with different kinematic viscosities (η_1) is compared with the two analytical solutions with the corresponding η_1 . Equation (4.7) and equation (4.8) are labelled as Zhmud's

Equation and Fries' Equation in these three figures, respectively. The capillary rise rate shows good agreement with the theoretical ones when the kinematic viscosities $\eta_1=0.01$ (illustrated in Figure 4-8), while there are obvious contrasts between the analytical solutions and numerical ones in the other two cases (illustrated in Figure 4-9 and Figure 4-10). The obvious difference between the numerical results and the analytical ones, especially at high viscosities, might result from the initial contact angle assumption difference between the theoretical equations and the numerical models. As illustrated in Figure 4-5(a), Figure 4-11 and Figure 4-12, though the theoretical contact angles in these three cases are the same (120°), due to the initialisation of the numerical model, the initial contact angle between the liquid and the plates is 90° , rather than 120° , which might need some time steps to increase to the theoretical one. These three figures indicate that the lower the kinematic viscosity in the numerical system, the faster the contact angle will arrive at the set value. However, in equations (4.7) and (4.8), the contact angle is assumed to be constant at 120° in the study, which might lead to the disagreement between numerical results and the analytical solutions.

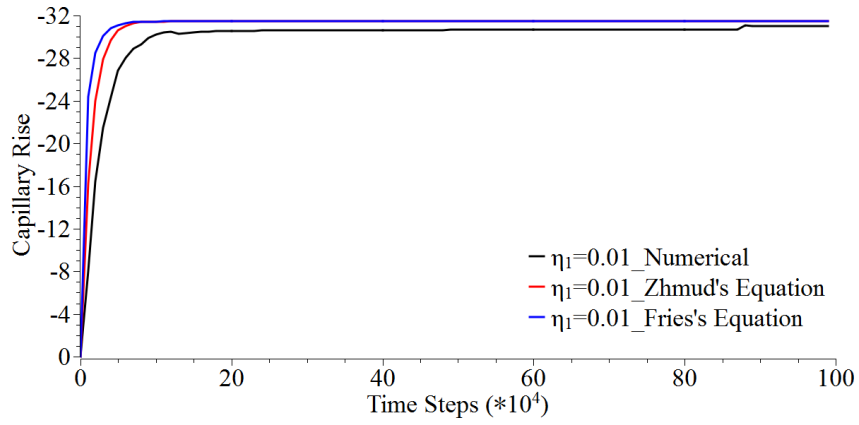


Figure 4-8 Numerical and analytical results for capillary rise (Case 1)

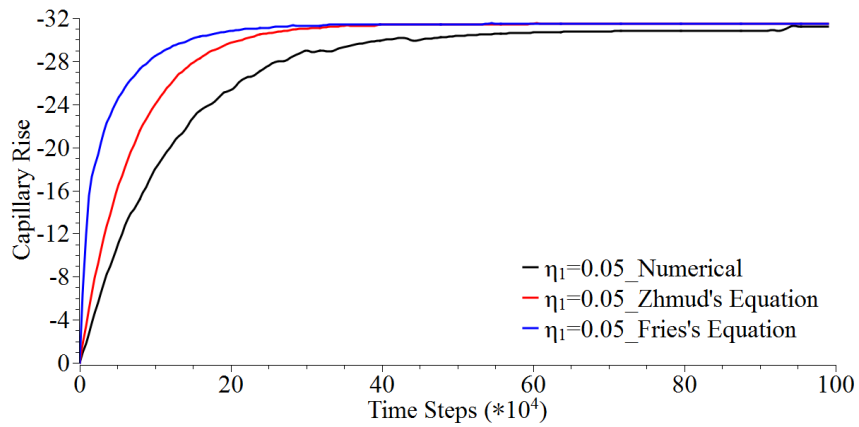


Figure 4-9 Numerical and analytical results for capillary rise (Case 2)

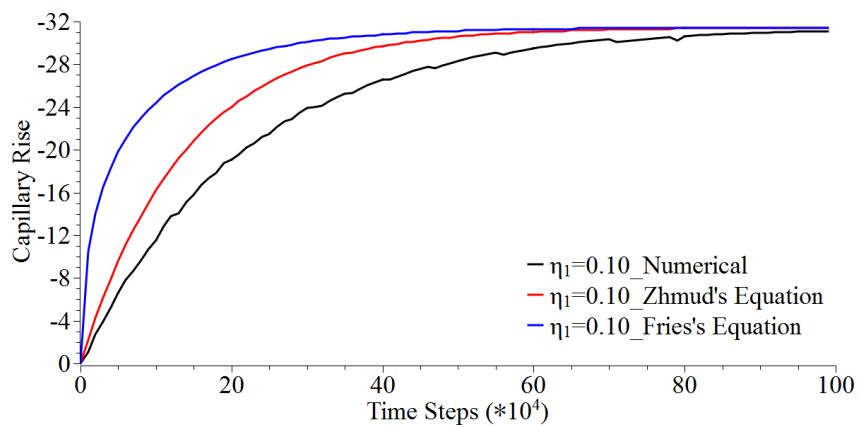


Figure 4-10 Numerical and analytical results for capillary rise (Case 3)

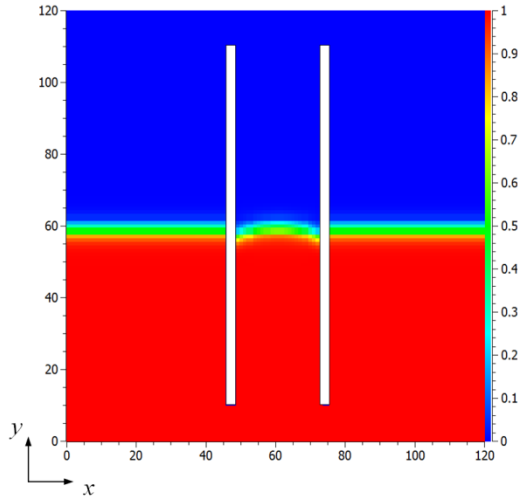


Figure 4-11 Component contour of Case 2 in the 1,000th time steps

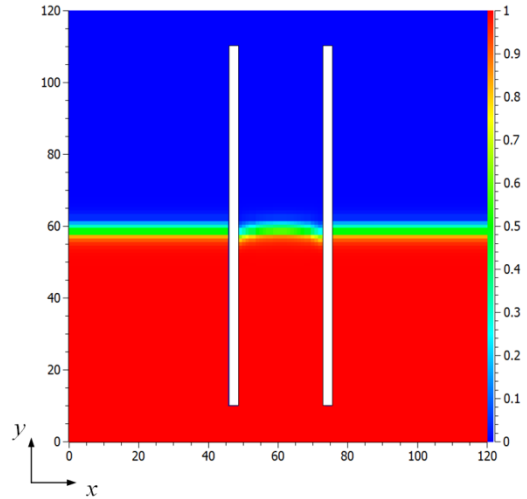


Figure 4-12 Component contour of Case 3 in the 1,000th time steps

Figure 4-13 displays the total pressure distribution along the axes $x=60$ and $x=20$ in Figure 4-5(d). Compared with Figure 4-5(d), it can be found that the turning points of the pressure distribution lines are near the interface point on these two axes, which conforms to the reality that the interface of two different fluids is always the turning point of pressure distribution.

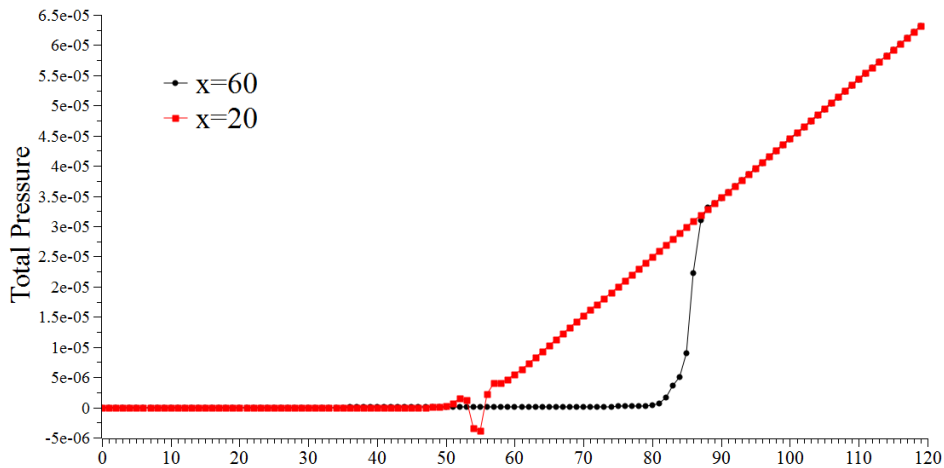


Figure 4-13 Total pressure distribution along two axes

In Figure 4-13, the two pressure distribution lines coincide with each other near the interface point and develop with the same slope angle, which is 1.03×10^{-6} in value. Since the pressure is the same between and out of two paralleled plates under the meniscus ($y \approx 87$), the liquid in the system should be stagnant due to zero pressure

difference, which proves that the system reaches an equilibrium at that time. Besides, the slope value is similar with the theoretical pressure distribution slope $(\rho_1 - \rho_2)g = 0.999 * 9.8 \times 10^{-7} \doteq 9.79 \times 10^{-7}$ and the difference might be caused by the capillary pressure due to the surface tension in the model.

It should be mentioned that the clink on the total pressure curve at $x=20$ in Figure 4-13 might be caused by the discontinuity of the component and density across the interface. For the total pressure evolution at $x=60$, because the hydrodynamic/hydrostatic pressure p_1 has a large pressure jump (from near zero to the pressure value outside plates at the same liquid level) near the interface, the influence of component discontinuity is diminished and the pressure distribution curve is smoother than that at $x=20$.

As a result, the above results show that the LB model and the GF-IBM model have the ability of fluids dynamic simulation under the simple geometrical boundaries and are able to predict the corresponding pressure distribution accurately.

4.3 Capillary bridge between two circular bodies

The capillary bridge (illustrated in Figure 4-12) is recognised as an important phenomenon in many systems, including the consolidation of granules, wetting of the powders, and the capillary condensation. The capillary bridge force is contributed by the capillary pressure inside the liquid bodies and the surface tension acting on the meniscus (Kralchevsky and Nagayama, 2001).

In this section, the capillary bridge forces with different contact angles are calculated with a new method from the numerical results of the LB model. Then they are compared with the corresponding theoretical solutions to show the accuracy of the new forcing calculation method proposed in this section and the LB model.

4.3.1 Theory of capillary bridge between two circular bodies

In order to simplify the theoretical analysis, the shape of the meniscus in Figure 4-14 is always assumed to be an arc (Kralchevsky and Nagayama, 2001). Therefore, according to the Y–L equation, the capillary pressure across the middle cross-section MM' in Figure 4-14 can be presented as $-\sigma/r_1$. The bridge force between two particles consists of the force F_p caused by the capillary pressure and the force caused

by the surface tension. Then the total capillary force F at the cross-section MM' can be expressed as follows (Shinto et al., 2007):

$$F = -2\sigma + F_p = -2\sigma + 2l \cdot p, \quad (4.10)$$

where p is the capillary pressure and can be expressed as:

$$p = -\frac{\sigma}{r_1}. \quad (4.11)$$

The values of l and r_1 in Figure 4-14 can be determined by fitting the arc as follows:

$$y - y_0 = l + r_1 - [r_1^2 - (x - x_0)^2]^{1/2}, \quad (4.12)$$

where x_0 and y_0 are the midpoint of the central axes of two circular bodies.

In fact, it can be easily proven that the total capillary force is independent of the choice of the cross-section (Kralchevsky and Nagayama, 2001). In other words, the force acted on the cross-section MM' should be the same as the force acted on each of the circular particles in the system. Therefore, the force acted on the left circular particle in Figure 4-14 is calculated and compared with the force in section MM' in this section.

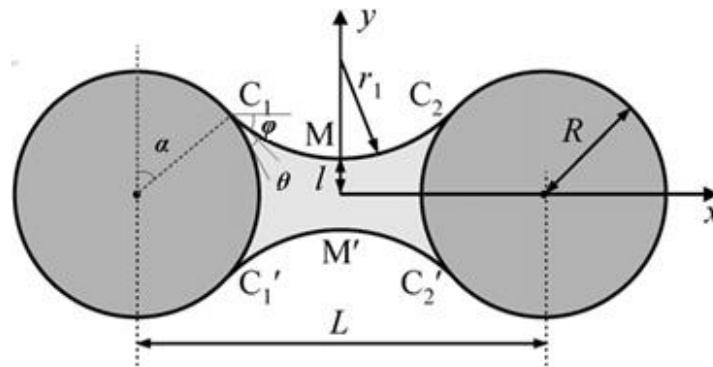


Figure 4-14 Sketch of a capillary bridge between two cylinders. θ is the contact angle and ϕ is the slope angle (Shinto et al., 2007)

4.3.2 Numerical simulation details and the force calculation method

The simulation domain for the capillary bridge test is 240×120 and two circular bodies with the same radius $R=30.79$ are symmetrical with respect to the axis $x=0$ (illustrated in Figure 4-14). The circular centres of these two bodies are $(-37.5,0.0)$

and (37.5,0.0), respectively. A droplet with a radius equalling 15.0, density equalling 1.0, and kinematic equalling 0.1 is initialised in the midpoint of the two circle centres with three different contact angles (30°, 60° and 90°) with the circular bodies and the same surface tension 7.275×10^{-5} .

In order to calculate the force F_p caused by the capillary pressure around the left circular body in Figure 4-14, a new forcing calculation method similar to the Ghost Fluid Immersed Boundary Method used in Section 3.2.2 is proposed as follows.

At first, the circular body is divided into N arcs with the same arc length l_p ($l_p = 2\pi R/N$). With the total pressure from the numerical results of the LB model, the pressure acted on the centre of each arc p_a can be interpolated from the pressure values on the fluid and ghost nodes around it (illustrated in Figure 4-15; for simplicity, the bilinear interpolation method is applied here). Then the force can be calculated as the summation of the force acted on every arc as follows:

$$\mathbf{F}_p = \sum_{a=1}^N p_a l_p \mathbf{n}, \quad (4.13)$$

where \mathbf{n} is the normal directional unit of the arc. Meanwhile, for the force \mathbf{F}_s incurred by the surface tension, the force point should be the same as the interface point on the circular surface where component $C=0.5$. Then the slope angle of the menisci θ in Figure 4-14 can be represented as:

$$\varphi = \alpha - \theta. \quad (4.14)$$

Then the total capillary force applied on the obstacles can be expressed as:

$$\mathbf{F} = \mathbf{F}_p + \mathbf{F}_s \cdot \mathbf{n}_\theta, \quad (4.15)$$

where $\mathbf{n}_\theta = (\cos\varphi, -\sin\varphi)$.

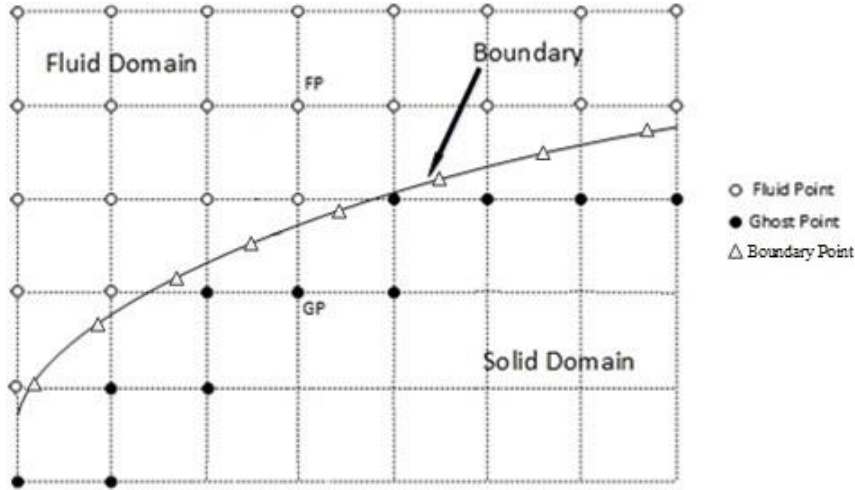


Figure 4-15 Schematic figure of the boundary points on a curved surface

It should be mentioned that the expression in (4.15) ignores the effect of shear stress acted on the circular bodies. According to the definition of shear stress for Newtonian fluids in laminar flow in this thesis, the shear stress should be proportional to the strain rate (or the rate of shear velocity) on the surface (Oertel et al., 2010) and can be expressed as:

$$\boldsymbol{\tau} = \mu \nabla \mathbf{u}, \quad (4.16)$$

where $\boldsymbol{\tau}$ is the shear stress, μ is dynamic viscosity (which equals $\rho \cdot \eta$), and $\nabla \mathbf{u}$ represents the rate of shear velocity.

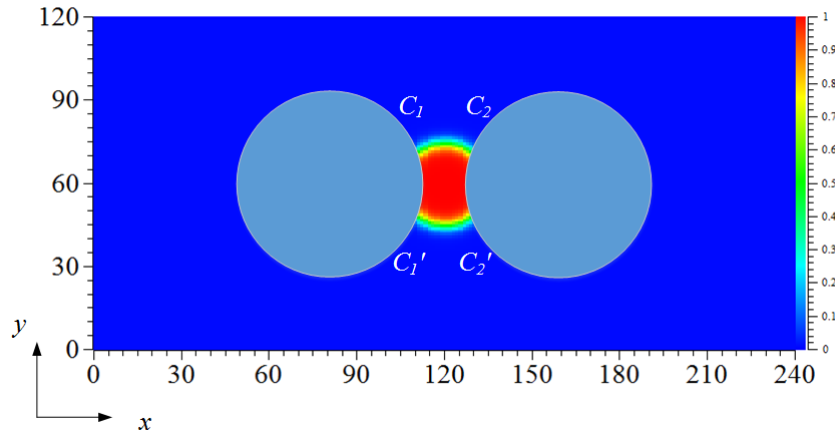
Meanwhile, for the models in this and the following sections in this thesis, because we mainly study the equilibrium state of the models, all of which are in a steady state, in order to simplify the computation, the shear force caused by the shear stress is neglected in this thesis.

4.3.3 Numerical simulation results

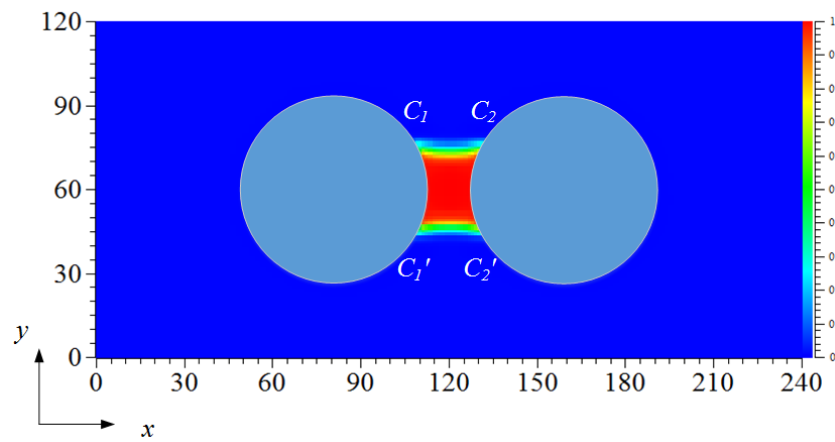
In order to ensure that the system reaches an equilibrium state, the numerical results at 1,000,000th time steps (about 250 hours of CPU time) are studied in the following section and the maximum velocity at this time step is less than 2.0×10^{-6} . In the analysis of numerical results, it could be found that the value of the shear velocity rate is smaller than the value of the maximum velocity. Besides, the velocities far away (> five lattice spaces) from the contact points are always two orders of magnitude less than the maximum velocity. Therefore, with the dynamic viscosity $\mu = \rho \cdot \eta = 0.1$, the

threshold value of velocity 2.0×10^{-6} can ensure that the influence of shear stress is trivial in the simulation.

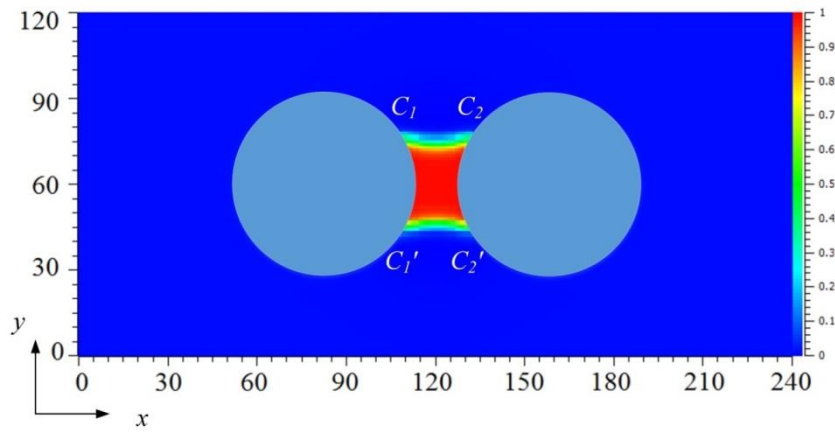
According to the definition of component C in the model, $C=0.5$ is supposed to be the interface of the liquid and vapour in the simulation. In order to calculate the radius of the meniscus with equation (4.12), the y -coordinate values of the interface at axes $x=115$ and $x=120$ are obtained from the component distribution results in three cases at the $1,000,000^{\text{th}}$ time step (illustrated in Figure 4-16, Figure 4-17 and Figure 4-18). The numerical results of capillary pressure and the corresponding analytical solutions are displayed in Table 4-3.



(a) 1st time step

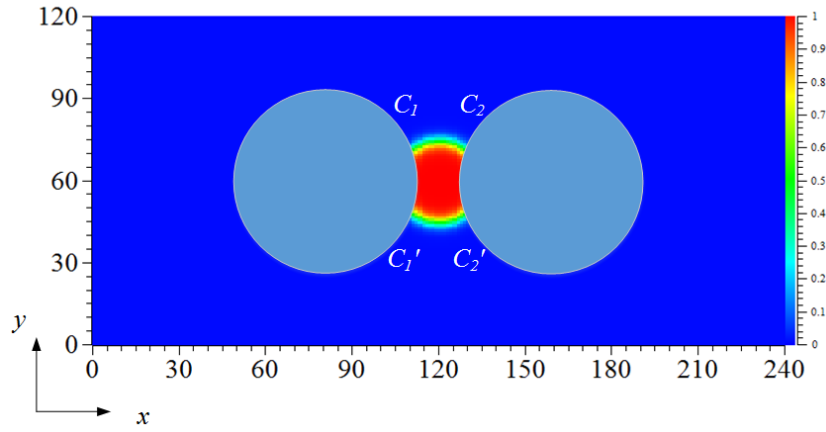


(b) 40,000th time step

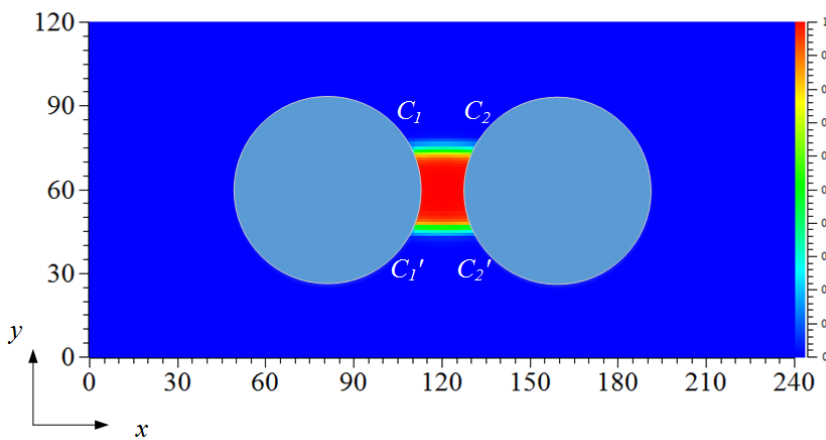


(c) 1,000,000th time step

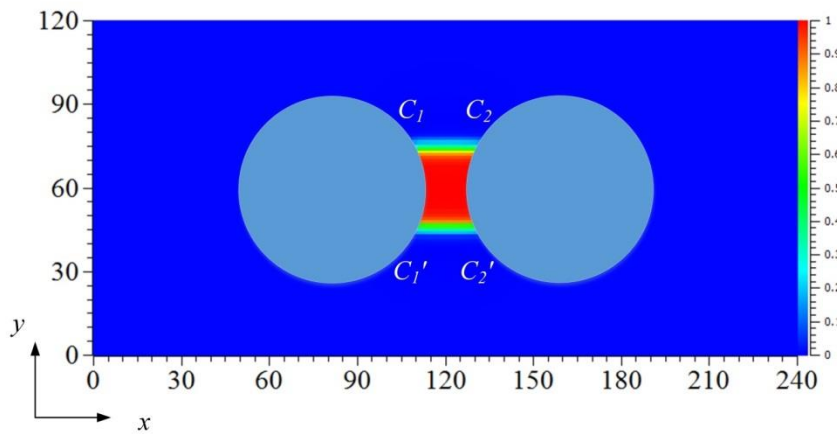
Figure 4-16 Component contour of the capillary bridge model ($\theta=30^\circ$)



(a) 1st time step

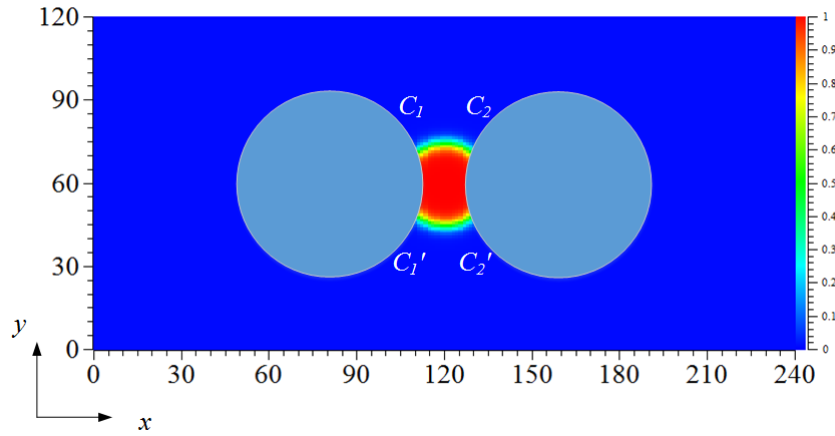


(b) 40,000th time step

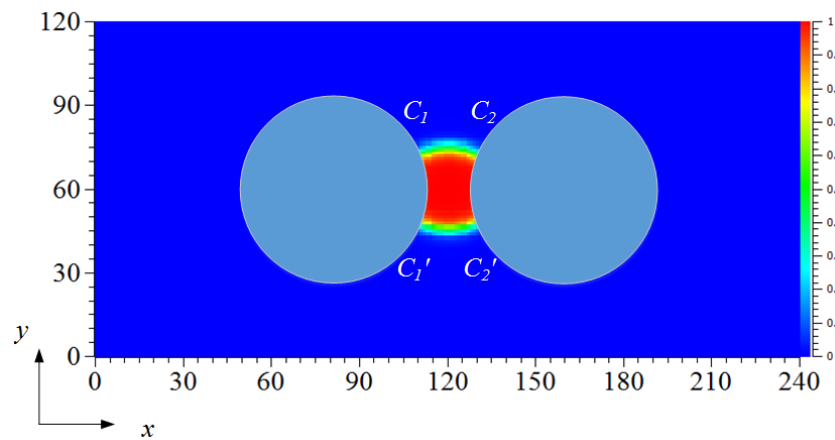


(c) 1,000,000th time step

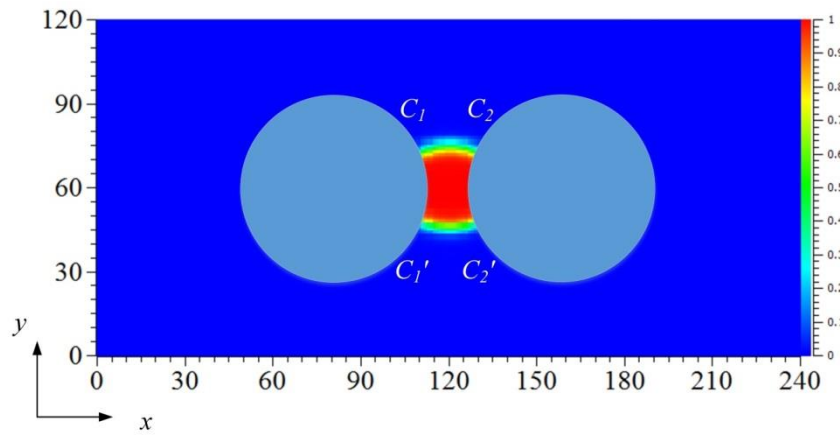
Figure 4-17 Component contour of the capillary bridge model ($\theta = 60^\circ$)



(a) 1st time step



(b) 40,000th time step



(c) 1,000,000th time step

Figure 4-18 Component contour of the capillary bridge model ($\theta=90^\circ$)

Table 4-3 Numerical results of capillary pressure with different contact angles

	Case 1	Case 2	Case 3
Contact Angle θ	30°	60°	90°
Meniscus Radius R	32.3	-818.0	-23.2
Analytical Capillary Pressure P_A	2.252×10^{-6}	-8.893×10^{-8}	-3.14×10^{-6}
Numerical Capillary Pressure P_N	2.169×10^{-6}	-8.381×10^{-8}	-3.18×10^{-6}
Relative Error ($ P_A - P_N / P_A $)	3.7%	5.8%	1.3%

The numerical capillary pressures P_N in Table 4-3 are obtained from the capillary pressure difference in the middle cross-section MM' (illustrated in Figure 4-14) and the total pressure distributions of three different contact angles are plotted in Figure 4-19, Figure 4-20 and Figure 4-21, respectively. In Table 4-3, it shows that the numerical results of capillary pressure agree well with the corresponding numerical solutions and the LB model in this thesis can be used as a tool to predict the capillary pressure value.

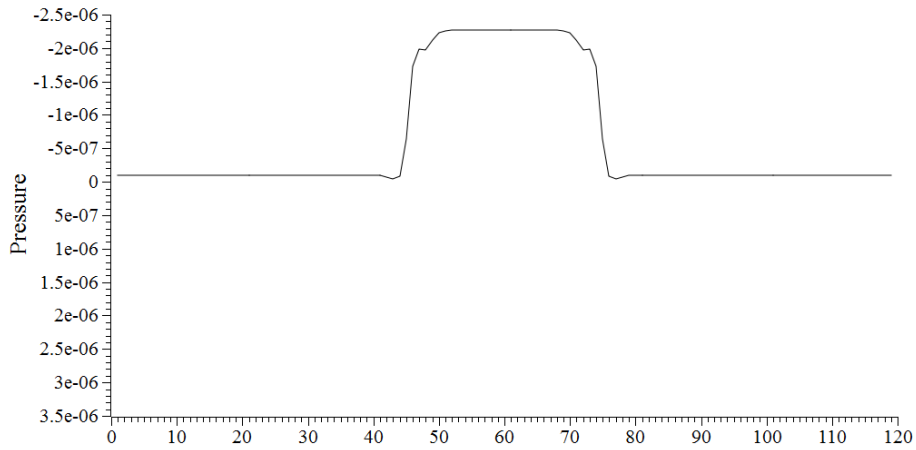


Figure 4-19 Total pressure distribution at cross-section MM ' at the 1,000,000th step
 ($\theta=30^\circ$)

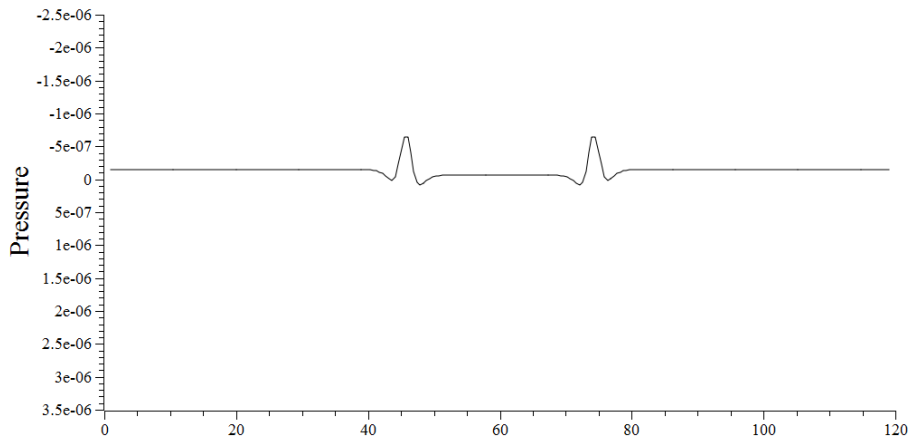


Figure 4-20 Total pressure distribution at cross-section MM ' at the 1,000,000th step
 ($\theta=60^\circ$)

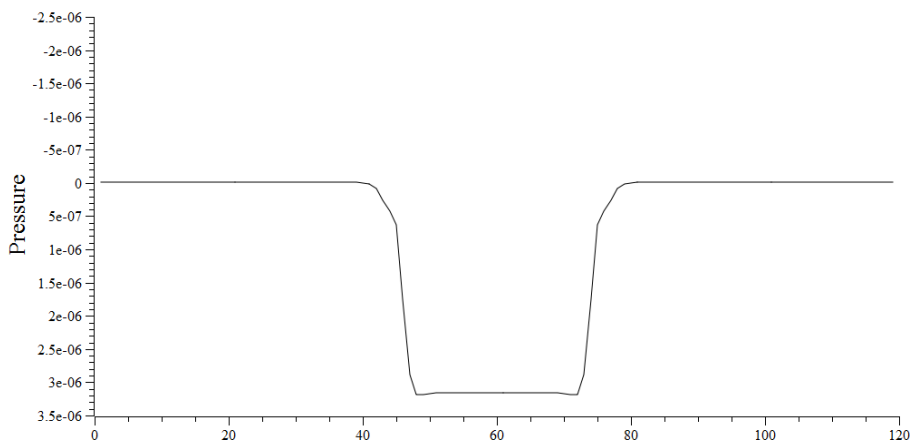


Figure 4-21 Total pressure distribution at cross-section MM ' at the 1,000,000th step
 ($\theta=90^\circ$)

In order to calculate the total capillary force acted on the circular particles, we divide the particle into 1,024 equal-length arcs and $l_p = \frac{2\pi R}{N} \doteq 0.189$. Taking the left circular body illustrated in Figure 4-14 as an example, the total capillary forces acted on the particles and on the cross-section MM' are displayed in .

Table 4-4.

Table 4-4 Total lateral capillary force F calculated in the model

	Case 1	Case 2	Case 3
Contact Angle θ	30°	60°	90°
Slope Angle θ on left particle	-30.3°	0°	20.9°
Capillary Force acted on left particle (F_C)	20.047×10 ⁻⁵	14.453×10 ⁻⁵	5.21×10 ⁻⁵
Capillary Force acted on cross-section MM' (F_M)	20.247×10 ⁻⁵	14.529×10 ⁻⁵	5.48×10 ⁻⁵
Relative Error ($ F_C - F_M /F_M$)	1.0%	0.5%	4.9%

Table 4-4 shows that, based on the total pressure value obtained from the numerical simulation, the new forcing calculation proposed in Section 4.3.2 agrees well with the analytical solutions calculation from the cross-section MM', which indicates that the forcing calculation method can be used to predict the lateral capillary force acted on the particles in the capillary bridge phenomenon.

4.4 Contact line dynamics between two alongside cylinders

In order to examine the robustness of the code in this thesis to manipulate the Two-Phase Flow along the circular boundaries, the capillary rise between two circular bodies is simulated.

Allain and Cloitre (1993) proposed the theoretical solutions for the interface force and geometry characters of the capillary rise between two alongside cylinders. Later, Shinto et al. (2007) used LBM to verify the theoretical solutions with a stepwise boundary and low density ratio (10:1). In this section, similar numerical simulation to

Shinto's is applied (except for the circular boundary and the large density ratio (1000:1)).

In this section, the lateral capillary force between two circular bodies with different circle centre distances L (illustrated in Figure 4-22) is calculated from the numerical simulation results. The corresponding analytical force solutions will be compared with the numerical results to verify the forcing calculation method proposed in Section 4.3.2 in complicated problems. Besides, based on the assumption that the shape of the meniscus between two bodies is an elliptic arc, the contact point distance d (illustrated in Figure 4-22) is compared between the numerical results and the analytical solutions to validate the accuracy of the LB code to simulate the complex capillary rise phenomenon.

4.4.1 Theory of lateral capillary force and geometry characters between two circular bodies

In the system depicted in Figure 4-22, $\zeta(x)$ is the shape of the meniscus formed around the cylinders and $h_i (i=1,2)$ is the vertical position of the central axis of cylinders with respect to the level $y = \zeta(\pm \infty) \equiv 0$. H is the vertical rise of the meniscus between two cylinders in the middle. L and d are the horizontal distances between the centre of cylinders and the capillary contact points, respectively. θ_i and θ_i' are the intersection angles between the contact points and the vertical axis. ψ_i and ψ_i' are the slope angles of the exterior and interior menisci, respectively. $\alpha_i (i=1,2)$ is the contact angle of the corresponding cylinders.

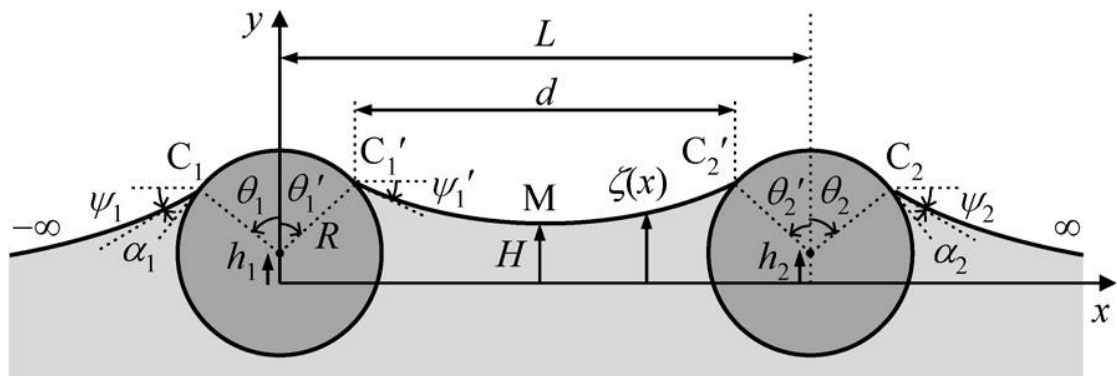


Figure 4-22 Sketch of two horizontal cylinders of radius R fixed at the interface between two fluids (Shinto et al., 2007)

The interaction force per unit length of the cylinder should be the sum of contributions from the surface tension of the menisci and the hydrostatic pressure throughout the cylinder surface. Therefore, the interaction force should be (while taking the left cylinder in Figure 4-22 as an example):

$$F = -\gamma_1 \left[\cos(\theta_1' - \alpha_1) - \cos(\theta_1 - \alpha_1) \right] - B\gamma_1 \left[\frac{1}{2} (\sin^2 \theta_1 - \sin^2 \theta_1') + \frac{h_1}{R} (\cos \theta_1 - \cos \theta_1') \right], \quad (4.17)$$

where

$$B = q^2 R^2 \text{ and } q^2 = \frac{(\rho_1 - \rho_2)g}{\gamma_1}, \quad (4.18)$$

where B and q^{-1} are called the bond number and the capillary length, respectively.

For the cylinders with the same wettability (or the same contact angles in this section) and constrained at the same vertical position ($h_1=h_2=h$), the distance between two contact points d can be expressed as (Shinto et al., 2007; Allain and Cloitre, 1993):

$$qd = \frac{2}{a} \left\{ (2 - a^2) \left[F\left(\frac{\pi}{2}, a\right) - F\left(\frac{\pi - |\psi_1'|}{2}, a\right) \right] - 2 \left[E\left(\frac{\pi}{2}, a\right) - E\left(\frac{\pi - |\psi_1'|}{2}, a\right) \right] \right\}, \quad (4.19)$$

where

$$a = \frac{4}{4 + (qH)^2}. \quad (4.20)$$

On the right-hand side of equation (4.19), function $F(\phi, k)$ and $E(\phi, k)$ are the incomplete elliptic integrals of the first and second kinds, respectively, with ϕ being the amplitude and k the modulus (the sine of the modular angle). Besides, the centre-to-centre distance between the two cylinders can also be calculated as:

$$qL = qd + 2B^{1/2} \sin \theta_1'. \quad (4.21)$$

It should be mentioned that the left-hand side of equation (4.20) given in Shinto et al. (2007) is a^2 , while in a similar equation proposed by Allain and Cloitre (1993), it is a instead of a^2 . In this thesis, the equation proposed by Allain and Cloitre (1993) is used

because some validation tests for this equation have also been proposed in their papers.

With equations (4.17)–(4.21) and the vertical rise H (illustrated in Figure 4-22), the slope angle ψ_1' and the contact point distance d can be uniquely determined.

Therefore, the numerical results are compared with the analytical lateral capillary force and the contact point distance in Section 4.4.3 to validate the accuracy of the LB model.

4.4.2 Numerical simulation details

The simulation domain in this section is 480×120 and confined with solid boundaries (contact angle equals 90°) located around the domain. The gravity acceleration is 9.8×10^{-7} and the density of the liquid and vapour in the simulation is 1.0 and 0.001, respectively. The kinematic viscosity for the liquid is defined as 0.1 and for the vapour is 0.157. Two circular bodies with the same radius $R=30.79$ and wettability (contact angle $\alpha=30^\circ$ and surface tension $\sigma=7.275 \times 10^{-4}$) are located on the axis $y=60$ and symmetrical with respect to the axis $x=240$ in the domain (illustrated in Figure 4-23). Three cases with different cylinders' centre distance L (illustrated in Figure 4-23) (80, 120 and 160) are simulated in the model. Therefore, according to equation (4.18), the bond number B and the capillary length q can be calculated as 1.2758 and 0.03668.

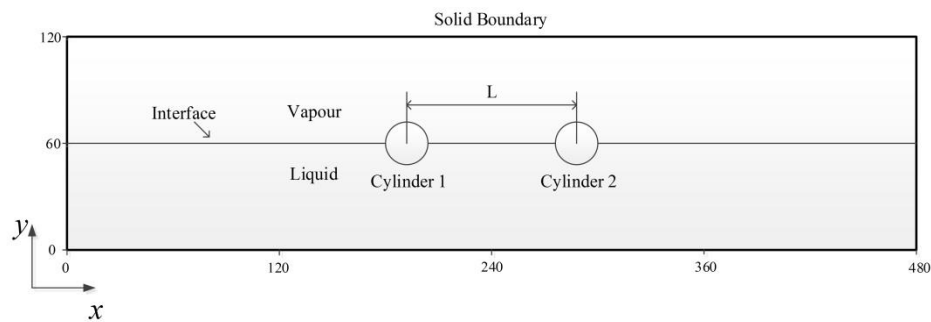


Figure 4-23 Initial state of the computational model used in LBM simulation

$$F_2 = -B\gamma_1 \left[\frac{1}{2} (\sin^2\theta_1 - \sin^2\theta_1') + \frac{h_1}{R} (\cos\theta_1 - \cos\theta_1') \right]. \quad (4.22)$$

From equation (4.17), it can be pointed out that the lateral interaction force consists of two parts: the capillary force dominated by the surface tension on contact points F_1

(the first square brackets on the right-hand side) and the force caused by the gravity due to the uneven distribution of liquid around the cylinders F_2 (the second square brackets on the right-hand side). Since the computation method in the first square bracket in equation (4.17) is the same as the forcing method proposed in Section 4.3.2, in the analysis of numerical simulation results, only the force F_2 (shown in equation (4.22)) is studied in the following section.

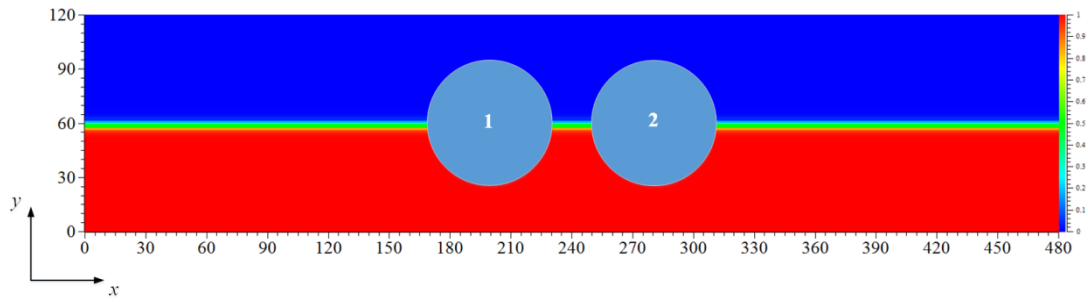
4.4.3 Numerical simulation results

In the following, the force on the left circular particle (Cylinder 1 in Figure 4-23) is analysed and the height of the capillary rise between two bodies is measured through the component contour figures in the first 1,000,000 time steps (about 610 hours of CPU time) illustrated in Figure 4-24, Figure 4-25 and Figure 4-26.

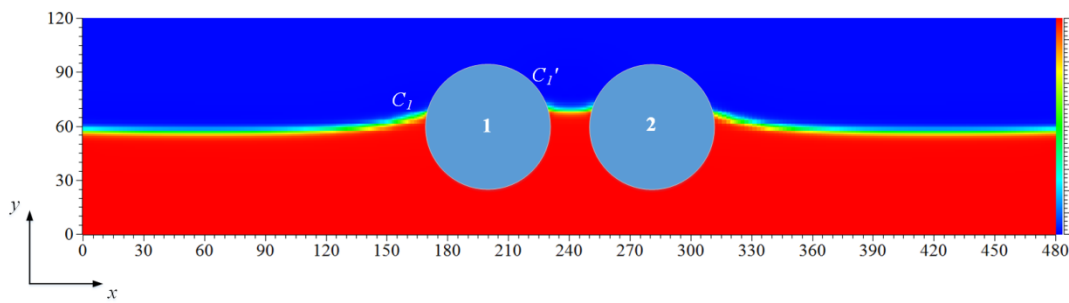
The zero water level is defined as the value of the y -coordinate at $x=0$ or $x=480$ (the values are the same for these two due to the asymmetry), and the vertical position of the circle centre h_1 and the vertical rise of the meniscus H can be measured as the y -coordinate difference with the zero water level. The contact points C_1 and C_1' are read directly from the component distributions from the numerical results to calculate the intersection angles θ_1 and θ_1' . Then the contact distance d in the numerical simulation can be calculated as $d = L - 2.0 \times R \times \sin \theta_1'$.

For the analytical results, the commercial software *Maple* is used in this section to solve the simultaneous equations (equation (4.19) and equation (4.21)) and obtain the analytical contact point distance d and the intersection angle θ_1' .

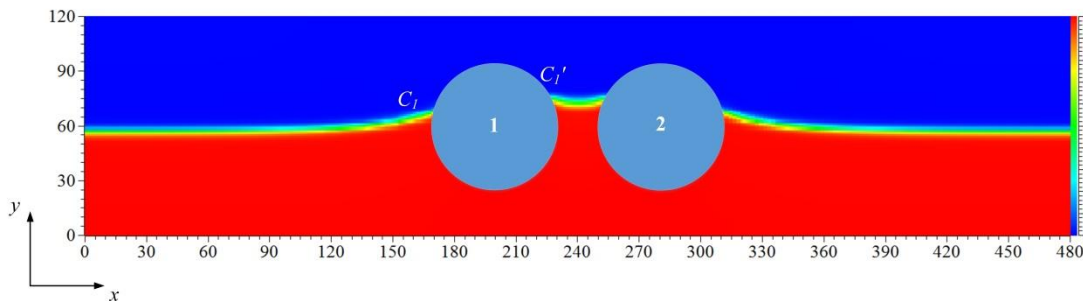
Case 1 ($L=80$)



(a) 1st time step



(b) 40,000th time step



(c) 1,000,000th time step

Figure 4-24 Component contours of two circular bodies ($L=80$)

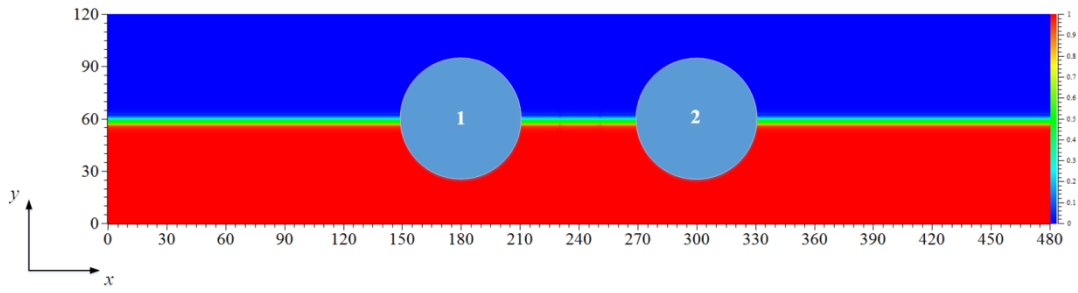
The numerical results for Case 1 are compared with analytical results in Table 4-5 as follows:

Table 4-5 Numerical results of capillary pressure with different contact angles

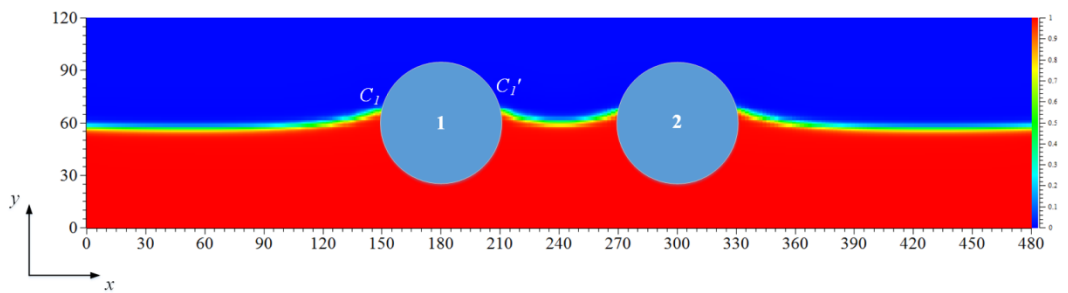
	Numerical	Analytical
Vertical Position of Circle Centre h_1	4.0	-
Vertical Rise of the Meniscus H	16.5	-
Contact Point C_1	(170.6, 69.0)	-
Contact Point C_1'	(226.4, 75.9)	-
Intersection Angle θ_1	73.0°	-
Intersection Angle θ_1'	59.0°	57.8°
Contact Point Distance d	27.2	27.8
Lateral Force caused by Gravity F_2	1.076×10^{-4}	1.103×10^{-4}
Relative Error for θ_1' $(\theta_{1N}' - \theta_{1A}' / \theta_{1A}')$	2.1%	-
Relative Error for d $(d_N - d_A / d_A)$	2.2%	-
Relative Error for F_2 $(d_N - d_A / d_A)$	2.4%	-

The calculation method mentioned in Section 4.3.2 is applied in the force F_2 calculation. The circular body is divided into 1,024 equal-length arcs and $l_p = \frac{2\pi R}{N} \doteq 0.189$.

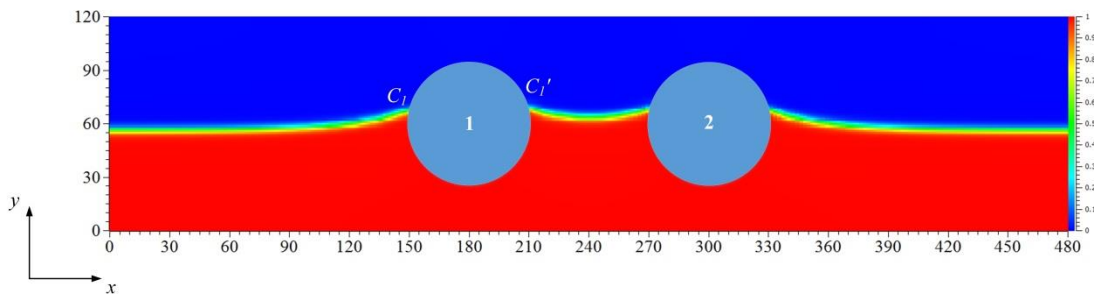
Case 2 ($L=120$)



(a) 1st time step



(b) 40,000th time step



(c) 1,000,000th time step

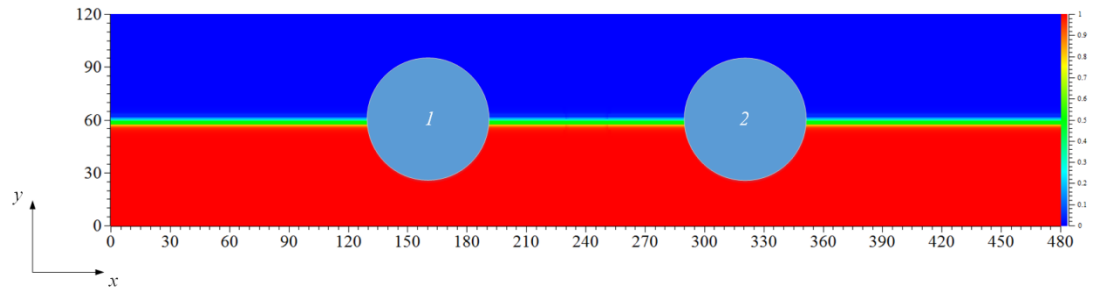
Figure 4-25 Component contours of two circular bodies ($L=120$)

The numerical results for Case 2 are compared with analytical results in Table 4-6 as follows:

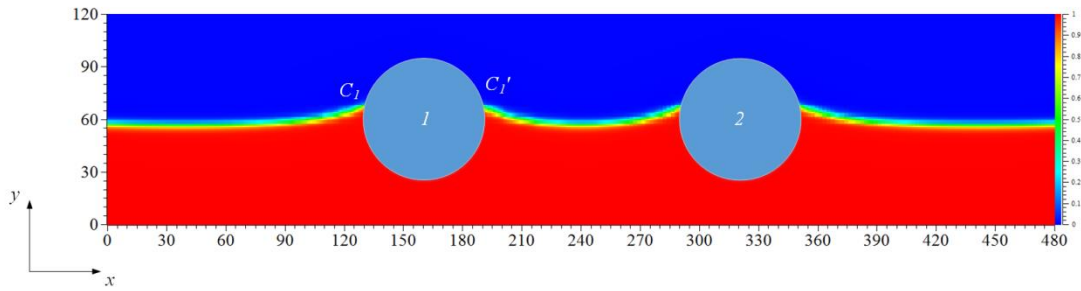
Table 4-6 Numerical results of capillary pressure with different contact angles

	Numerical	Analytical
Vertical Position of Circle Centre h_1	3.6	-
Vertical Rise of the Meniscus H	7.4	-
Contact Point C_1	(150.3, 68.2)	-
Contact Point C_1'	(208.9, 70.5)	-
Intersection Angle θ_1	74.6°	-
Intersection Angle θ_1'	70.0°	64.2°
Contact Point Distance d	62.1	64.6
Lateral Force caused by Gravity F_2	2.932×10^{-5}	2.976×10^{-5}
Relative Error for θ_1' ($ \theta_{1N}' - \theta_{1A}' / \theta_{1A}' $)	9.0%	-
Relative Error for d ($ d_N - d_A / d_A $)	3.9%	-
Relative Error for F_2 ($ d_N - d_A / d_A $)	1.5%	-

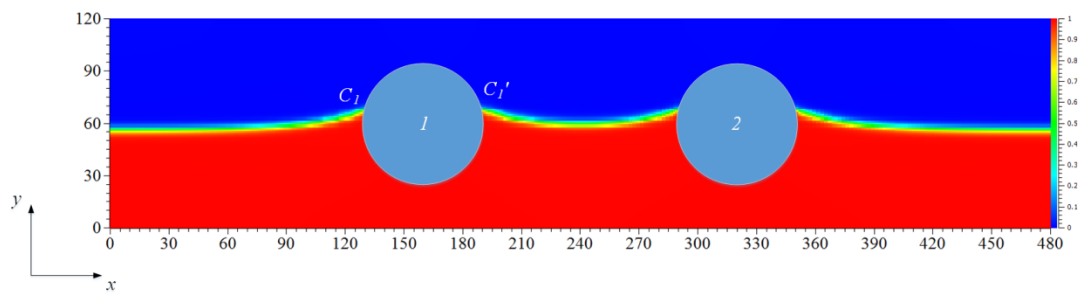
Case 3 ($L=160$)



(a) 1st time step



(b) 40,000th time step



(c) 1,000,000th time step

Figure 4-26 Component contours of two circular bodies ($L=160$)

The numerical results for Case 3 are compared with analytical results in Table 4-7 as follows:

Table 4-7 Numerical results of capillary pressure with different contact angles

	Numerical	Analytical
Vertical Position of Circle Centre h_1	3.6	-
Vertical Rise of the Meniscus H	3.6	-
Contact Point C_1	(130.5, 68.9)	-
Contact Point C_1'	(189.4, 69.0)	-
Intersection Angle θ_1	73.2°	-
Intersection Angle θ_1'	73.0°	67.5°
Contact Point Distance d	101.1	103.1
Lateral Force caused by Gravity F_2	1.302×10^{-6}	1.260×10^{-6}
Relative Error for θ_1' ($ \theta_{1N}' - \theta_{1A}' / \theta_{1A}' $)	8.1%	-
Relative Error for d ($ d_N - d_A / d_A $)	1.9%	-
Relative Error for F_2 ($ d_N - d_A / d_A $)	3.3%	-

From Table 4-5 to Table 4-7, the maximum relative error for F_2 is only 3.3%, which means that the forcing calculation method used in this thesis can predict the force acted on the circular bodies accurately. However, for the simulation of intersection angles, the maximum relative error is as large as 9.0%. It might be the result of the elliptic shape assumption of the meniscus used in the analytical solutions (illustrated in equation (4.19)). For large centre distance L , the influence of surface tension might be dissipated for the middle part of the meniscus, meaning that the elliptic shape assumption can hardly be valid. Although the prediction of intersection angles has a large relative error, due to the larger centre distance L in case 2 and case 3, the relative error for the contact point distance d still shows good agreement between numerical results and analytical ones.

Therefore, it can be concluded that the LB model used in this thesis can accurately predict the two-phase fluid movement between two circular bodies and the forcing calculation method proposed in this thesis can also predict the force acted on the particles precisely.

4.5 Capillary rise in porous media

Capillary rise phenomena in porous media occur routinely in nature and are of significant importance in the study of unsaturated soil. Since the pioneering work of Washburn in 1921, this phenomenon has been studied in many areas, such as packing of particulates, consolidated samples, and the fibrous materials (Lago and Araujo, 2000).

In this section, the capillary rise in idealised circular bodies packing porous media is simulated with the code and also compared with some theoretical solutions to validate the code's ability to simulate two-phase flow in porous media.

4.5.1 Theory of lateral capillary rise in porous media

As shown in Figure 4-27, if Darcy's law is assumed to be valid in the two monophasic regions, the velocity of the capillary rise front v driven by the capillary pressure P_c can be given as (Lago and Araujo, 2000):

$$v = \frac{dh}{dt} = \frac{k}{\phi} \frac{P_c - (\rho_1 - \rho_2)gh}{\mu_1(h+z_R) + \mu_2(L-H-z_R)}, \quad (4.23)$$

where k is the permeability and ϕ is the porosity of the porous sample, ρ_i and μ_i ($i=1,2$) are the density and dynamic viscosity of fluid i , respectively, and H and z_R represent the hydraulic head above and below the reservoir level. L is the height from the free surface of fluid 2 to the base of the porous sample.

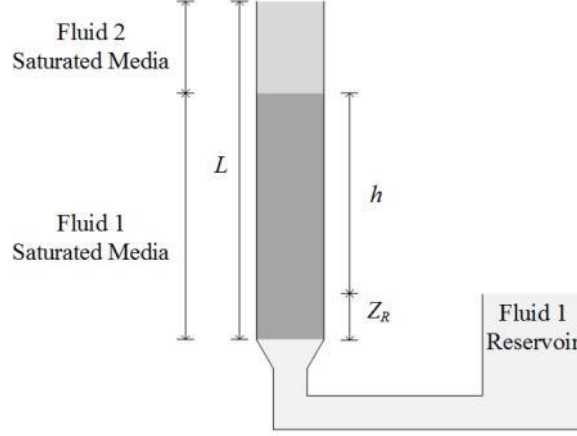


Figure 4-27 Schematic diagram of a capillary rise experiment in a porous sample
(Lago and Araujo, 2000)

The advancing of fluid 1 through the porous sample is only affected by the gravity and the velocity can be simplified as:

$$v_g = \frac{k(\rho_1 - \rho_2)g}{\phi \mu_1}, \quad (4.24)$$

and equation (4.22) can be expressed as:

$$v = \frac{v_g(h_e - h)}{(h + z_R) + \frac{\mu_2}{\mu_1}(L - H - z_R)}, \quad (4.25)$$

where h_e is the hydraulic equilibrium height and can be calculated from the equilibrium condition as follows:

$$P_c = (\rho_1 - \rho_2)gh_e. \quad (4.26)$$

Neglecting the dynamic viscosity term in equation (4.25), the capillary rise equation can be calculated through integration of equation (4.25) as follows:

$$t = \frac{h_e + z_R}{v_g} \ln\left(\frac{h_e}{h_e - h}\right) - \frac{h}{v_g}, \quad (4.27)$$

where the initial condition is $h=0$ and $t=0$.

4.5.2 Numerical simulation details

The simulation domain for the two fluid displacements is 320×160 and 44 circular bodies with three different sizes ($R_1=10.79$, $R_2=6.79$ and $R_3=5.29$) are located in the domain with the same contact angles ($\theta=0^\circ$), as illustrated in Figure 4-28 (Case 1).

Because of the limitation of the computer performance and the low computing efficiency of Lee's model, in this section, only 44 particles could be simulated in this section, though some errors might appear. In fact, even with only 44 particles in this case, the 1,000,000 time steps still require about 540 hours of CPU time for the computation.

In order to increase the accuracy of the measurement, the contact angles for the two sides of plates and solid boundaries are 90° to ensure a flat interface outside the plates. The surface tension is $\sigma = 7.275 \times 10^{-4}$ and the gravity $g = 9.8 \times 10^{-7}$. The original liquid level is at $y=60.0$ and the height difference $h(t)$ between the two interfaces is defined as the capillary rise driven by the surface tension.

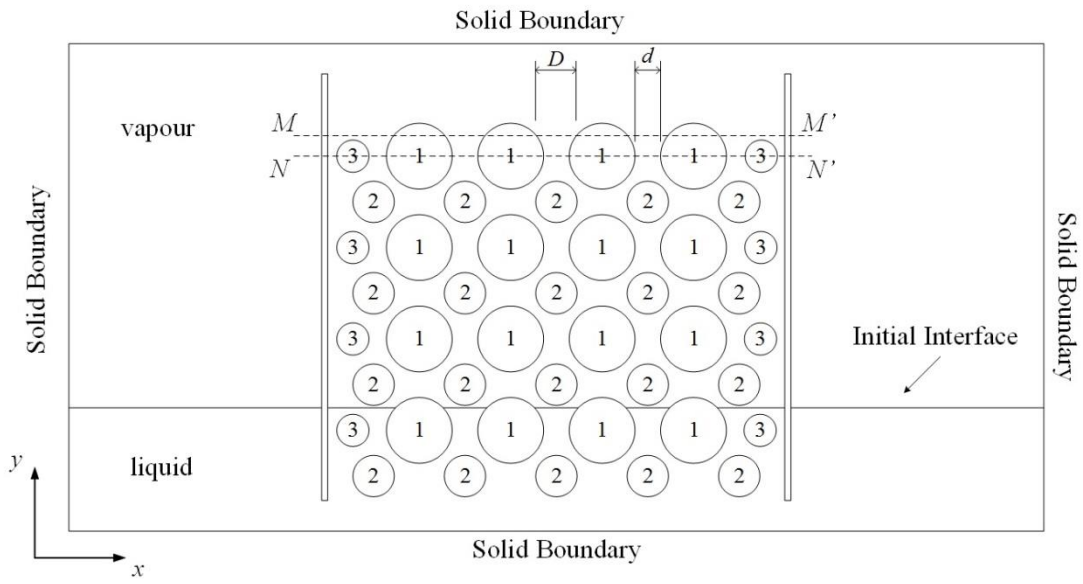


Figure 4-28 Schematic figure of capillary rise in porous media (Case 1)

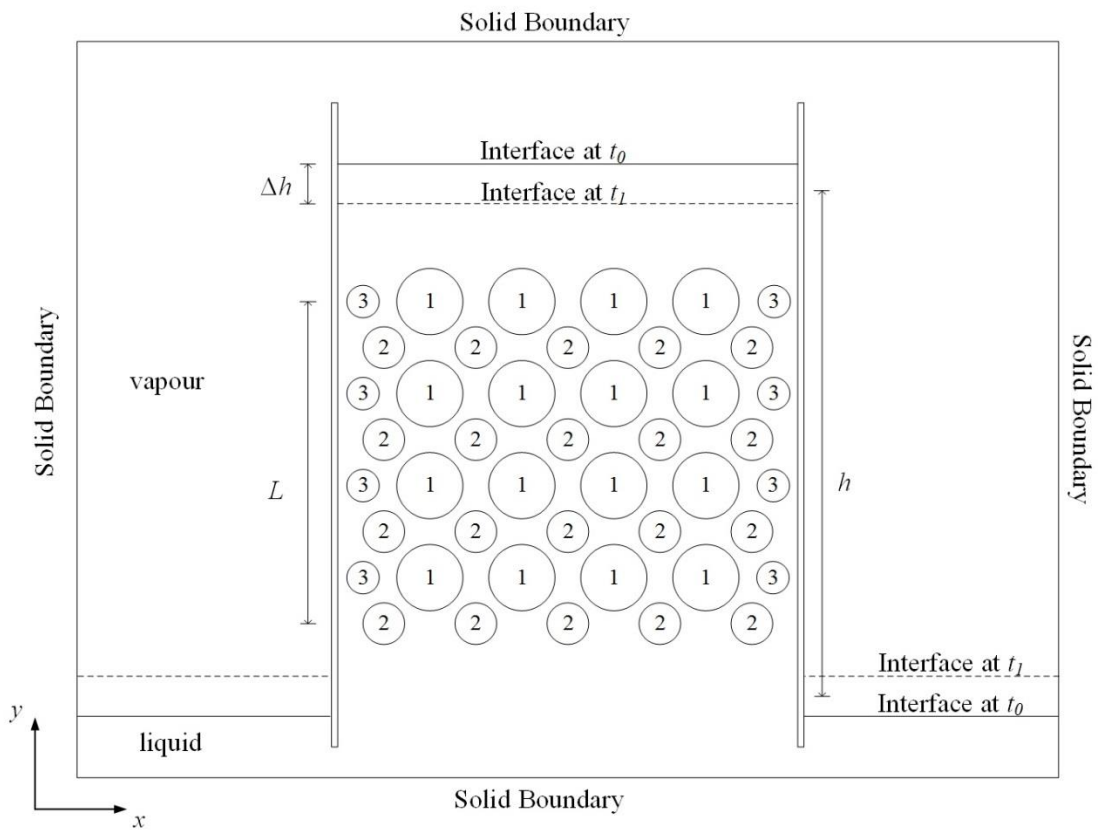


Figure 4-29 Schematic figure of a permeability test in porous media (Case 2)

In order to obtain the permeability parameter in equation (4.24), a simple falling head permeability test (Case 2) is simulated at first. As illustrated in Figure 4-29, a similar numerical case is simulated in this section. The simulation domain for the two fluid

displacements is 320×240 and 44 circular particles with the same position fixed in space and properties as those in Figure 4-28 are located in the domain. The initial liquid level (time t_0) between two plates is $h + \Delta h$ higher than the outside liquid level. Due to the gravitational effect and the mass conservation, when the liquid level falls Δh from time t_1 to t_0 , the liquid level outside the plates would rise Δh at the same time. The vertical distance between the circle centres of circular bodies at the top and the bottom is defined as the length of the porous area (illustrated in Figure 4-29) and can be measured as $L=150$. Therefore, the permeability of the porous area in this model can be calculated as (Gong, 2006):

$$k = \frac{\Delta h \cdot L}{h \cdot (t_1 - t_0)}. \quad (4.28)$$

Based on the initial condition illustrated in Figure 4-28, the height of the sample below the free liquid surface z_R in equation (4.27) equals zero and the equation (4.27) can be simplified as:

$$t = \frac{h_e}{v_g} \ln \left(\frac{h_e}{h_e - h} \right) - \frac{h}{v_g}. \quad (4.29)$$

Although the hydraulic capillary height h_c can be calculated from equation (4.26), due to the complex geometry of the pore system and the different positions of the menisci, it is difficult to estimate the capillary pressure accurately (Lago and Araujo, 2000; Lockington and Parlange, 2004). Therefore, the hydraulic capillary height h_c is obtained from the maximum capillary rise in numerical results for this thesis. With the permeability k and the hydraulic equilibrium height h_e from the numerical results, the numerical result of the capillary rise in porous media is compared with the corresponding analytical solutions of equation (4.27) (or (4.29)).

4.5.3 Numerical simulation results

The falling head permeability test (Case 2) is simulated for one million steps at first. In order to minimise the influence of liquid outside the plates and the initial fluctuation of numerical computation to the measurement of the permeability in the simulation, we only choose the numerical results from the 40,000th time step to the 120,000th time step. In these 80,000 time steps, the interface change $\Delta h=11.88$ and the hydraulic head $h=129.84$. Thus, the permeability $k = 11.88 \cdot 10^5 / (129.84 \cdot 80,000) = 1.20 \times 10^{-4}$.

Then the capillary rise in porous media (Case 1) is simulated for one million time steps. The capillary rise of numerical results in the first one million time steps is plotted in Figure 4-30. From Figure 4-30, it can be found that after about 480,000 time steps, the value of the capillary rise is stable at about 48.7. (The advancing front of the capillary rise is stable near $y=97.9$ and the liquid level outside the plates is stable near $y=49.2$ from Figure 4-37.)

With the permeability and the equilibrium capillary rise obtained from the numerical simulation, the corresponding analytical solutions in the first one million steps are also plotted in Figure 4-30.

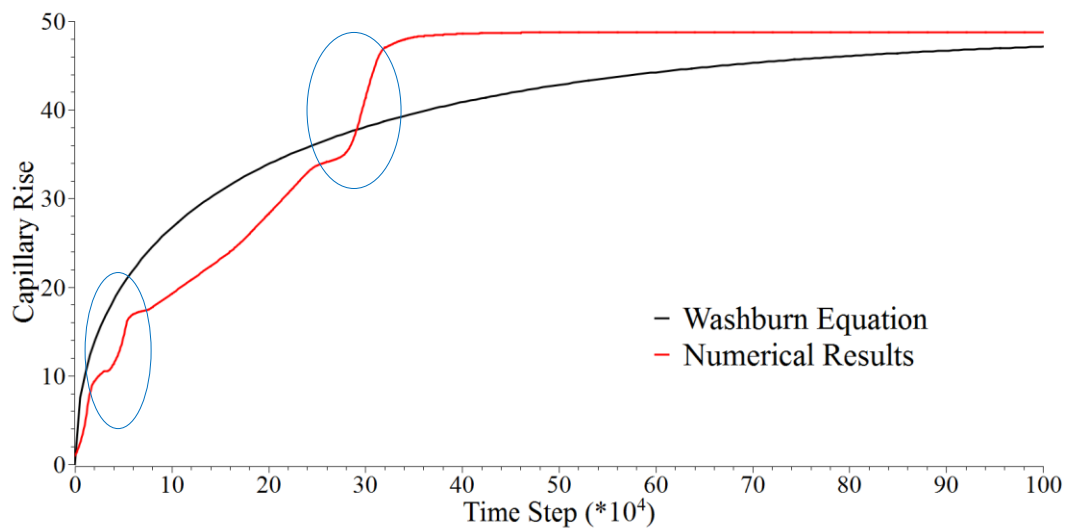


Figure 4-30 Numerical and analytical results for a capillary rise in porous media

For the analytical results, the curve reaches 47.12 (96.7% of the maximum height) at the 1,000,000th time steps and it needs almost 3,000,000 time steps to reach the maximum height in this section. Since Washburn's equation may not be accurate for long-term prediction (Delker et al., 1996; Lockington and Parlange, 2004), only the first 500,000 time steps are discussed in this section.

As illustrated in Figure 4-30, there are two obvious stair-stepping parts in the curve of numerical results from time steps 30,000 to 50,000 and from 280,000 to 300,000. For the Washburn equation, it assumes that the porous media is isotropic and the pores distribute uniformly in the media. However, due to the limitation of the computation, it is difficult to ensure the uniform distribution of pores in the numerical model with only 44 circular particles. Therefore, although the circles are located evenly between

two plates, the geometrical characters have a significant influence on the advancing of the capillary rise as follows:

For a single particle, without regard to the dynamic contact angle phenomenon, the lifting force contributed by the surface tension in the capillary rise can be represented as $\sigma \cdot \cos(\phi)$. Therefore, if the menisci rise from contact point A to C via B (illustrated in Figure 4-31), the lifting force will increase from 0 (at point A) to σ (at point B) and decrease to 0 (at point C), which means that the location of the contact may have a significant influence on the lifting point in the simulation.

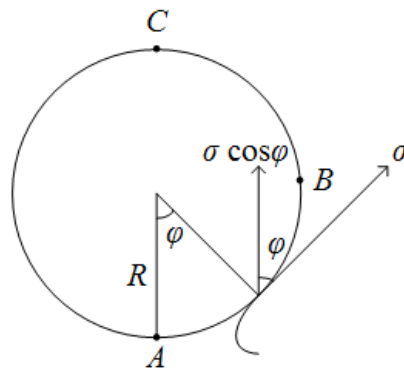


Figure 4-31 Geometrical representation of the contact point of a meniscus with a circle of diameter R (Lago and Araujo, 2001)

Figure 4-32 to Figure 4-36 show the component distribution in the 5,000th, 15,000th, 40,000th, 50,000th and 80,000th time steps. From the 5,000th time step to the 15,000th time step, the void distance D is decreasing and lifting force is increasing, while the corresponding curve in Figure 4-30 shows a concave shape. Later, the distance D is increasing and the lifting force is decreasing with the rise of the liquid until near the 50,000th time step. The corresponding curve becomes slightly stagnant in Figure 4-30. From the 50,000th time step to the 80,000th time step, the average D decreases again (due to the liquid flowing through the path between particle 1 and particle 2) and the lifting force is still small due to the contact point location on the particles. At the same time, the curves show a concave shape again. A similar process happens for the second stair-stepping shape curve in Figure 4-30.

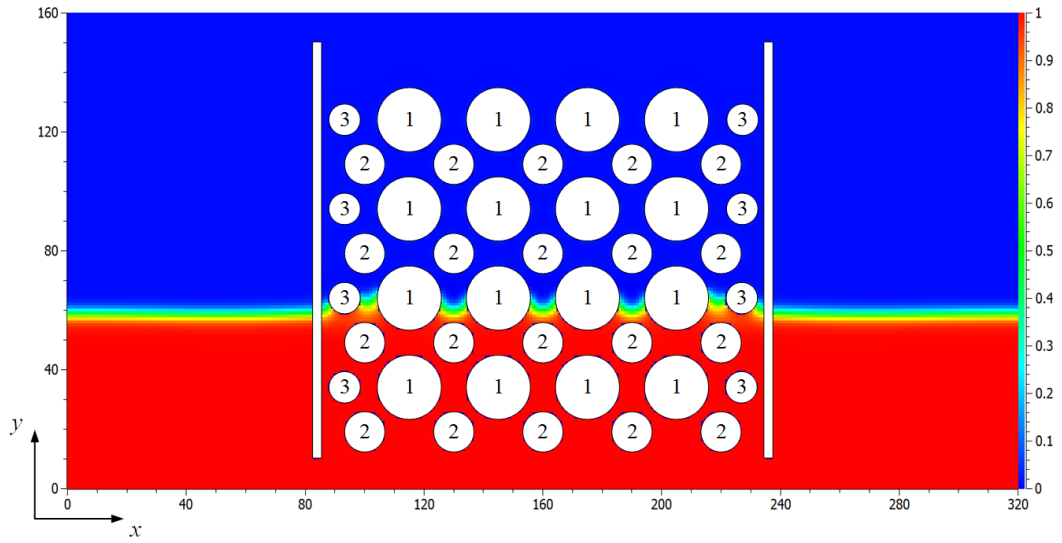


Figure 4-32 Component contour of the capillary rise in porous media in the 5,000th time step

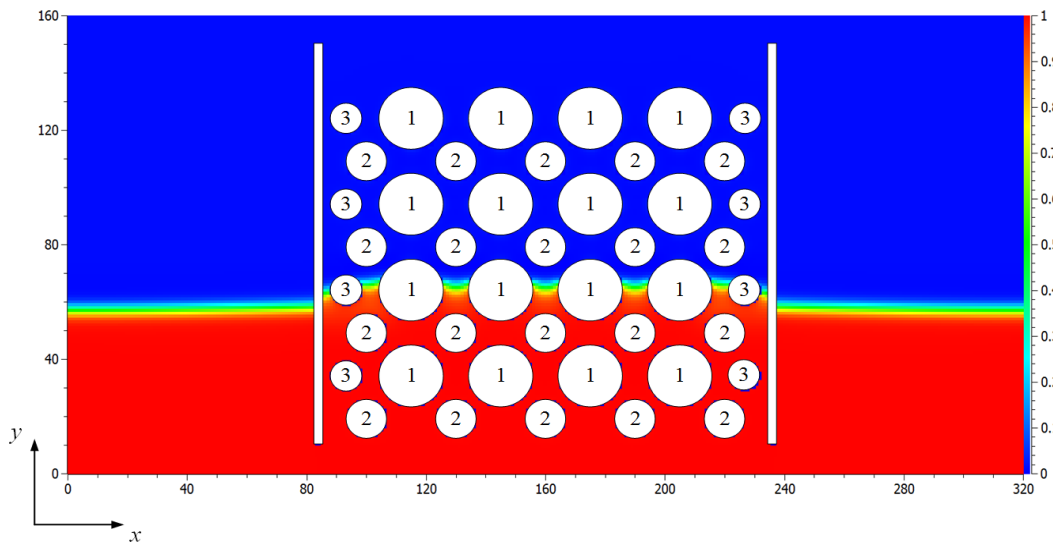


Figure 4-33 Component contour of the capillary rise in porous media in the 15,000th time step

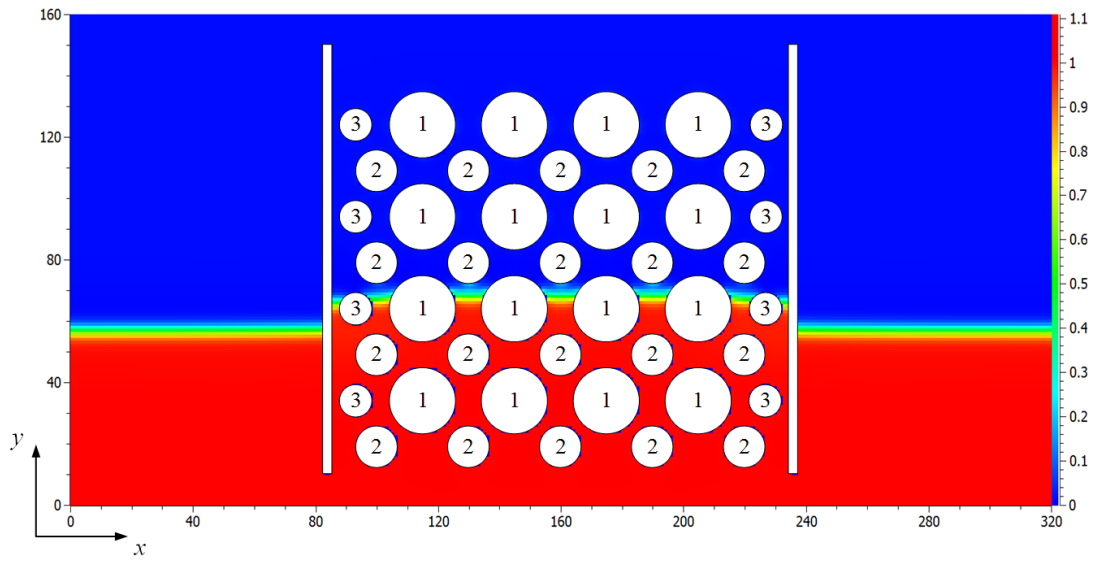


Figure 4-34 Component contour of the capillary rise in porous media in the 40,000th time step

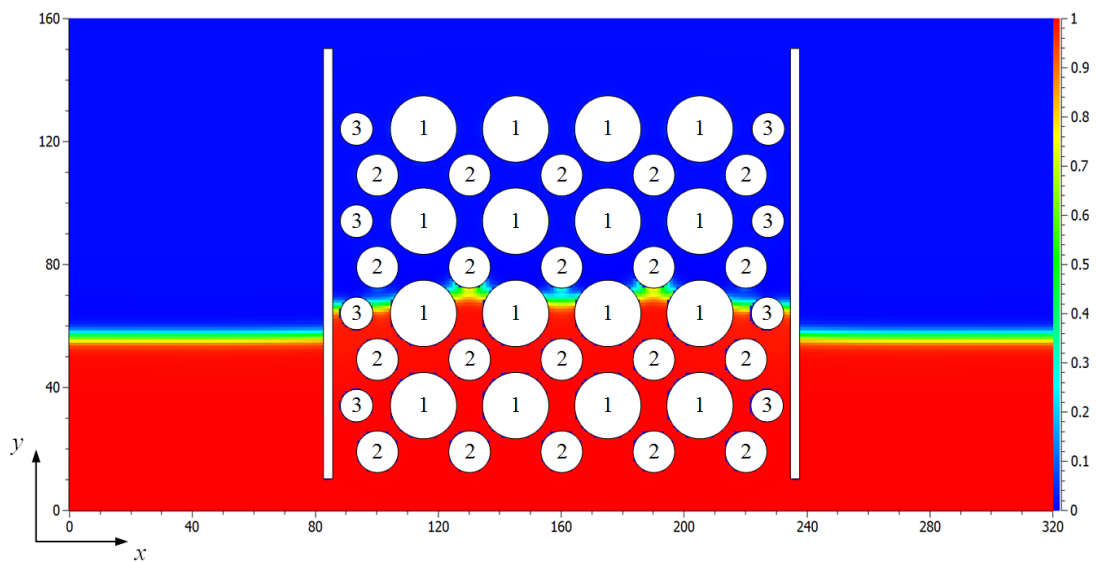


Figure 4-35 Component contour of the capillary rise in porous media in the 50,000th time step

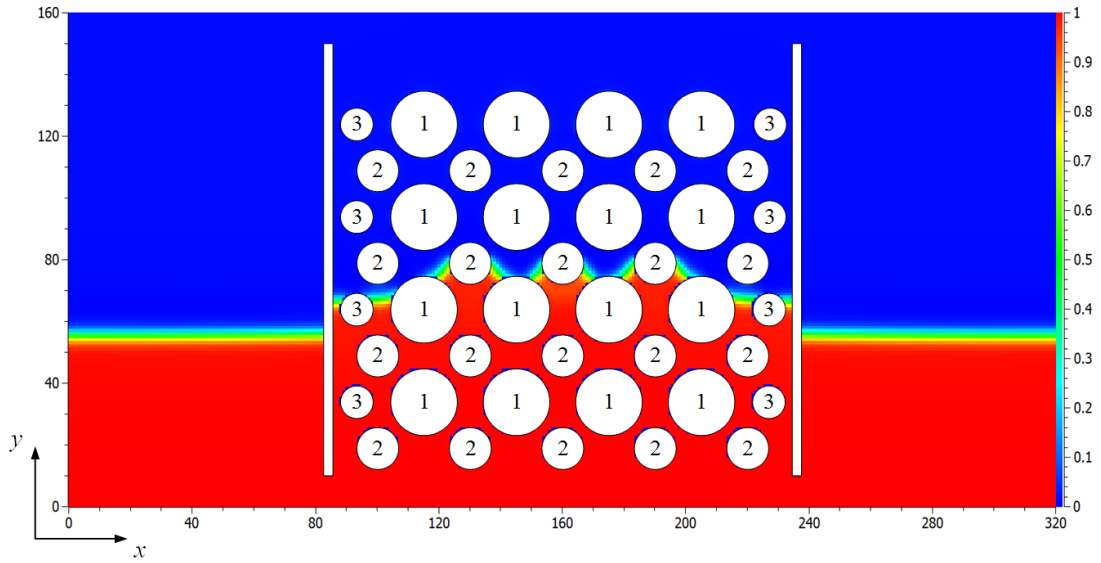


Figure 4-36 Component contour of the capillary rise in porous media in the 80,000th time step

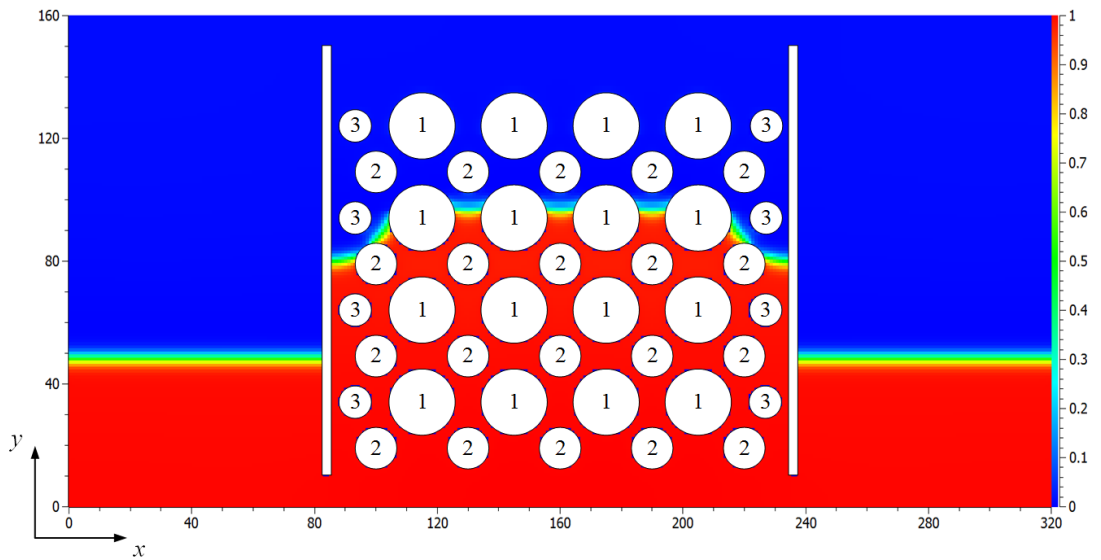


Figure 4-37 Component contour of the capillary rise in porous media in the 480,000th time step

Figure 4-37 shows the component distribution in the 480,000th time step. The capillary rise near the plate boundary stagnates near $y=81.0$, while the equilibrium capillary height for the centre part is near $y=96.9$. The difference might be caused by the non-uniform distribution of the particles, especially those near the plates. Therefore, we would only use the liquid a little far from the plates (from $x=127$ to $x=195$) to analyse the total pressure distribution character in the following.

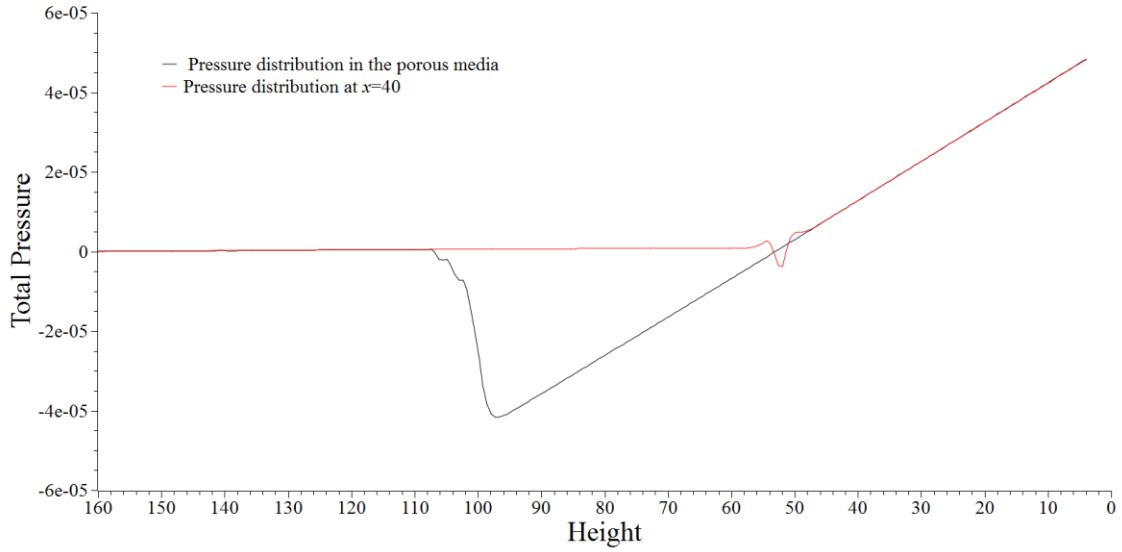


Figure 4-38 Total pressure distribution in the 480,000th time step

Figure 4-38 indicates the pressure distribution in the porous media and outside the plates in the 480,000th time step, respectively. The total pressure inside the plates reaches its minimum value near $y=98$ and the total pressure outside the plates begins to increase from a value close to 0 near $y=50$. Compared with Figure 4-37, it can be found that the turning points of the pressure distribution lines are both near the interface between two fluids, which conforms to the reality that the interface of two different fluids is always the turning point of pressure distribution.

Besides, the pressure distribution curve inside the porous media coincides with the outside pressure distribution curve near $y=50$ and then develops with the same slope $k \doteq 9.82 \times 10^{-7}$. According to equation (4.26), the slope of the curves in Figure 4-38 should be $(\rho_1 - \rho_2)g = 0.999 * 9.8 \times 10^{-7} \doteq 9.79 \times 10^{-7}$. Therefore, the numerical value of the pressure distribution slope only has a 0.3% relative difference from the analytical value.

Furthermore, the theoretical minimum pressure inside the porous media according to equation (4.26) should be $-48.7 \times 9.82 \times 10^{-7} = -4.78 \times 10^{-5}$, while the minimum value indicated by Figure 4-38 is about -4.17×10^{-5} , which has a 12.7% error relative to the analytical results.

Although the capillary rise rate and the total pressure distribution curve have an obvious error with the analytical solutions, it can still show that the LB model has the

ability to simulate the multiphase flow in porous media, even with such a simple numerical model in this section.

4.6 Summary

In this chapter, verifications are carried out to evaluate the algorithms and implementation in Chapter 3.

Firstly, the code in this thesis is verified with the droplet test to evaluate its ability in modelling the two-phase fluid problems with a large density ratio (1:1000). Good qualitative agreements between the numerical results and the analytical ones have been achieved and the droplet radius is also stable during the numerical computation, with only 1.3% shrinkage compared to the initial value, which proves that the code developed in this thesis can simulate the multiphase fluids system with a large density ratio accurately.

Then the capillary rise test is simulated to gauge the ability of GF-IBM with LBM to model the multiphase flow along simple geometrical boundaries. Due to the different assumption about the contact angle at the initial time steps, there are errors between the numerical results and the analytical ones on the capillary rise rate curves; however, the good agreements have been achieved on the height of the capillary rise and the pressure distribution.

The GF-IBM model is also evaluated with the capillary bridge test and the contact line dynamics test in Section 4.3 and Section 4.4. The GF-IBM model illustrates a good ability to predict the movement of the meniscus along the curved boundary. Besides, a new forcing calculation method based on the Immersed Boundary Method is proved to be accurate with the predicted force value validated against the corresponding theoretical ones between two circular particles.

In Section 4.5, the capillary rise in the porous media model is simulated with the verified code to validate its ability in complex multiphase flow in porous media. Due to the limitation of the computer performance, the porous media only consists of 44 circular particles and an obvious disagreement is found between the numerical capillary rise and the analytical solutions. It still shows that the code can deal with the complex flow in complex geometrical boundary models.

In this chapter, in order to reduce the computing CPU time and ensure the stability of the model, some parameters, including the interface thickness, the mobility, the domain size and the grid resolution, are fixed in the simulation and further parametric studies will be conducted in the next chapter.

Chapter 5 Parametric Study

In order to gauge the influence of the LBM code in this thesis, a series of two-dimensional analysis is conducted to evaluate the effect of four numerical parameters in the simulation, including the interface thickness (Section 5.1), mobility (Section 5.2), domain size (Section 5.3), and grid resolution (Section 5.4).

5.1 Interface thickness dependence

In the LB model used in this thesis, the diffuse interface method is applied in the computation. Instead of regarding the interface between two fluids as a zero-thickness surface endowed with the physical properties, the diffuse interface method treats the interface as a non-zero special zone with all physical quantities continuous across it (Anderson et al., 1998). For the physical quantity gradients across the interface appearing in the LB model computations, it is easy to be understood that the thicker the interface, the smoother the physical parameter gradients across the interface.

In this section, the effects of the interface thickness on the LB model results are studied by the contact line dynamics test between two alongside cylinders with five different interface thicknesses S (3, 5, 7, 9, 11), and the geometrical characters (the vertical rise between two cylinders) are compared with each other to estimate the influence of the parameter S .

5.1.1 Numerical simulation details

The simulation domain (480×120) in this section is confined with solid boundaries (contact angle equals 90°) located around it. The gravity acceleration is 9.8×10^{-7} and the density of the liquid and vapour in the simulation is 1.0 and 0.001, respectively. The kinematic viscosity for the liquid is defined as 0.1 and for the vapour is 0.157. Two circular bodies with the same radius $R=30.79$ and wettability (contact angle $\alpha = 30^\circ$ and surface tension $\sigma = 7.275 \times 10^{-4}$) are located on the axis $y=60$ and symmetrical with respect to the axis $x=240$ in the domain (illustrated in Figure 5-1).

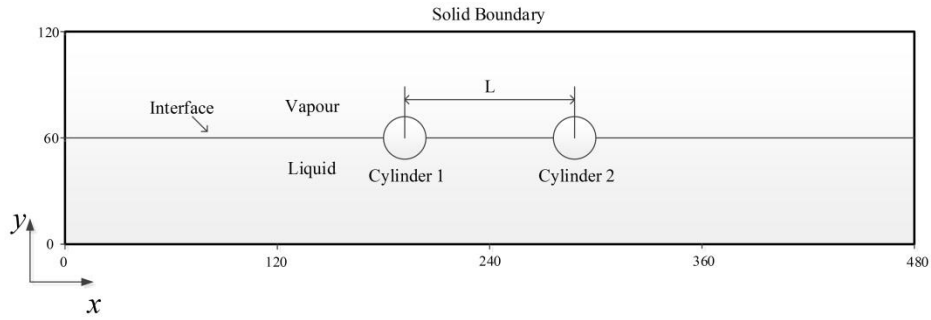
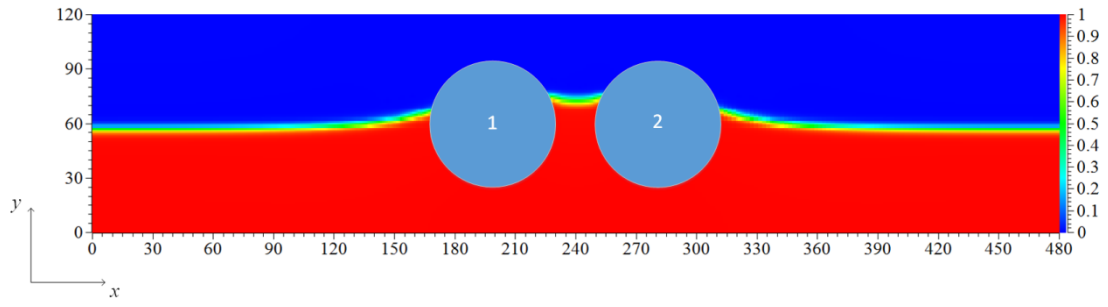


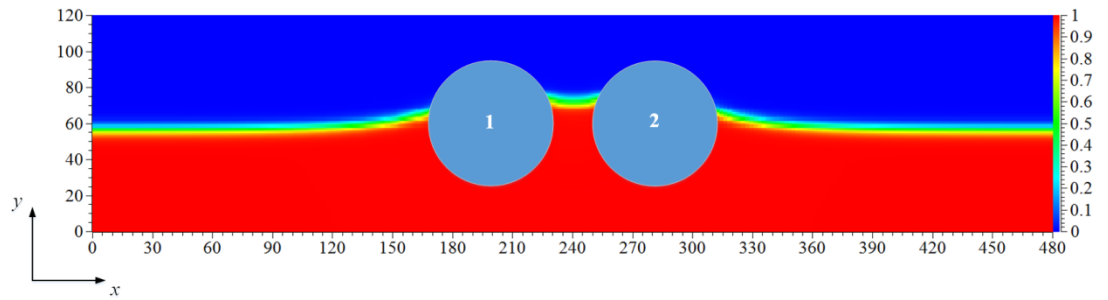
Figure 5-1 Initial state of the computational model used in LBM simulation

5.1.2 Numerical simulation results

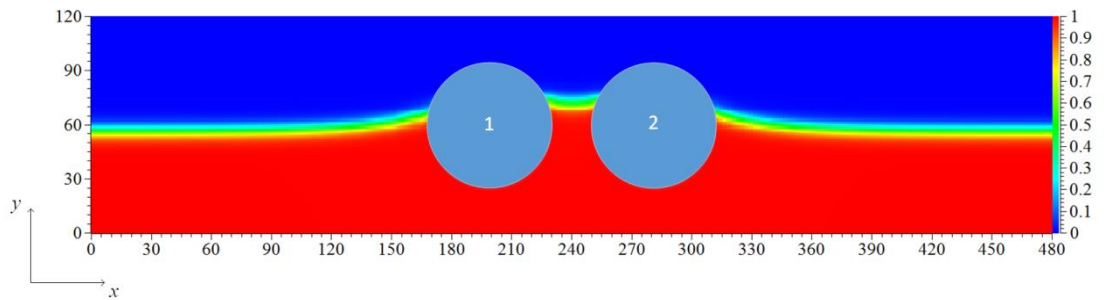
The numerical simulation for $S=3$ becomes unstable and the interface shape is distorted at the first 1,000 time steps, which is consistent with the result in Lee's numerical experiments (Lee and Fischer, 2006) that the numerically sustainable interface thickness should be greater than 3.0. For the other four results, the component contours in the 1,000,000th time steps are illustrated in Figure 5-2.



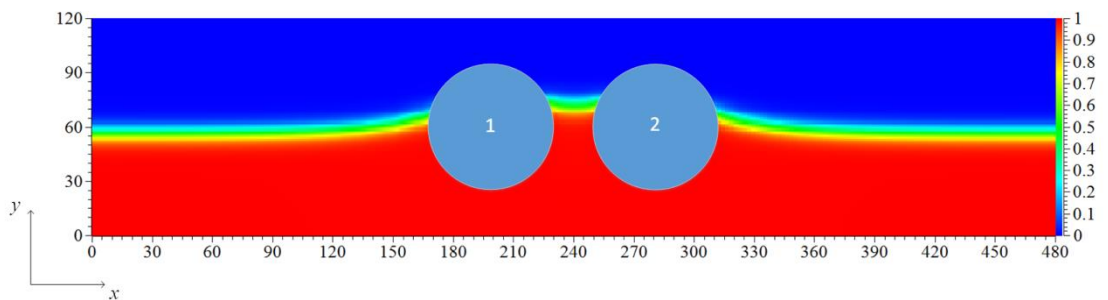
(a) $S=5$



(b) $S=7$



(c) $S=9$



(d) $S=11$

Figure 5-2 Component contours of two circular bodies in the 1,000,000th step ($S=5,7,9,11$)

In Figure 5-2, the green zone in the component contours represents the component value near 0.5, i.e. it stands for the interface areas between two different fluids in the model. It is interesting to find that with the increase in the interface thickness, the interface areas in Figure 5-2 also become wider.

To further study the influence of interface thickness on the model, the intermolecular force F (calculation method is shown in equation (3.14)) along the axis $x=240$ is plotted in Figure 5-3. Compared with Figure 5-2, it can be found that the intermolecular force F mainly changed in the interface areas in the model (or the green zone in the component contours). Besides, although the peak of the intermolecular force F decreases with the increase in the thickness S , the areas under each curve stay similar (from -0.332 to -0.329), which means that the increase in the thickness has little influence on the total lifting force incurred by the surface tension, but it would help to smooth the sharp change of the physical quantities across the interface in the numerical computation.

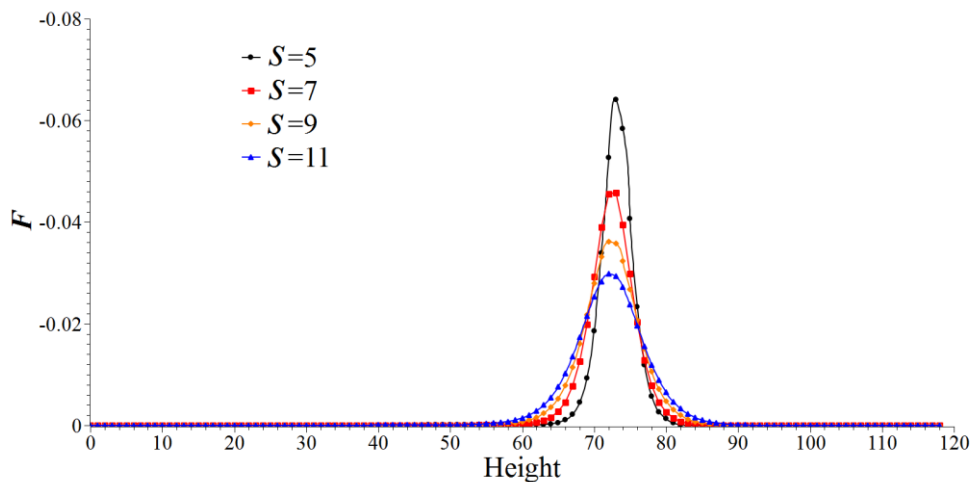


Figure 5-3 Intermolecular force (F) at the axis $x=240$ with different interface thickness (S) in the 1,000,000th time step

Then the corresponding vertical rises of the meniscus (the height difference of the meniscus at axes $x=240$ and $x=0$) are also plotted in Figure 5-4.

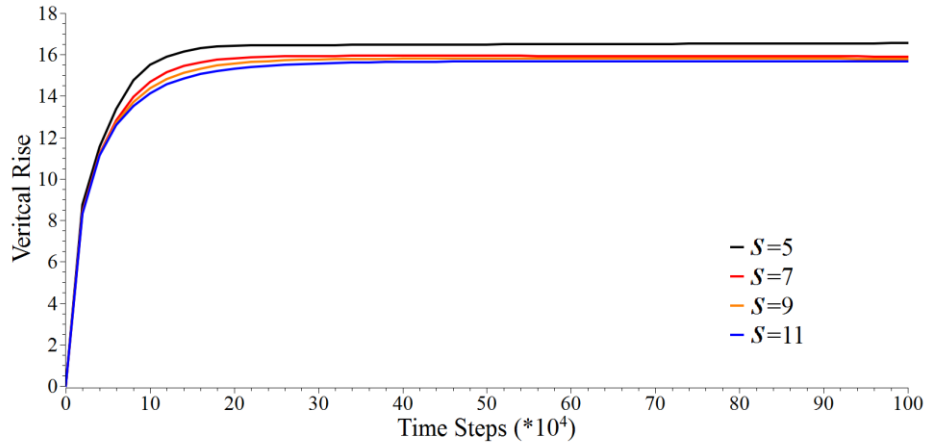


Figure 5-4 Vertical rises (H) with different interface thickness (S) in the first 1,000,000 time steps

In Figure 5-4, it shows that the stable vertical rise H in the 1,000,000th time step decreases with the increase in the interface thickness S . When S is only 5, the vertical rise H is 16.1; when S increases to 11, the vertical rise H decreases to 15.7. The decrease of the vertical rise might be caused by the impractical interface thickness in the simulation. The non-zero interface thickness assumption used in the LB model in this thesis aims to smooth the discontinuous fluid properties across the interface. However, the finite interface thickness in the LB model is different from the negligible interface thickness in reality and the interface thickness in reality can hardly be larger than 1/100 of the ball radius, like the LB models in this section.

Therefore, the increase in the interface thickness can contribute to increasing the stability of the numerical computation by polishing the sharp physical gradient change in computation and it also has little effect on the total force acted on the meniscus in the numerical computation. Nevertheless, since the assumption of the meniscus interface thickness disagrees with the reality, the large interface thickness S in the simulation might make the numerical model different from the real problem we studied and destroy the accuracy of the numerical results.

5.2 Mobility dependence

The parameter mobility M in equation (3.12)(3.12), indeed, is the diffusion coefficient D used in Fick's equation and numerous other equations in physical chemistry. It

represents the ability of molecular flux between two different species; the higher the diffusivity, the faster they diffuse into each other (Mass diffusivity, 2015).

In Chapter 4, the mobility M is fixed at the value 0.5 to decrease the computation time. In this section, in order to investigate the effect of mobility on the numerical results, five contact line dynamics tests between two alongside cylinders with different mobility values (0.0005, 0.005, 0.05, 0.5 and 5.0) are carried out and the geometrical characters are studied to evaluate the effect of the mobility on the results of the numerical simulation.

5.2.1 Numerical simulation details

The simulation domain in this section is 480×120 and confined with solid boundaries (contact angle equals 90°) located around the domain. The gravity acceleration is 9.8×10^{-7} and the density of the liquid and vapour in the simulation is 1.0 and 0.001, respectively. The kinematic viscosity for the liquid is defined as 0.1 and for the vapour is 0.157. Two circular bodies with the same radius $R=30.79$ and wettability (contact angle $\alpha=30^\circ$ and surface tension $\sigma=7.275 \times 10^{-4}$) are located on the axis $y=60$ and symmetrical with respect to the axis $x=240$ in the domain (illustrated in Figure 5-5).

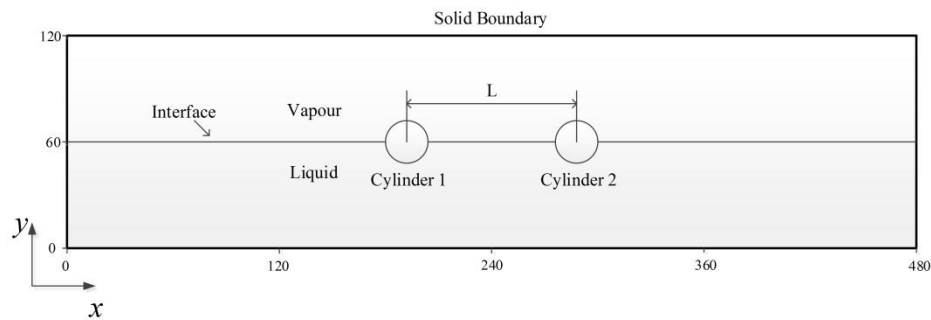


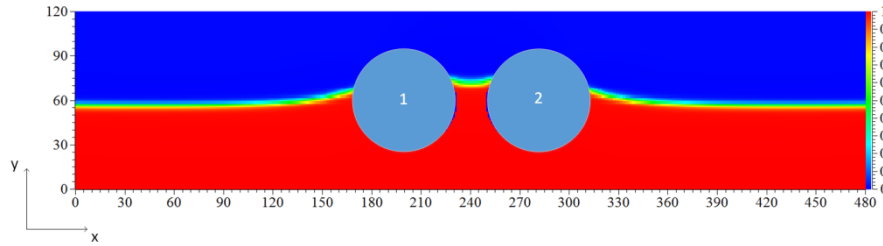
Figure 5-5 Initial state of the computational model used in LBM simulation

5.2.2 Numerical simulation results

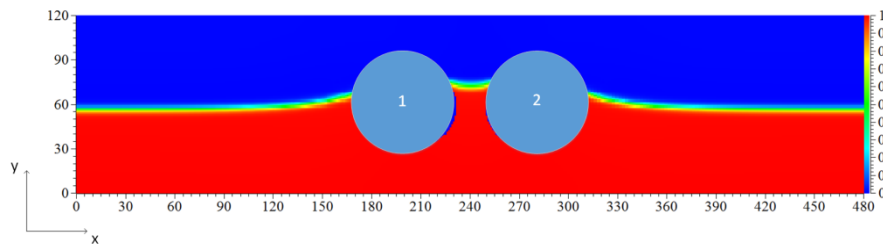
The numerical simulation for $M=5.0$ becomes unstable and the interface shape is distorted at the first 1,000 time steps. The instability might be caused by the shear stress near the contact points between the meniscus and the circular particles. In the LB model in this section, the fluids in simulation are Newtonian fluids and the shear force should be in direct proportion to the derivative of velocity. Since the mobility

reflects the diffuse velocity between two species, the higher the mobility, the faster the meniscus would rise at the first several thousand steps in the computation, which would damage the accuracy of the extrapolation with the GF-IBM method near the boundary and lead to distortion of the interface.

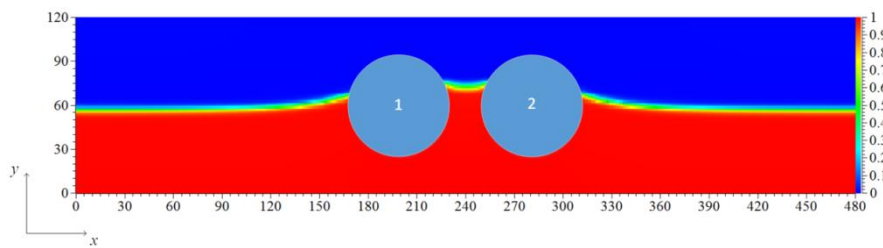
For the other four cases, Figure 5-6 to Figure 5-9 show the component contours of four cases with different mobility (from 0.5 to 0.0005) at different time steps. The component contours at the 100,000th time step illustrate the effect of mobility in these four figures obviously: with the decrease of the mobility M , the vertical rises of the meniscus between two circular bodies decline at the same time. In order to further analyse the influence of the mobility on the convergence of the numerical system, the vertical rises of the meniscus (the height difference of the meniscus at axes $x=240$ and $x=0$) are plotted in Figure 5-10.



(a) 100,000th time step

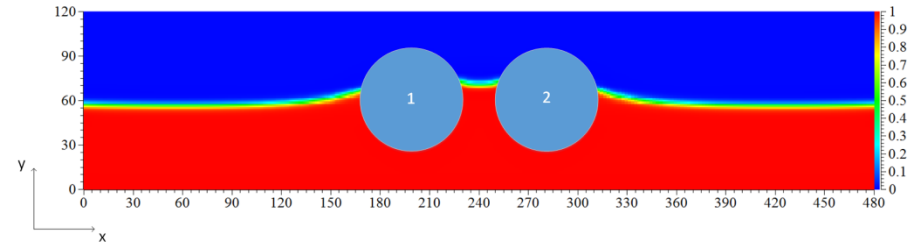


(b) 400,000th time step

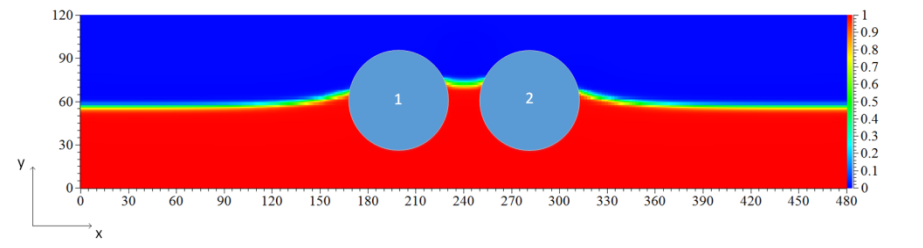


(c) 1,200,000th time step

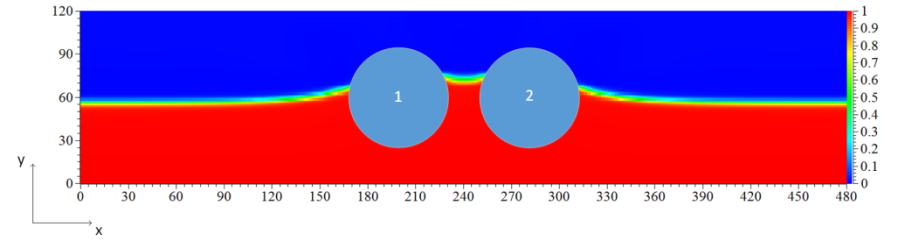
Figure 5-6 Component contours of two circular bodies ($M=0.5$)



(a) 100,000th time step

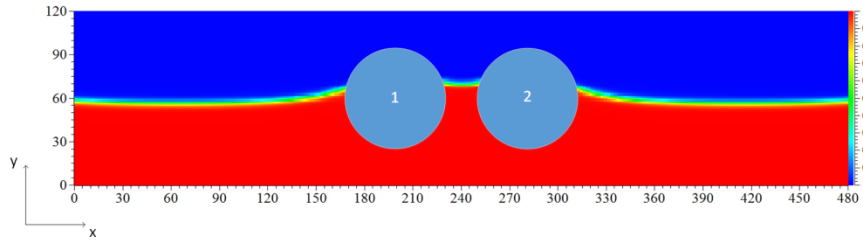


(b) 400,000th time step

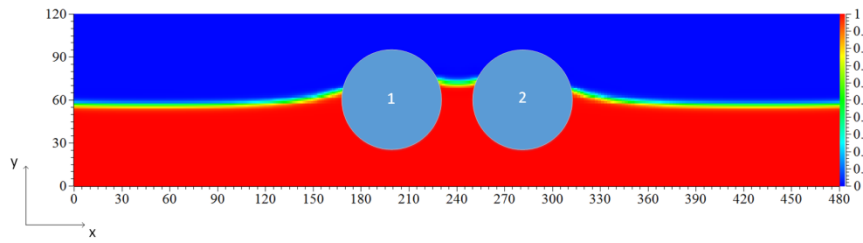


(c) 1,200,000th time step

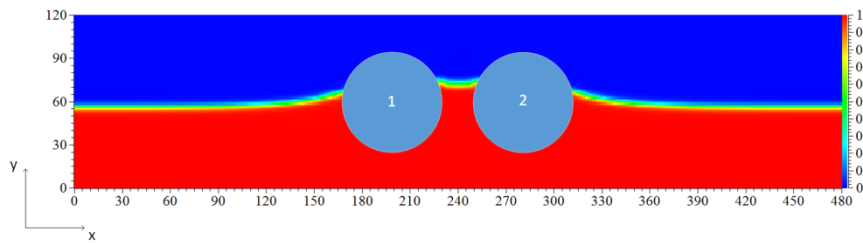
Figure 5-7 Component contours of two circular bodies ($M=0.05$)



(a) 100,000th time step

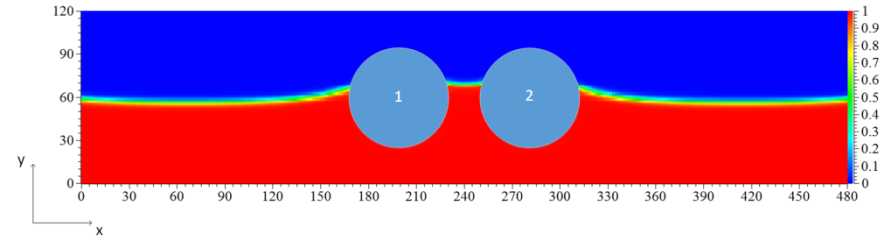


(b) 400,000th time step

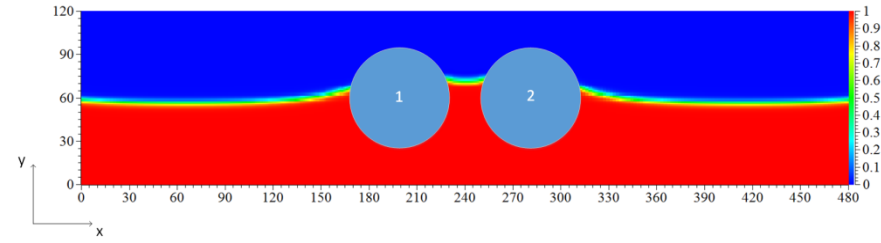


(c) 1,200,000th time step

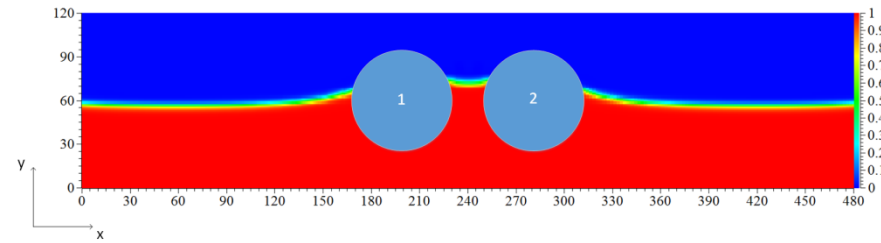
Figure 5-8 Component contours of two circular bodies ($M=0.005$)



(a) 100,000th time step



(b) 400,000th time step



(c) 1,200,000th time step

Figure 5-9 Component contours of two circular bodies ($M=0.0005$)

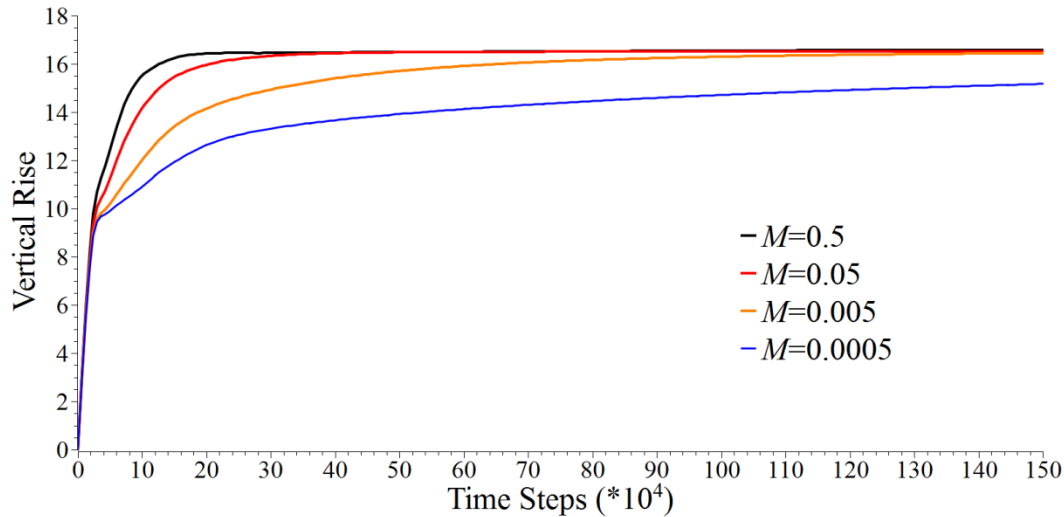


Figure 5-10 Vertical rises (H) with different mobility (M) in the first 1,500,000 time steps

From Figure 5-10, it can be found that, despite the different convergence rate to the maximum vertical rise for different cases, the first three cases ($M=0.5$, 0.05 and 0.005) all reach a similar value of vertical rise (from 16.54 to 16.51) in the first 1,500,000 time steps. Besides, with the decrease of mobility, the equilibrium time for the maximum vertical rise is extended obviously. The time steps for these four cases are illustrated in Table 5-1, which indicates that when the mobility decreases from 0.5 to 0.0005 , the time steps for the equilibrium time soar from $380,000$ (about 232 hours of CPU time) to $5,600,000$ (nearly $3,400$ hours of CPU time).

Table 5-1 Time steps required for the maximum vertical rise

Mobility	0.5	0.05	0.005	0.0005
Time steps required for maximum vertical rise ($\times 10^4$)	38	46	162	560

As a result, on the one hand, the system would be unstable and the interface would distort with large mobility in the simulation. On the other hand, higher mobility M also means faster convergence to the equilibrium state. Lee (2009) recommended a simple equation for mobility in the droplet test ($M \times \beta = 0.02$). But for some complicated cases, such as the cases in this section, the value of mobility should be much lower than the value recommended by Lee.

5.3 Domain size dependence

Because the numerical simulations are performed in a confined domain, the viscous effect created by the non-slip wall boundary condition might influence the behaviour of the meniscus. For the bubble test conducted by Amaya-Bower and Lee (2010), it was found that the viscous effect caused by the wall boundary could constrain the radial deformation and slow down the bubble rise in a vertical channel (Amaya-Bower and Lee, 2010).

Thus, in this section, the effect of the domain size is studied through three different capillary bridge cases with a different domain size (160×80 , 240×120 and 320×160) and the capillary pressure distributions in the capillary bridge are studied to evaluate the influence of the domain size on the numerical results.

5.3.1 Numerical simulation details

Two circular bodies with the same radius $R=30.79$ are located symmetrically with respect to the axis $x=0$ (illustrated in Figure 5-11) in the domains with different sizes (160×80 , 240×120 and 320×160). The circular centres of these two bodies are $(-37.5, 0.0)$ and $(37.5, 0, 0)$, respectively. A droplet with a radius equalling 15.0, density equalling 1.0, and kinematic equalling 0.1 is initialised in the midpoint of the two circle centres with the contact angle $\theta=30^\circ$ and surface tension 7.275×10^{-5} . In order to validate the results with the analytical solutions, the gravitations are set at zero in these three cases. Besides, the meniscus radius r_1 and the capillary pressure p (mentioned in Section 4.3) are compared with each other and the analytical solution to study the effect of the domain size on the numerical results.

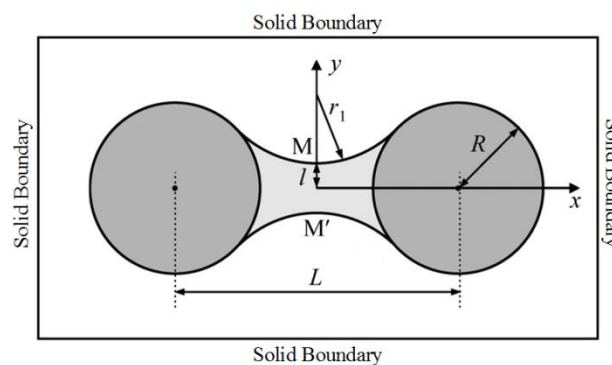
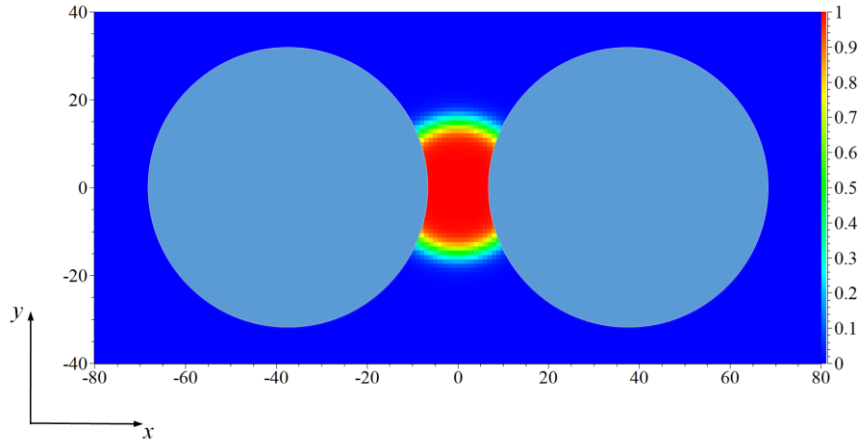


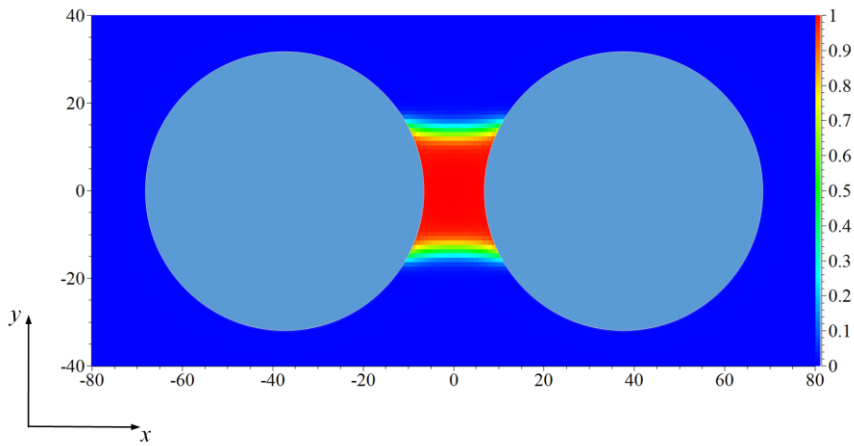
Figure 5-11 Sketch of the capillary bridge between two cylinders (Shinto et al., 2007)

5.3.2 Numerical simulation results

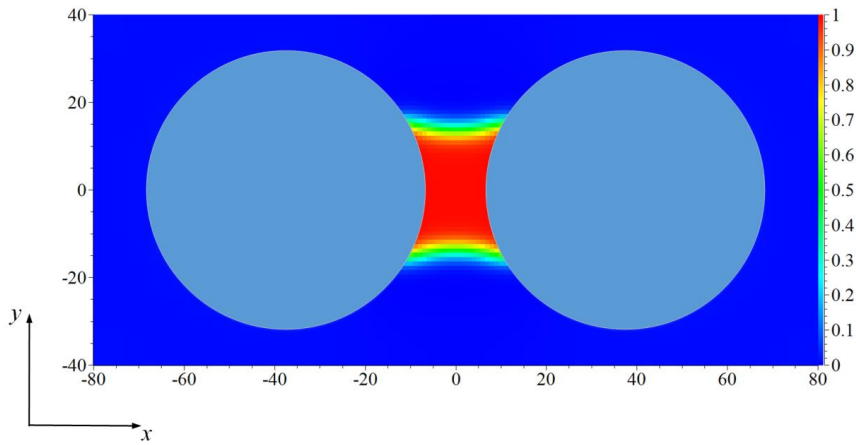
In order to ensure that the system reaches an equilibrium state, the numerical results at the 1,000,000th time steps are studied in the following. Figure 5-12, Figure 5-13 and Figure 5-14 plot the component contours for three different domain sizes in the first 1,000,000 time steps. In order to calculate the radius of the meniscus with equation (4.12), the y-coordinate values of the interface at axes $x=5$ and $x=0$ are obtained from the component distribution results in three cases. The numerical results of capillary pressure and the corresponding analytical solutions are displayed in Table 5-2.



(a) 1st time step

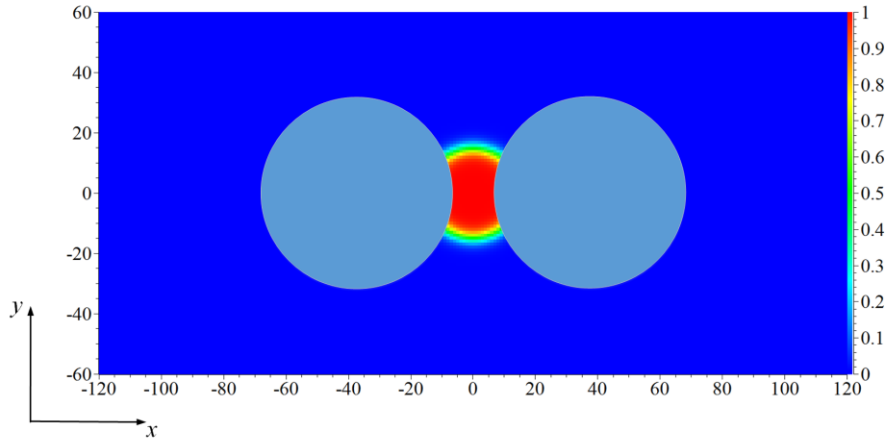


(b) 40,000th time step

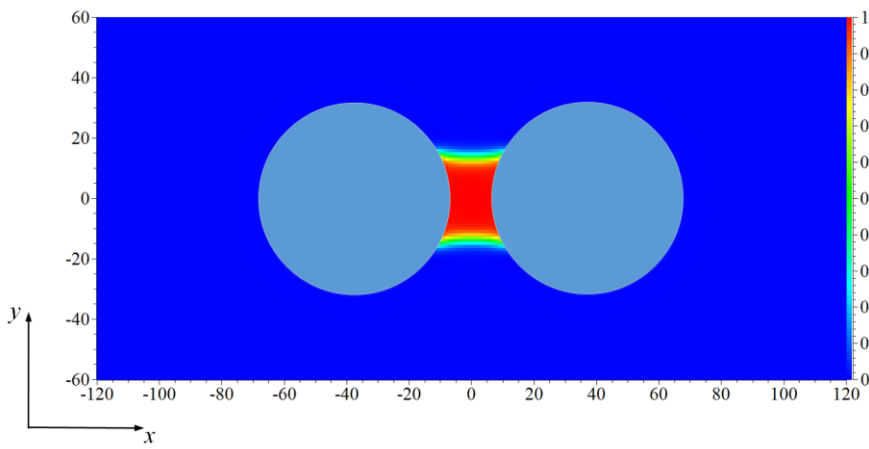


(c) 1,000,000th time step

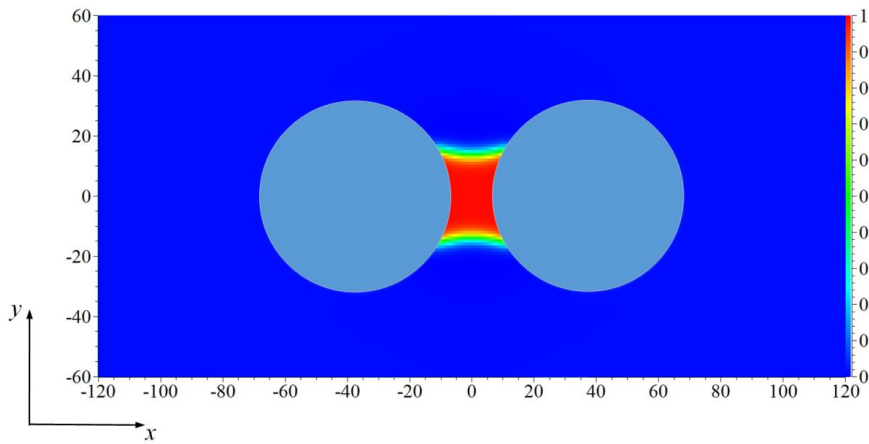
Figure 5-12 Component contour of Case 1 (domain size = 160×80)



(a) 1st time step

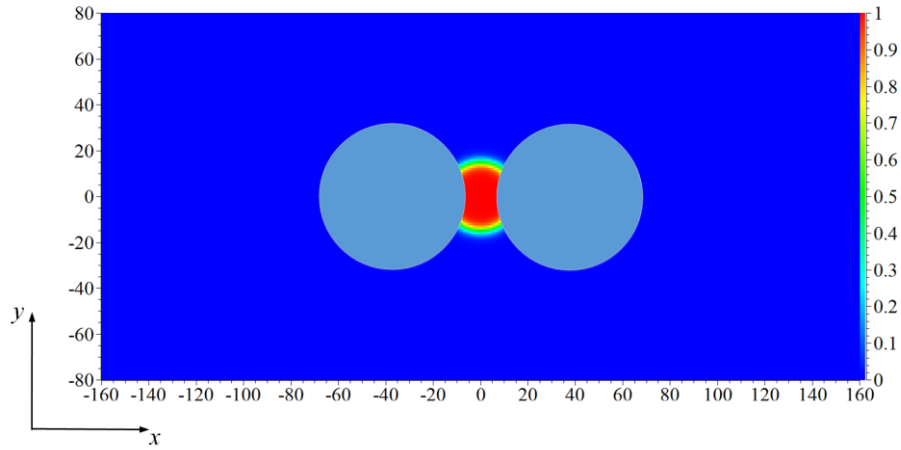


(b) 40,000th time step

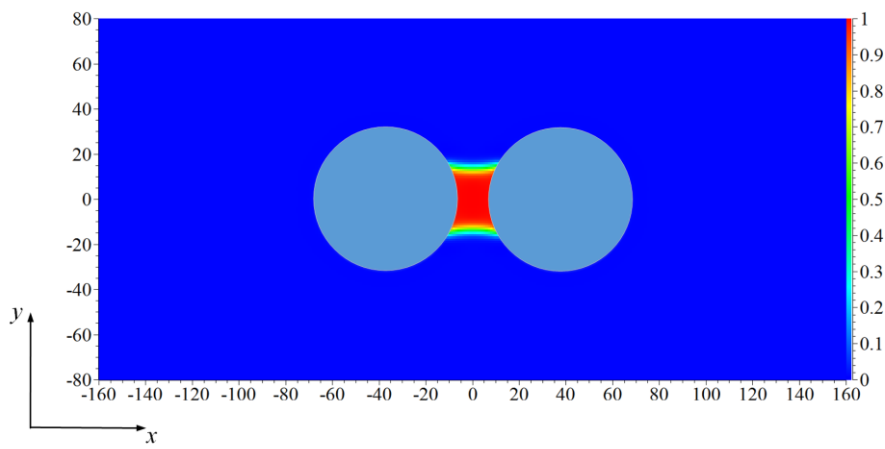


(c) 1,000,000th time step

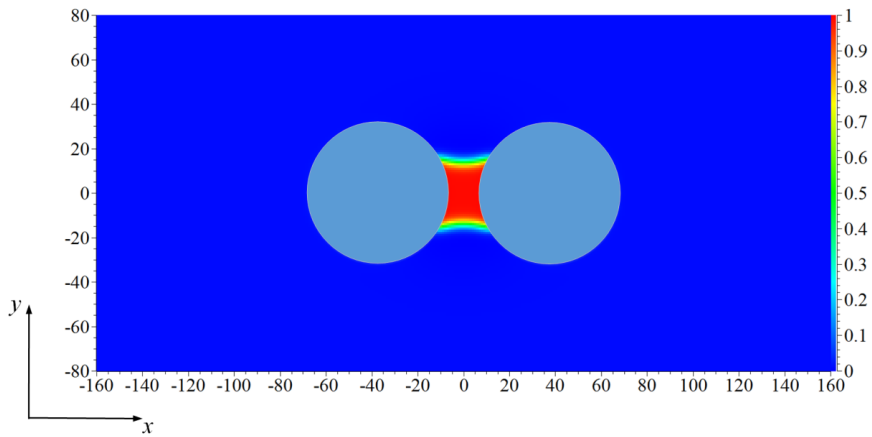
Figure 5-13 Component contour of Case 2 (domain size = 240×120)



(a) 1st time step



(b) 40,000th time step



(c) 1,000,000th time step

Figure 5-14 Component contour of Case 3 (domain size = 320×160)

Table 5-2 Numerical results of capillary pressure with different contact angles

	Case 1	Case 2	Case 3
Domain Size	160×80	240×120	320×160
Meniscus Radius R	32.3	32.3	32.3
Analytical Capillary Pressure P_A	2.252×10^{-6}	2.252×10^{-6}	2.252×10^{-6}
Numerical Capillary Pressure P_N	2.169×10^{-6}	2.169×10^{-6}	2.170×10^{-6}
Relative Error ($ P_A - P_N / P_A $)	3.7%	3.7%	3.6%

It is interesting to find in Table 5-2 that the domain size does not influence the final shape of the meniscus in these three cases and meniscus radiuses are similar in the 1,000,000th time step. Besides, the accuracy of the pressure computation also does not have significant improvement with a larger domain size (from 3.7% to 3.6%).

However, from the total pressure distributions on the cross-section MM' (illustrated in Figure 5-15, Figure 5-16 and Figure 5-17), it shows that although the capillary pressures (the pressure difference across the meniscus) are similar to each other in these three cases, the absolute values of the total pressure across the meniscus are totally different from each other.

For the domain with the smallest size, the total pressure outside the meniscus has the same order of magnitude as the capillary pressure; meanwhile, with the increase of the domain size, the outside total pressure decreases to around -1.0×10^{-7} with the domain size of 240×120, and even to -4.0×10^{-8} for the largest domain size.

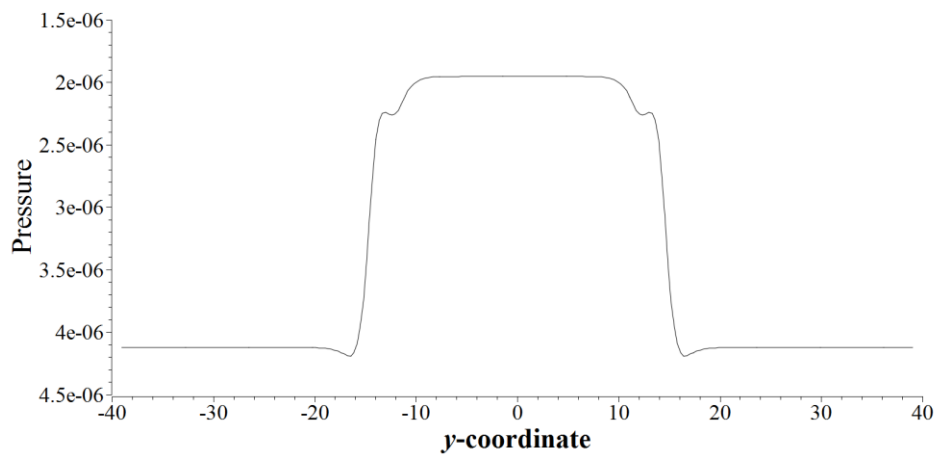


Figure 5-15 Total pressure distribution at cross-section MM' at the 1,000,000th step (domain size = 160×80)

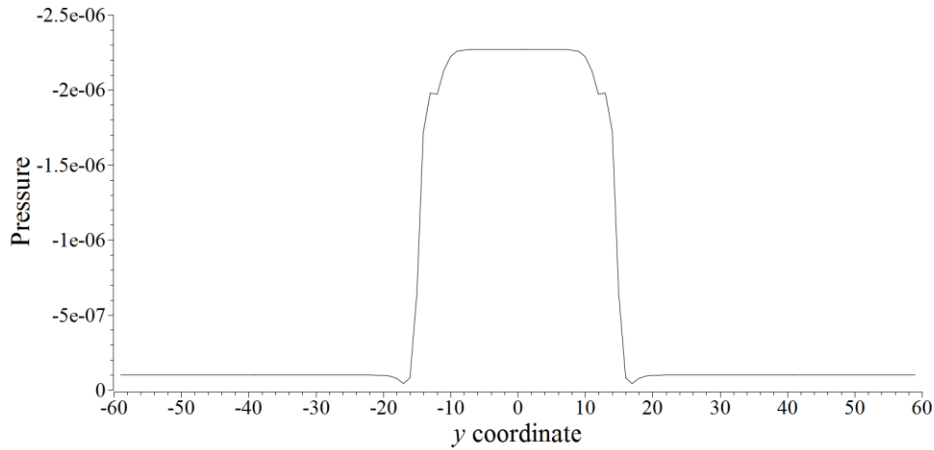


Figure 5-16 Total pressure distribution at cross-section MM' at the 1,000,000th step (domain size = 240×120)

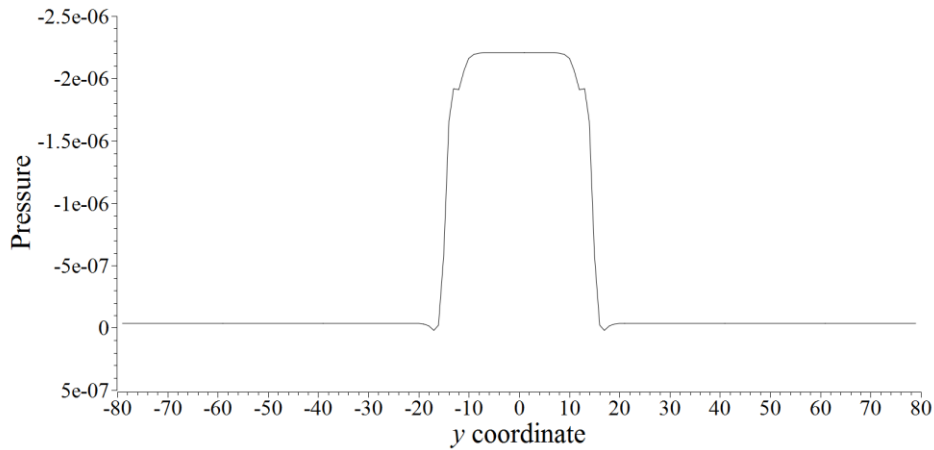


Figure 5-17 Total pressure distribution at cross-section MM' at the 1,000,000th step (domain size = 320×160)

Therefore, for the capillary bridge test in this section, the domain size has little effect on the numerical computation of the meniscus shape and the capillary pressure (the pressure difference across the meniscus); however, it affects the absolute value of the total pressure in the computation domain, especially when the domain size is small. Because the particles in the simulation are assumed to be rigid and the fluids are incompressible, the geometrical characters and the capillary pressure difference stay the same with the different domain size. Nevertheless, if the particles are soft and movable or the compressibility of the fluids is taken into consideration, the smallest domain size might cause a severe error in the numerical simulation.

5.4 Grid resolution dependence

In order to study the effect of grid resolution on the numerical computation, in this section, the capillary bridge test with three different grid resolutions (120×60 , 240×120 and 360×180) is simulated and the capillary pressure distributions in the capillary bridge are studied to evaluate the influence of grid resolution on the numerical result.

5.4.1 Numerical simulation details

The domain size for the capillary bridge test in this section is $2.4\text{mm} \times 1.2\text{mm}$ and the densities for the liquid and vapour phases are $1.0 \times 10^3\text{ kg/m}^3$ and $1.0 \times 10^3\text{ kg/m}^3$, respectively. The corresponding kinematic viscosities are $1.0 \times 10^{-5}\text{ m}^2/\text{s}$ and $1.57 \times 10^{-5}\text{ m}^2/\text{s}$.

As illustrated in Figure 5-18, two circular bodies with the radius $R=0.3079\text{ mm}$ are located with respect to the axis $x=0$. A droplet with a 0.15mm radius is initialised in the midpoint of the two circle centres with the same contact angle $\theta=30^\circ$ and surface tension $7.275 \times 10^{-5}\text{ N/m}$.

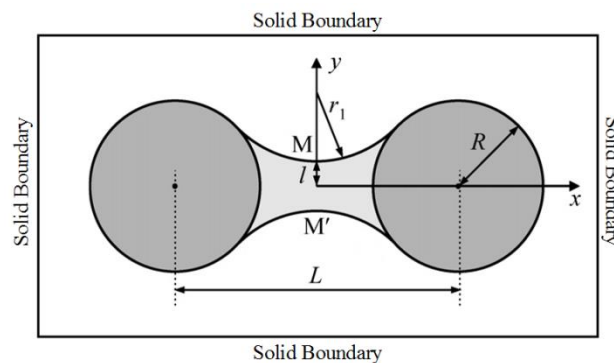


Figure 5-18 Sketch of the capillary bridge between two cylinders (Shinto et al., 2007)

According to Appendix A with a different grid resolution, the same physical units would have different lattice units in the numerical simulation. The parameters in the LB model with different grid resolutions are listed in Table 5-3 (all parameters are in lattice units except for the space length and the time step).

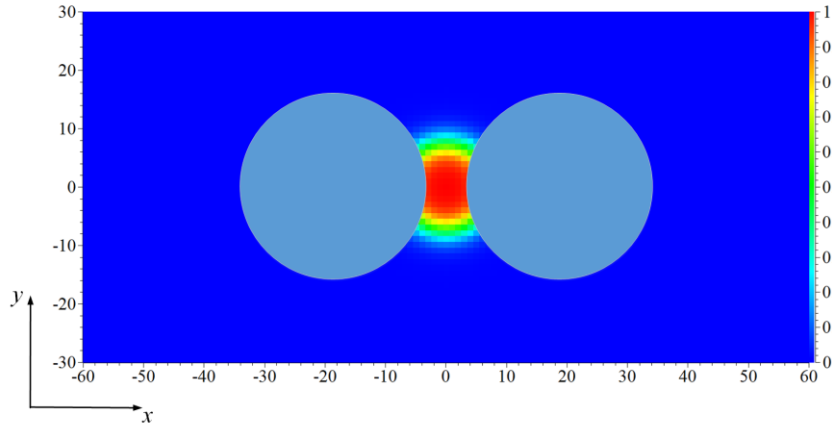
Table 5-3 Parameters used in three different cases

	Case 1	Case 2	Case 3
Grid resolution	120×60	240×120	360×180
Space length (m)	2.0×10^{-5}	1.0×10^{-5}	6.67×10^{-6}
Time step (s)	2.0e-6	1.0×10^{-6}	2.67×10^{-7}
Liquid density	1.0	1.0	1.0
Vapour density	1.0×10^{-3}	1.0×10^{-3}	1.0×10^{-3}
Circle radius	15.40	30.79	46.19
Droplet radius	7.5	15.0	22.5
Circle centre distance	37.5	75.0	112.5
Kinematic viscosity/liquid	5.00×10^{-2}	1.00×10^{-1}	6.00×10^{-2}
Kinematic viscosity/vapour	7.85×10^{-2}	1.57×10^{-1}	9.42×10^{-2}
Surface tension	3.638×10^{-5}	7.275×10^{-5}	1.746×10^{-5}

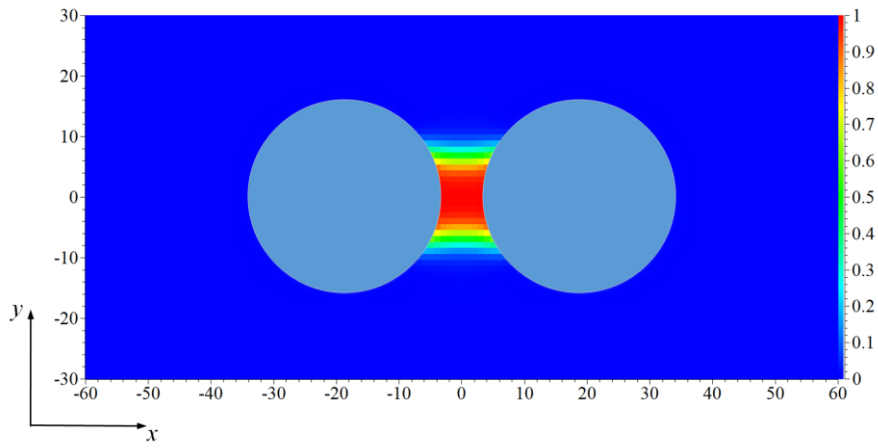
It should be mentioned that in the simulation of the capillary bridge test with a different grid resolution, the time step should be adjusted to guarantee the liquid kinematic viscosity lower than 0.2 for the requirement of stable computation in this section, which might be related to the distortion incurred for the initial shear stress mentioned in Section 5.2.2.

5.4.2 Numerical simulation results

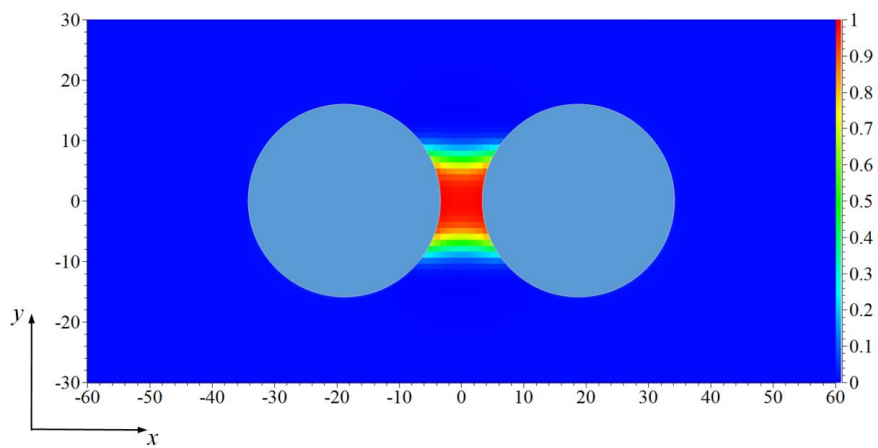
In order to ensure that the system reaches an equilibrium state, the numerical results at 1 second (1,000,000 time steps for the grid resolution of 240×120) are studied in the following. In order to calculate the radius of the meniscus with equation (4.12), the y-coordinate values of the interface at axes $x=3$ and $x=0$ are obtained from the component distribution results in three cases. The numerical results of capillary pressure and the corresponding analytical solutions are displayed in Table 5-4.



(a) 1st time step

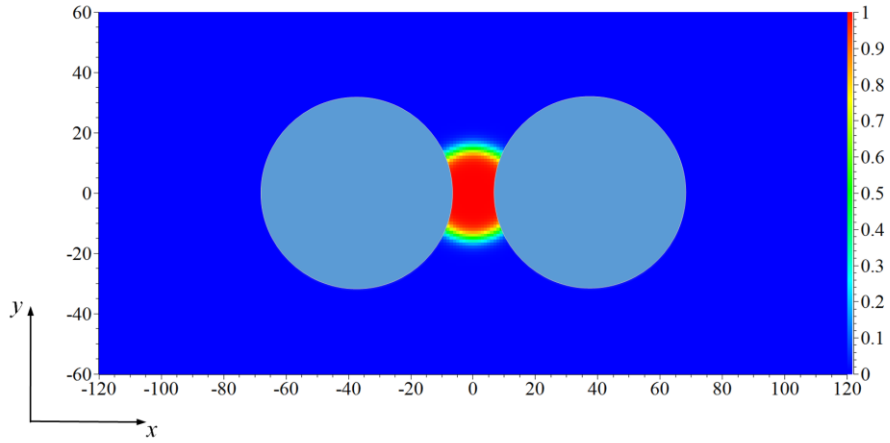


(b) 20,000th time step

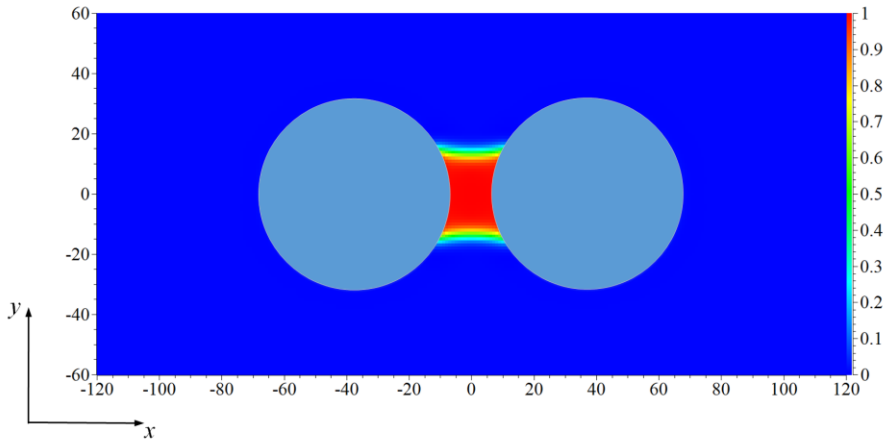


(c) 500,000th time step

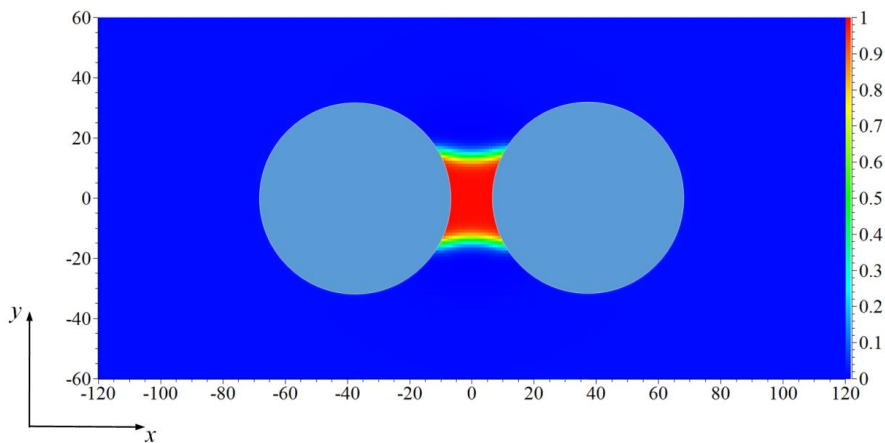
Figure 5-19 Component contour of Case 1 (grid resolution = 120×60)



(a) 1st time step

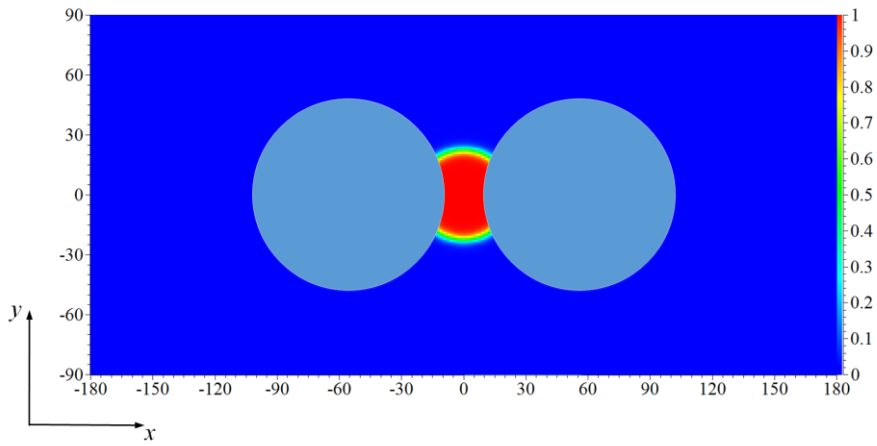


(b) 40,000th time step

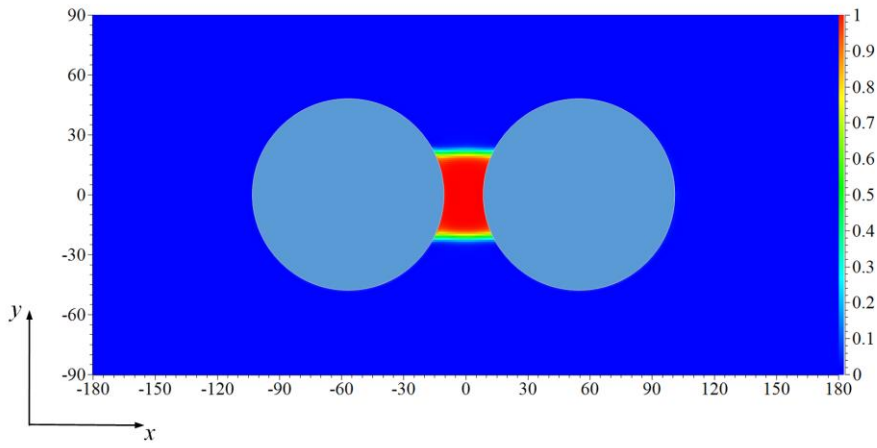


(c) 1,000,000th time step

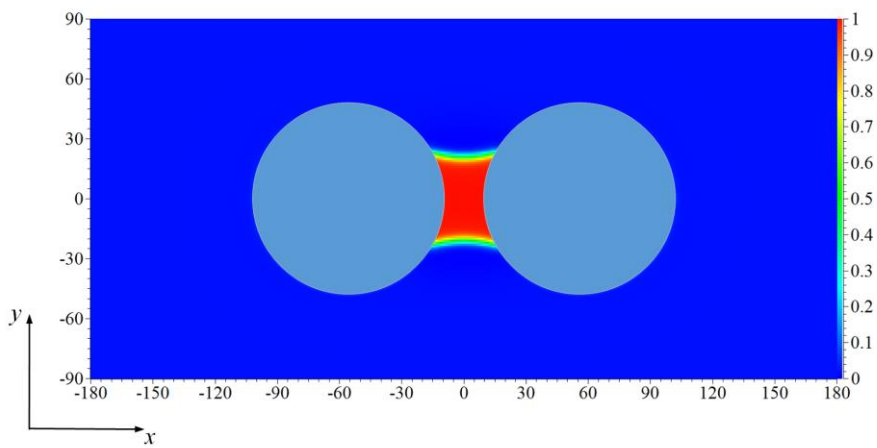
Figure 5-20 Component contour of Case 2 (grid resolution = 240×120)



(a) 1st time step



(b) 80,000th time step



(c) 3,750,000th time step

Figure 5-21 Component contour of Case 3 (grid resolution = 360×180)

Table 5-4 Numerical results of capillary pressure with different contact angles

	Case 1	Case 2	Case 3
Grid Resolution	120×60	240×120	360×180
Time Step (lattice unit)	500,000	1,000,000	3,750,000
Time Step (physical unit/s)	1.0	1.0	1.0
Meniscus Radius R (lattice unit)	15.9	32.3	51.5
Meniscus Radius R (physical unit/m)	3.18×10^{-4}	3.23×10^{-4}	3.43×10^{-4}
Surface Tension	3.638×10^{-5}	7.275×10^{-5}	1.746×10^{-5}
Analytical Capillary Pressure P_A	2.288×10^{-6}	2.252×10^{-6}	3.390×10^{-7}
Numerical Capillary Pressure P_N	2.236×10^{-6}	2.169×10^{-6}	3.244×10^{-7}
Relative Error ($ P_A - P_N / P_A $)	2.3%	3.7%	4.3%

In Table 5-4, it shows that with the increase in the grid resolution, the meniscus radius is also increasing in physical units. The relative variation of the meniscus radius with a different grid resolution is smaller than 10%; however, the CPU time for the models soars from 35 hours in Case 1 to nearly 1,900 hours in Case 3.

Besides, the relative errors of the predicted pressure (illustrated in Table 5-4) do not change much, just from 2.3% to 4.3%, and the corresponding numerical capillary pressure distributions on the cross-section MM' are plotted in Figure 5-22 to Figure 5-24. Compared with the large increase in the computational requirements, the variation of the radius and the pressure can be ignored.

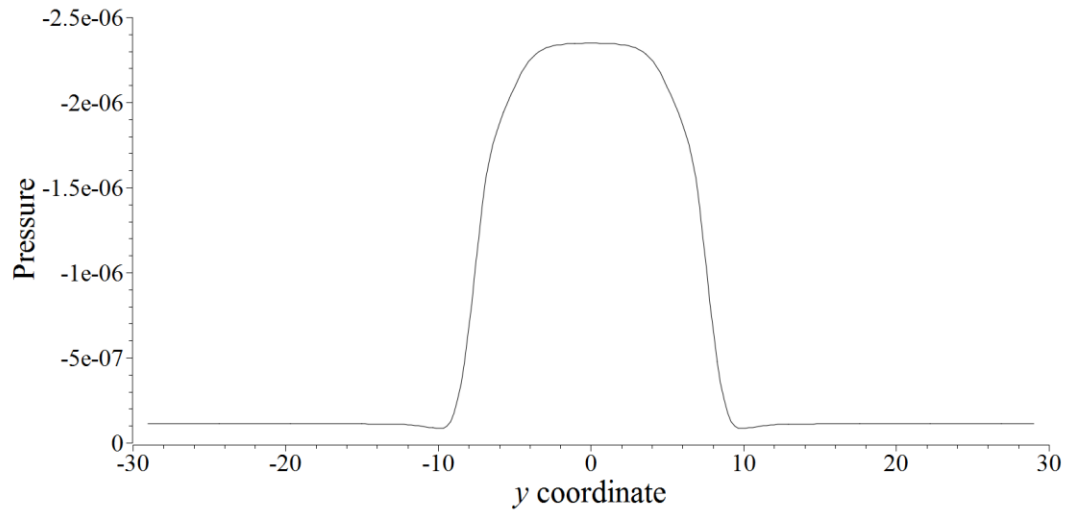


Figure 5-22 Total pressure distribution at cross-section MM ' at the 500,000th step
(domain size = 120×60)

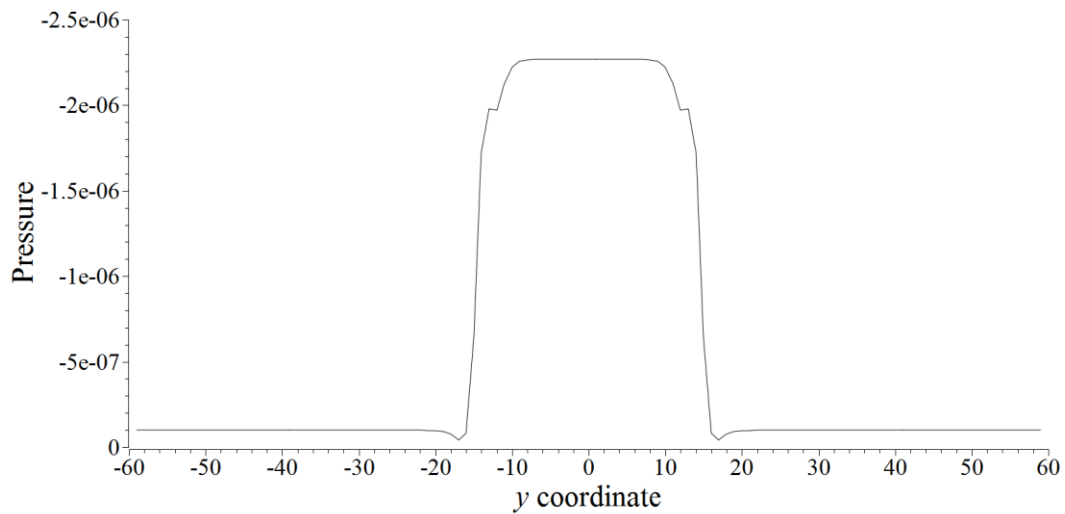


Figure 5-23 Total pressure distribution at cross-section MM ' at the 1,000,000th step
(domain size = 240×120)

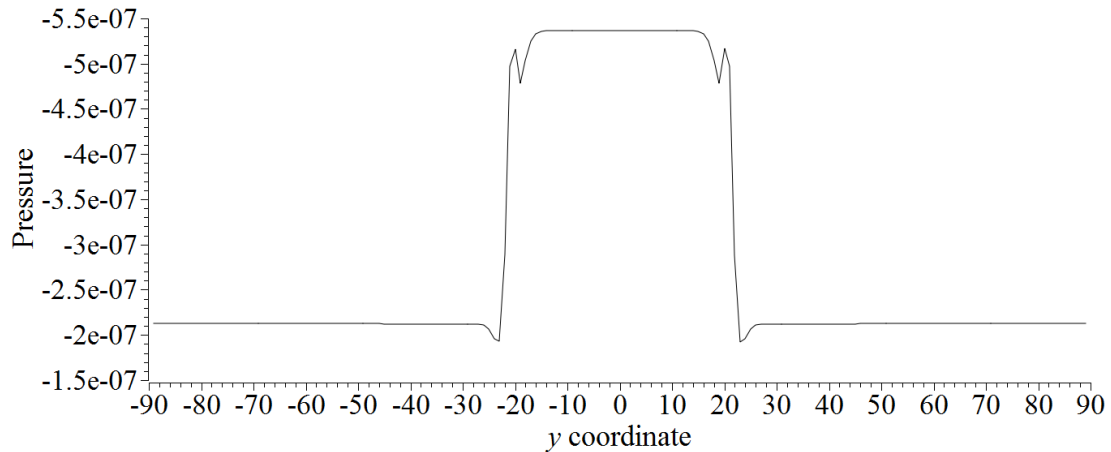


Figure 5-24 Total pressure distribution at cross-section MM' at the 1,000,000th step
(domain size = 320×160)

Therefore, for the simple capillary bridge test in this section, the grid resolution has little effect on the numerical computation of the meniscus shape and the capillary pressure (the pressure difference across the meniscus). However, with the increase in the grid resolution, the CPU time would increase dramatically.

5.5 Summary

This chapter explores the effects of four different parameters, including the interface thickness, the mobility, the domain size and the grid resolution, on the numerical simulation.

The interface thickness S in the LB model contributes to the smoothness of the physical quantity gradients across the meniscus without changing the total pressure acted on it. Although the larger S is beneficial for the computational stability in the model, it will also exaggerate the contact length between the meniscus and the solid particle, which might damage the accuracy of the numerical results.

Higher mobility M means a faster convergence to the equilibrium state for the model (Lee, 2009). However, large mobility (i.e. the case $M=5.0$ in Section 5.2) will also lead to the instability of the numerical computation.

For the capillary bridge test validated in this chapter, the domain size has little effect on the geometrical characters and the capillary pressure difference for the meniscus at the equilibrium state. Nevertheless, the absolute value of the total pressure is obviously higher in the smallest domain size, which might produce errors when the

particles in the model are soft and movable or the fluids are compressible in the simulation.

The grid resolution shows little effect on the geometrical characters and the capillary pressure difference for the meniscus at the equilibrium state. In fact, Amaya-Bower and Lee (2010) also found that the final shape in the coarse grid only had a slight difference from that in the fine grid for the bubble rising test. Yet, for some cases, the finer grid could illustrate the details of the fluid movement specifically.

Chapter 6 Conclusions and Future Work

6.1 Conclusions of this thesis

In this thesis, a numerical Lattice Boltzmann and Ghost Fluid Immersed Boundary (LB-GFIB) code is developed in exploring the interaction between two different fluids with large density ratio and capturing the local dynamic contacting behaviour between the meniscus and the curved solid boundaries. Besides, a new forcing calculation approach is presented in this thesis to predict the mechanical behaviour of the meniscus on the curved boundaries.

In order to verify the new code developed in this thesis, the droplet test, the capillary rise test, the capillary bridge test, the dynamic test and the capillary rise in porous media test are conducted to validate the numerical results. Besides, the parameter studies are conducted to gauge the influence of four parameters in the model, including the interface thickness, the mobility, the domain size and the grid resolution.

The detailed finds in this thesis are as follows,

- The no-slip bounce back boundary condition applied in the conventional GFIB models fail to conserve the mass in the numerical computation, while the slip bounce back boundary condition can help to eliminate the violation of mass conservation in the model.
- The multiphase Lattice Boltzmann model applied in this thesis can reduce the negative influence of parasite numerical currents in the simulation and ensure the stability of the liquid droplet among the vapour with density ratio about 1000:1 in the droplet test with only 1.3% shrinkage of the radius compared with the original value.
- The modified GFIB model exerted on the solid boundaries in this thesis can guarantee the mass conservation in the capillary rise test, the capillary bridge test and the dynamic line contact test. Besides, the capillary rises and the contact angles in the simulation are all well satisfied with the analytical values with a maximum error at 9.0%.

- The newly proposed forcing calculation method produces can accurately predict the capillary force between the two circular particles in the capillary bridge test and the contact dynamic line test in this thesis with a relative error less than 5.0% compared to the analytical solutions.
- The new code can simulate the complex Two-Phase Flow in the complex geometrical porous media model with good prediction of pressure inside the porous media (with a 12.7% error with the analytical result), though the capillary rise rate still cannot be simulated accurately in this thesis due to the small amount of solid particles used in the model.
- The parametrical study shows that except the interface thickness, the mobility, the domain size and the grid resolution have little impacts on the accuracy of the results. For the interface thickness, although it contributes to the numerical stability, it also exaggerates the thickness of meniscus in the real physical problems and damage numerical accuracy.

The equilibrium time in the computation is mainly influenced by the mobility and the grid resolution in the parametrical study in this thesis. With smaller mobility and high grid resolution, the CPU time required for the same model would increase obviously.

6.2 Future works

The research presented in this thesis is an early attempt to develop a numerical tool to study the behaviour of unsaturated soils. The future work related to the thesis could include:

(1) Combining the code with Discrete Element Method (DEM)

In this thesis, the circular particles are assumed to be stagnant in the simulation, which is different with multiphase fluids flows in unsaturated soil skeleton in reality. In fact, the coupling effect between the fluids flow and the movement of the soil particles is a critical point in the numerical study of unsaturated soil behaviour. In this thesis, the LB code only solve the problem of the multiphase fluids flow along the curved boundary, the simulation of the real water-air fluids flow in soil skeletons might be solved by the coupled LBM with DEM.

The Discrete Element Method (DEM) is originally developed by Cundall (Cundall and Strack, 1978) for the problems in rock mechanics and later it becomes a powerful

tool to simulate the discrete objectives systems, including the granular soil particles (Chen et al, 2011). The coupled LB and DEM method was first proposed by Cook et al (2000) in 2000 and later Boutt et al (2007) succeeded in simulating the fluid flow in the 2D porous media with this method.

The code *FPS-BHAM* used in this thesis developed by Li in 2013 has already been validated against the pipe leakage experiment and the good quantity agreements show that the subroutines related to the LB and DEM is well developed in the code.

Therefore, the subroutines related to the LB-DEM interaction will be modified in the future and the coupled multiphase LB with DEM will be developed to simulate the Two-Phase Flow in unsaturated soil particles in two dimensions.

(2) Extending the code to three-dimensions

In the current two-dimensional simulations, the solid particles needs to have a certain distance with each other to ensure that the multiphase fluids flow can pass through the assembly particles, while in the real condition, the liquid can easily flow in the connected pores with particles contacted closely with each other in three dimensions. Besides, the meniscus shape and force analysis in two-dimensions are different with those in the real three-dimensions (as indicated in section 4.2.1). Therefore, it is expected to extend the simulations by the modified *FPS-BHAM* to three-dimensions ones, by which physical characteristics can be captured more accurately.

References

- Akinci, N., Akinci, G. & Teschner, M. (2013) Versatile surface tension and adhesion for SPH fluids. *ACM Transactions on Graphics (TOG)* 32(6). p. 182-189
- Allain, C. & Cloitre, M. (1993) Interaction between particles trapped at fluid interfaces. I. Exact and asymptotic solutions for the force between two horizontal cylinders. *Journal of Colloid Interface Science* 157. p. 261-268
- Amaya-Bower, L. & Lee, T. (2011) Numerical simulation of single bubble rising in vertical and inclined square channel using lattice Boltzmann method. *Chemical Engineering Science* 66(5). p. 935-952
- Anderson, D. M., McFadden, G. B. & Wheeler, A. A. (1998) Diffuse-interface methods in fluid mechanics. *Annual Review of Fluid Mechanics* 30(1). p.139-165
- Anderson, T. B. & Jackson, R. (1968) Fluid Mechanical Description of Fluidized Beds. Stability of State of Uniform Fluidization. *Industrial & Engineering Chemistry Fundamentals* 7(1). p. 12-21
- Apsley, D. & Hu, W. (2003) CFD simulation of two- and three-dimensional free-surface flow. *International Journal for Numerical Methods in Fluids* 42(5). p. 465-491
- Benzi, R., Succi, S & Vergassola, M. (1992) The lattice Boltzmann equation: theory and applications. *Physics Reports* 222(3). p. 145-197.
- Capuani, F., Pagonabarraga, I. & Frenkel, D. (2004) Discrete solution of the electrokinetic equations. *The Journal of chemical physics* 121(2). p. 973-986.
- Chaudhuri, A. , Hadjadj, A. & Chinnayya, A. (2011) On the use of immersed boundary methods for shock/obstacle interactions. *Journal of Computational Physics* 230(5). p. 1731-1748
- Chen, F., Drumm, E. C. & Guiochon, G. (2011) Coupled discrete element and finite volume solution of two classical soil mechanics problems. *Computers and Geotechnics* 38(5). p. 638-647
- Chen, S. & Doolen, G. D. (1998) Lattice Boltzmann Method for Fluid Flows, *Annual Review of Fluid Mechanics* 30(1). p. 329-364

- Chen, S., Chen, H., Martinez, D. & Matthaeus, W. (1991) Lattice Boltzmann model for simulation of magnetohydrodynamics. *Physical Review Letters* 67(27). p. 3776-3779.
- Choi, K. Y. & Cheung, R. W. M. (2013) Landslide disaster prevention and mitigation through works in Hong Kong . *Journal of Rock Mechanics and Geotechnical Engineering* 5(5). p. 354-365
- Coleman, G. N. & Sandberg, R. D. (2010) A primer on direct numerical simulation of turbulence-methods, procedures and guidelines. [Online] May 2009. Available from: <http://eprints.soton.ac.uk/66182/> . [Accessed: 14th April 2015]
- Connington, K. & Lee, T. (2012) A review of spurious currents in the lattice Boltzmann method for multiphase flows. *Journal of Mechanical Science and Technology* 26(12). p. 3857-3863
- Connington, K. & Lee, T. (2013) Lattice Boltzmann simulations of forced wetting transitions of drops on superhydrophobic surfaces. *Journal of Computational Physics* 250. p. 601-615
- Connington, K. W., Lee, T. & Morris, J. F. (2015) Interaction of fluid interfaces with immersed solid particles using the lattice Boltzmann method for liquid–gas–particle systems. *Journal of Computational Physics* 283. p. 453-477
- Crespo, A. J. C. (2008) Application of the smoothed particle hydrodynamics model SPHysics to free surface hydrodynamics. A Thesis Submitted in partial fulfilment of the Requirements of Universidade de Vigo for the Degree of Doctor of Philosophy. Vigo: Universidade de Vigo
- Cundall, P. A. & Strack, O. D. (1978) The distinct element method as a tool for research in granular media. Report to the national science foundation concerning NSF grant eng76-20711.
- Daniele, C. (2009) Numerical analysis of multiphase flows through the lattice boltzmann method. PhD Thesis, University of Rome TOR VERGATA, Rome
- Daniele, C., Gino, B., Sauro, S., Federico, T. & Stefano, U. (2009) Improved Lattice Boltzmann Without Parasitic Currents for Rayleigh-Taylor Instability. *Communications in Computational Physical* 7(3). p. 423-444

- Delker, T., Pengra, D. B. & Wong, P. (1996) Interface Pinning and the Dynamics of Capillary Rise in Porous Media. *Physical Review Letters* 76(16). p. 2902-2905
- Ding, H., Spelt, P.D.M. & Shu, C. (2007) Diffuse interface model for incompressible two-phase flows with large density ratios. *Journal of Computational Physics* 226(2). p. 2078–2095
- Dissipative particle dynamics, May 05, 2015, Available from <
https://en.wikipedia.org/wiki/Dissipative_particle_dynamics >
- Fan, L., Fang, H. & Lin, Z. (2001) Simulation of contact line dynamics in a two-dimensional capillary tube by the lattice Boltzmann model. *Physical Review E* 63(5). p. 051603
- Feng, Y. T., Han, K. & Owen, D. R. J. (2007) Coupled lattice Boltzmann method and discrete element modelling of particle transport in turbulent fluid flows: Computational issues. *International Journal for Numerical Methods in Engineering* 72(9). p. 1111-1134
- Feng, Z. G. & Michaelides, E. E. (2004) The immersed boundary-lattice Boltzmann method for solving fluid–particles interaction problems. *Journal of Computational Physics* 195(2). p. 602-628
- Filippova, O. & Hänel, D. (2000) A Novel Lattice BGK Approach for Low Mach Number Combustion. *Journal of Computational Physics* 158(2). p. 139-160
- Fredlund, D. G. (1997) From theory to the practice of unsaturated soil mechanics. *Proceeding of the Third Brazilian Symposium on Unsaturated Soil 2*. p. 501-526
- Fredlund, D. G., & Xing, A. (1994) Equations for the soil-water characteristic curve. *Canadian Geotechnical Journal* 31(4). p. 521-532
- Fredlund, D. G., Rahardjo, H. & Fredlund, M. D. (2012) *Unsaturated soil mechanics in engineering practice*, Hoboken: John Wiley & Sons
- Fredlund, M. D. (2000) *The role of unsaturated soil property functions in the practice of unsaturated soil mechanics*. PhD Thesis, University of Saskatchewan, Saskatoon

- Fredlund, M.D., Fredlund, D. G. & Wilson, G. W. (1997) Estimation of unsaturated soil properties using a knowledge-based system. Proceedings of the Fourth Congress on Computing in Civil Engineering, ASCE, Philadelphia, p. 16-18
- Fries, N. & Dreyer, M. (2008) An analytic solution of capillary rise restrained by gravity. *Journal of Colloid and Interface Science* 320. p. 259-263
- Galera, S. , Maire, P. H. & Breil, J. (2010) A two-dimensional unstructured cell-centered multi-material ALE scheme using VOF interface reconstruction, *Journal of Computational Physics* 229(16). p. 5755-5787
- Garcia, M., Sommerer, Y., Schonfeld, T. & Poinso, T. (2005) Evaluation of euler/euler and euler/lagrange strategies for large eddy simulations of turbulent reacting flows In ECCOMAS Thematic Conference on Computational Combustion, Greece
- Gens, A. (2010) Soil–environment interactions in geotechnical engineering. *Géotechnique* 60(1). p. 3-74
- Glimm, J., Grove, J. W., Li, X. L., Oh, W. & Sharp, D. H. (2001) A Critical Analysis of Rayleigh–Taylor Growth Rates. *Journal of Computational Physics* 169(2). p. 652-677
- Gomez,G. M., Roger, B. D., Dalrymple, R. A. & Crespo, A. J. C.(2010) State-of-the-art of classical SPH for free-surface flows. *Journal of Hydraulic Research* 48(S1). p. 6-27
- Gomez-Gesteira, M., Rogers, B. D., Dalrymple, R. A. & Crespo, A.J.C. (2010) State-of-the-art of classical SPH for free-surface flows. *Journal of Hydraulic Research* 48. p. 6-27
- Gunstensen,A. K., Rothman, D. H., Zaleski, S. & Zanetti, G. (1991) Lattice Boltzmann model of immiscible fluids. *Physical Review A* 43(8). p. 4320-4327
- Guo, Z., Zheng, C. & Shi, B. (2002) An extrapolation method for boundary conditions in lattice Boltzmann method. *Physics of Fluids* 14(6). p. 2007-2010
- Hao, L. & Cheng, P. (2010) Pore-scale simulations on relative permeability of porous media by lattice Boltzmann method. *International Journal of Heat and Mass Transfer* 53. p. 1908-1913

- He, X. & Doolen, G. D. (2002) Thermodynamic Foundations of Kinetic Theory and Lattice Boltzmann Models for Multiphase Flows. *Journal of Statistical Physics* 107(1). p. 309-328
- He, X., Chen, S. & Zhang, R. (1999) A lattice Boltzmann scheme for incompressible multiphase flow and its application in simulation of Rayleigh-Taylor instability. *Journal of Computational Physics* 152. p. 642-663
- He, X., Shan, X. & Doolen G. D. (1998) Discrete Boltzmann equation model for nonideal gases. *Physical Review E* 57(1). p. R13-R16
- Hu, X. Y. & Adams, N. A. (2006) A multi-phase SPH method for macroscopic and mesoscopic flows. *Journal of Computational Physics* 213(2). p. 844-861
- Huang, H., Thorne, D. T., Schaap, M. G. & Sukop, M. C. (2007) Proposed approximation for contact angles in Shan-and-Chen-type multicomponent multiphase lattice Boltzmann models. *Physical Review E* 76(6). p. 066701
- Jones, L. D. & Jefferson, I. (2012) Expansive Soil. in Burland, J., (ed.) *ICE manual of geotechnical engineering. Volume 1, geotechnical engineering principles, problematic soils and site investigation*, London: ICE Publishing, (p. 413-441)
- Kralchevsky, P. A. & Nagayama, K. (2001) *Particles at Fluid Interfaces and Membranes*. Elsevier, Amsterdam
- KU Leuven (2015) Microstructure Modeling. [Online] available from: <https://www.mtm.kuleuven.be/Onderzoek/thermo/research-fields/microstructure-modeling> [Accessed : 14th April 2015]
- Kuksenok, O., Yeomans, J.M. & Balazs, A. C. (2002) Using patterned substrates to promote mixing in microchannels. *Physical Review E* 65(3). p. 031502
- Kuznik, F., Obrecht, C., Rusaouen, G. & Roux, J. J. (2010) LBM based flow simulation using GPU computing processor. *Computers & Mathematics with Applications* 59(7). p. 2380-2392
- Ladd, A. J. C. (1994a) Numerical simulations of particulate suspensions via a discretized Boltzmann equation. Part 1. Theoretical foundation. *Journal of Fluid Mechanics* 271. p.285-309

Ladd, A. J. C. (1994b) Numerical simulations of particulate suspensions via a discretized Boltzmann equation. Part 2. Numerical results. *Journal of Fluid Mechanics* 271. p. 311-339.

Lago, M. & Araujo, M. (2001) Capillary Rise in Porous Media. *Journal of Colloid and Interface Science* 234. p. 35-43

Lagrangian and Eulerian specification of the flow field, (wiki article), September 15, 2015, Available from: <
https://en.wikipedia.org/wiki/Lagrangian_and_Eulerian_specification_of_the_flow_field>

Lee, S. H., Hur, N. & Kang, S. (2011) A numerical analysis of drop impact on liquid film by using a level set method. *Journal of Mechanical Science and Technology* 25(10) .p. 2567-2572

Lee, T. (2004) A lattice Boltzmann study of surface-directed immiscible two-fluid flows in microfluidic systems. A thesis submitted in partial fulfillment of the requirements for the Doctor of Philosophy degree in Mechanical Engineering in the Graduate College of the University of Iowa. Iowa City: University of Iowa

Lee, T. (2009) Effects of incompressibility on the elimination of parasitic currents in the lattice Boltzmann equation method for binary fluids. *Computers & Mathematics with Applications* 58(5). p.987-994

Lee, T. & Fischer, P. F. (2006) Eliminating parasitic currents in the lattice Boltzmann equation method for nonideal gases. *Physical Review E* 74(4). p. 046709

Lee, T. & Lin, C. L. (2003) Pressure evolution lattice-Boltzmann-equation method for two-phase flow with phase change. *Physical Review E* 67. p. 056703

Lee, T. & Lin, C. L. (2005a) A stable discretization of the lattice Boltzmann equation for simulation of incompressible two-phase flows at high density ratio. *Journal of Computational Physics* 206(1). p. 16-47

Lee, T. & Lin, C. L. (2005b) Rarefaction and compressibility effects of the lattice-Boltzmann-equation method in a gas microchannel. *Physical Review E* 71(4). p. 046706

Lee, T. & Liu, L. (2008) Wall boundary conditions in the lattice Boltzmann equation method for nonideal gases. *Physical Review E* 78. p. 017702

Lee, T. & Liu, L. (2010) Lattice Boltzmann simulations of micron-scale drop impact on dry surfaces. *Journal of Computational Physics* 229(20). p. 8045-8063

Li, J. (2013) Numerical investigations of the coupled DEM-LBM technique with application to leakage-soil interaction due to a leaking pipe. A thesis submitted to The University of Birmingham for the degree of Doctor of Philosophy. Birmingham: University of Birmingham

Liu, L. & Lee, T. (2009) Wall free energy based polynomial boundary conditions for non-ideal gas lattice Boltzmann equation. *International Journal of Modern Physics C* 20(11). p. 1749-1768

Liu, M. B. & Liu, G. R. (2010) Smoothed Particle Hydrodynamics (SPH): an Overview and Recent Developments. *Archives of Computational Methods in Engineering* 17(1). p. 25-76

Lockington, D. A. & Parlange, J. Y. (2004) A new equation for macroscopic description of capillary rise in porous media. *Journal of Colloid and Interface Science* 278. p. 404-409

Lu, N. & Likos, J. L. (2004) *Unsaturated Soil Mechanics*, Hoboken: John Wiley & Sons, Inc.

Mass diffusivity, (wiki article), July 31, 2015, Available from: <
https://en.wikipedia.org/wiki/Mass_diffusivity >

McKee, C. R., & Bumb, A. C. (1984) The importance of unsaturated flow parameters in designing a monitoring system for hazardous wastes and environmental emergencies. In *Proceedings of the Hazardous Materials Control Research Institute National Conference*, Houston, Texas. p. 50-58

McKee, C. R., & Bumb, A. C. (1987) Flow-testing coalbed methane production wells in the presence of water and gas. *Society of Petroleum Engineers Formation Evaluation* 2(4). p. 599-608

- Meakin, P. & Tartakovsky, A. M. (2009) Modeling and simulation of pore-scale multiphase fluid flow and reactive transport in fractured and porous media. *Reviews of Geophysics* 47(3). p. RG3002
- Menard, T., Tanguy, S. & Berlemont, A. (2007) Coupling level set/VOF/ghost fluid methods: Validation and application to 3D simulation of the primary break-up of a liquid jet. *International Journal of Multiphase Flow* 33(5). p. 510-524
- Microstructure Modelling, 2015, Available from <
<http://www.mtm.kuleuven.be/Onderzoek/thermo/research-fields/microstructure-modeling> >
- Monaghan, J. J. (1994) Simulating Free Surface Flows with SPH. *Journal of Computational Physics* 110(2). p. 399-406
- Morris, J. P. (2000) Simulating surface tension with smoothed particle hydrodynamics. *International Journal for Numerical Methods in Fluids* 33(3). p. 333-353
- Mukherjee, S. & Abraham, J. (2007) Investigations of drop impact on dry walls with a lattice-Boltzmann model. *Journal of Colloid and Interface Science* 312(2). p. 341-354
- Niu, X. D., Shu, C., Chew, Y. T. & Peng, Y. (2006) A momentum exchange-based immersed boundary-lattice Boltzmann method for simulating incompressible viscous flows. *Physics Letters A* 354(3). p. 173-182
- Noble, D. & Torczynski, J. (1998) A lattice Boltzmann method for partially saturated cells. *Journal of Modern Physics C* 9. p. 1189-1201
- Oertel, Herbert, P. Erhard, Katherine Asfaw, Dieter Etling, U. Muller, U. Riedel, K. R. Sreenivasan, & J. Warnatz. (2010) *Prandtl-essentials of fluid mechanics*. New York: Springer Science & Business Media
- O'Sullivan, C. (2011) *Particulate discrete element modelling: a Geomechanics Perspective*, London: Taylor & Francis
- Pan, C., Hilpert, M. & Miller, C. T. (2004) Lattice-Boltzmann simulation of two-phase flow in porous media. *Water Resources Research* 40. p. W01501
- Peskin, C. S. (1972) Flow patterns around heart valves: A numerical method. *Journal of Computational Physics* 10(2). p. 252-271

- Pham, H. Q., Fredlund, D. G. & Barbour, S. L. (2005) A study on the hysteresis models for soil-water characteristic curve. *Canadian Geotechnical Journal* 42(6). p. 1548-1568
- Raiskinmaki, P., Kopoen, A., Merikoski, J. & Timonen, J. (2000) Spreading dynamics of three-dimensional droplets by the lattice-Boltzmann method. *Computational Materials Science* 18(1). p. 7-12
- Rothman, D. H. & Keller, J. M. (1988) Immiscible cellular-automaton fluids. *Journal of Statistical Physics* 52(3-4). p. 1119-1127
- Ryan, E. M., Tartakovsky, A. M. & Amon, C. (2011) Pore-scale modeling of competitive adsorption in porous media. *Journal of Contaminant Hydrology* 120-121. p. 56-78
- Sawley, M. L., Cleary, P. W., & Ha, J. (1999) Modelling of flow in porous media and resin transfer moulding using smoothed particle hydrodynamics. In *Second International Conference on CFD in the Minerals and Process Industries*. Melbourne, Vic, 6-8 December 1999. pp. 473-478
- Scardovelli, R. & Zaleski, S. (1999) DIRECT NUMERICAL SIMULATION OF FREE-SURFACE AND INTERFACIAL FLOW. *Annual Review of Fluid Mechanics* 31(1). p. 567-603
- Shan, X. & Chen, H. (1993) Lattice Boltzmann model for simulating flows with multiple phases and components. *Physical Review E* 47(3). p. 1815-1819
- Shan, X. & Doolen, G. (2008) Diffusion in a multi-component Lattice Boltzmann Equation model. *Physical Review E* 54(4). p. 3614-3620
- Shao, J. Y., Shu, C. & Chew, Y. T. (2013) Development of an immersed boundary-phase field-lattice Boltzmann method for Neumann boundary condition to study contact line dynamics. *Journal of Computational Physics* 234. p. 8-32
- Shinto, H., Komiyama, D. & Higashitani, K. (2007) Lattice Boltzmann study of capillary forces between cylindrical particles. *Advanced Powder Technology* 18(6). p. 643-662

- Shu, C., Liu, N. & Chew, Y. T. (2007) A novel immersed boundary velocity correction–lattice Boltzmann method and its application to simulate flow past a circular cylinder. *Journal of Computational Physics* 226(2). p. 1607-1622
- Siebold, A., Siebold, M., Schultz, J., Schultz, A. & Oppliger, M. (2000) Effect of dynamic contact angle on capillary rise phenomena. *Colloids and Surfaces A: Physicochemical and Engineering Aspects* 161(1). p. 81-87
- Sokolichin, A. & Eigenberger, G. (1994) Gas—liquid flow in bubble columns and loop reactors: Part I. Detailed modelling and numerical simulation. *Chemical Engineering Science* 49(24-2). p. 5735-5746
- Succi, S., Foti, E. & Higuera, F. (1989) Three-Dimensional Flows in Complex Geometries with the Lattice Boltzmann Method. *Europhysics Letter* 10(5). p. 443
- Sukop, M. C. & Thorne, D. T. (2006) *Lattice Boltzmann Modeling -An Introduction for Geoscientists and Engineers*. Berlin: Springer
- Sun, D. L. & Tao, W. Q. (2010) A coupled volume-of-fluid and level set (VOSET) method for computing incompressible two-phase flows. *International Journal of Heat and Mass Transfer* 53(4). p. 645-655
- Swift, M. R., Osborn, W. R. & Yeomans, J. M. (1995) Lattice Boltzmann Simulation of Nonideal Fluids. *Physical Review Letters* 75(5). p. 830-833
- Tartakovsky, A. & Meakin, P. (2005) Modeling of surface tension and contact angles with smoothed particle hydrodynamics. *Physical Review E* 72(2). p. 026301
- Tartakovsky, A. M., Meakin, P., Scheibe, T. and Wood B. (2007) A smoothed particle hydrodynamics model for reactive transport and mineral precipitation in porous and fractured porous media. *Water Resources Research* 43(5). p. W05437
- Thürey, N., Iglberger, K. & Rüde, U. (2006) Free surface flows with moving and deforming objects for LBM. *Proceedings of Vision, Modeling and Visualization*. p. 193-200
- Tiwari, A. & Vanka, S. P. (2012) A ghost fluid Lattice Boltzmann method for complex geometries. *International Journal for Numerical Methods in Fluids* 69(2). p. 481-498

Toon, L., Bart, A. & Philip, D. (2008) Porous flow in particle-based fluid simulations. ACM SIGGRAPH 2008 papers, Los Angeles, p. 1-8

Tryggvason, G., Bunner, B., Esmaeeli, A., Juric, D., Al-Rawahi, N., Tauber, W., Han, J., Nas, S. & Jan, Y. J. (2001) A Front-Tracking Method for the Computations of Multiphase Flow. *Journal of Computational Physics* 169(2). p. 708-759

Tseng, Y. H. & Ferziger, J. H. (2003) A ghost-cell immersed boundary method for flow in complex geometry. *Journal of computational physics* 192(2). p. 593-623

Tsuji, Y. (2007) Multi-scale modeling of dense phase gas-particle flow. *Chemical Engineering Science* 62(13). p. 3410-3418

Tsuji, Y. , Kawaguchi, T. & Tanaka, T. (1993) Discrete particle simulation of two-dimensional fluidized bed. *Powder Technology* 77(1). p. 79-87

Van Genuchten, M. T. (1980) A close-form equation for predicting the hydraulic conductivity of unsaturated soil. *Journal of Soil Science Society of America* 44. p. 892-898

Wiki for continuum mechanics (2015) Lagrangian and Eulerian specification of the flow field. [Online] Available from: http://en.wikipedia.org/wiki/Lagrangian_and_Eulerian_specification_of_the_flow_field . [Accessed: 14th April 2015]

Wiki for Physics (2014) Dissipative particle dynamics [Online] Available from : http://en.wikipedia.org/wiki/Dissipative_particle_dynamics [Accessed : 14th April 2015]

Wu, J. & Shu, C. (2009) Implicit velocity correction-based immersed boundary-lattice Boltzmann method and its application. *Journal of Computational Physics* 228. p. 1963-1979

Yang, G. Q., Du, B. & Fan, L. S. (2007) Bubble formation and dynamics in gas-liquid-solid fluidization—A review. *Chemical Engineering Science* 62(1-2). p. 2-27

Zhmd, B.V., Tiberg, F. & Hallstenson, K. (2000) Dynamics of capillary rise. *Journal of Colloid and Interface Science* 228(2). p. 263-269

Zwart, P. J., Raithby, G. D. & Raw, M. J. (1999) The integrated space-time finite volume method and its application to moving boundary problems. *Journal of Computational Physics* 154(2). p. 497-519

Appendix A The conservation between physical units and LB units

Variable	Physical	Lattice	Relationship
Density	ρ	$\bar{\rho}$	$\rho = \rho_0 \bar{\rho}$
Relaxation time	τ	τ	
Spacing	h	$\bar{h} = 1$	
Time Step	Δt	$\Delta \bar{t} = 1$	
Lattice Speed	$C = \frac{h}{\Delta t}$	$\bar{C} = 1$	
Viscosity	$\nu = \tau c_s^2 \frac{h^2}{\Delta t}$	$\bar{\nu} = \tau c_s^2$	$\nu = Ch\bar{\nu}$
Coordinate	x	\bar{x}	$x = h\bar{x}$
Velocity	$\mathbf{v} = \frac{d\mathbf{x}}{dt}$	$\bar{\mathbf{v}} = \frac{d\bar{\mathbf{x}}}{d\bar{t}}$	$\mathbf{v} = C\bar{\mathbf{v}}$
Acceleration	$\mathbf{a} = \frac{d^2\mathbf{x}}{dt^2}$	$\bar{\mathbf{a}} = \frac{d^2\bar{\mathbf{x}}}{d\bar{t}^2}$	$\mathbf{a} = \frac{C}{\Delta t}\bar{\mathbf{a}}$
Mass	m	\bar{m}	
Stiffness	k_n	\bar{k}_n	$k_n = C^2\bar{k}_n$

Appendix B Difference scheme used in LBM

In the LB model, a combination of central (CD) and biased (BD) directional derivatives will be used in the calculation of gradients and Laplacians of macroscopic variable. In calculation of equilibrium state distribution functions and the zero and first moment of the distribution functions, the simple central difference method will be applied, while in the collision step, the combination difference method will be imposed in the corresponding terms.

A central difference directional derivative of a variable Φ at x can be stated as:

$$\delta t \mathbf{e}_i \cdot \nabla^{CD} \phi|_x = \frac{1}{2} [\phi(\mathbf{x} + \mathbf{e}_i \delta t) - \phi(\mathbf{x} - \mathbf{e}_i \delta t)] \quad (\text{B.1})$$

And the corresponding central difference gradient is taken as the moment

$$\nabla^{CD} \phi|_x = \frac{1}{c_s^2 \delta t} \sum_{i \neq 0} t_i \mathbf{e}_i (\delta t \mathbf{e}_i \cdot \nabla^{CD}) \phi|_x \quad (\text{B.2})$$

Similarly, the biased difference directional derivatives and the biased difference gradient can be written as:

$$\delta t \mathbf{e}_i \cdot \nabla^{BD} \phi|_{x-\mathbf{e}_i \delta t} = \frac{1}{2} [-\phi(\mathbf{x} + \mathbf{e}_i \delta t) + 4\phi(\mathbf{x}) - 3\phi(\mathbf{x} - \mathbf{e}_i \delta t)] \quad (\text{B.3})$$

$$\nabla^{BD} \phi|_x = \frac{1}{c_s^2 \delta t} \sum_{i \neq 0} t_i \mathbf{e}_i (\delta t \mathbf{e}_i \cdot \nabla^{BD}) \phi|_x \quad (\text{B.4})$$

For the difference derivatives in collision steps, an average of the central and biased differences will be used as:

$$\delta t \mathbf{e}_i \cdot \nabla^{MD} \phi|_x = \frac{1}{2} [\delta t \mathbf{e}_i \cdot \nabla^{CD} \phi + \delta t \mathbf{e}_i \cdot \nabla^{BD} \phi]|_x \quad (\text{B.5})$$

$$\nabla^{MD} \phi|_x = \frac{1}{2} [\nabla^{CD} \phi + \nabla^{BD} \phi]|_x \quad (\text{B.6})$$

For the Laplacians, the following difference scheme will be used in the model:

$$(\delta t \mathbf{e}_i \cdot \nabla^{CD})^2 \phi|_x = [\phi(\mathbf{x} + \mathbf{e}_i \delta t) - 2\phi(\mathbf{x}) + \phi(\mathbf{x} - \mathbf{e}_i \delta t)] \quad (\text{B.7})$$

$$\nabla^2 \phi|_x = \frac{1}{c_s^2 \delta t^2} \sum_{i \neq 0} t_i (\delta t \mathbf{e}_i \cdot \nabla^{CD})^2 \phi|_x \quad (\text{B.8})$$